OBSERVATIONS AND MODELING OF THE COASTAL OCEAN BENEATH

TROPICAL AND EXTRA-TROPICAL CYCLONES

By

Travis N. Miles

A Dissertation Submitted to the

Graduate School-New Brunswick

Rutgers, The State University of New Jersey

In partial fulfillment of the requirements

For the degree of

Doctor of Philosophy

Graduate Program in Oceanography

Written under the direction of

Scott M. Glenn

And approved by

_____

_____

_____

_____

New Brunswick, New Jersey

May 2014

ABSTRACT OF THE DISSERTATION

OBSERVATIONS AND MODELING OF THE COASTAL OCEAN BENEATH

TROPICAL AND EXTRA-TROPICAL CYCLONES

By Travis N. Miles

Dissertation Director:

Scott M. Glenn

Tropical and extra-tropical cyclones are important episodic events that redistribute heat, nutrients, sediment, pollutants, carbon and other tracers on continental shelves, enhance near-surface chlorophyll and initiate phytoplankton blooms. These storms also cause extensive coastal damage through direct wind forcing, storm surge and precipitation. Despite the importance of these storms, they are chronically difficult to sample due to the extreme sampling conditions.

In my thesis I present data from Teledyne-Webb Slocum autonomous underwater vehicles (AUVs) deployed beneath an extra-tropical cyclone, Nor'Ida, and Huricane Sandy on the Mid-Atlantic Bight (MAB). In the first chapter of my thesis I used data from multiple AUVs and an ocean observation network to show that small-scale (O10km) spatial variability in sediment grain size is responsible for observed spatial variability in sediment resuspension and transport, even in large storms.

In the second chapter we deployed an AUV with an upward looking current meter beneath Hurricane Sandy and found that offshore advection of a downwelling front rapidly removed a cold water mass (the summer Cold Pool) from the continental-shelf over 18 hours before the storm made landfall. This study demonstrates that advective processes need to be included in future coupled atmospheric-ocean models to accurately forecast storm intensity.

In the third and final chapter of my thesis I used optical, acoustic and hydrographic data collected by the AUV during Hurricane Sandy to validate coupled hydrographic, bottom boundary layer and sediment models. This study is one of the first validations of the coupled model during an extreme storm on the MAB and shows broad patterns of erosion and deposition during Hurricane Sandy.

Acknowledgements

While this thesis is intended to be a showcase of my own original work, it would not have been possible without the continued creative, emotional and technical support of a vast network of individuals. Much of this thesis revolves around a networked coastal ocean, but the true network is the human network that drives continued creative and exciting research.

First, I would like to thank my co-advisors Scott Glenn and Oscar Schofield, for their friendship, support and trust over the past 5 years. I have truly taken their mantra of "Learn one, do one and teach one" to heart, and look forward to the next "teach one" phase of my career. Thanks also go to Josh Kohut and Doug Martinson for taking the time to guide and support my research and education. To the other professors at the Institute of Marine and Coastal Sciences, thank you for always having your doors open and making time to answer questions, regardless of how busy you may be.

I would like to thank past and present members of the Rutgers University Coastal Ocean Observation Laboratory. Without the diligence and hard work of Dave Aragon, Chip Haldeman and Tina Haskins none of this work would have been possible. Calling gliders 'autonomous' may be one of the larger understatements within this document. The dedication of these three people continues to push the edges of what we can sample. Additional thanks goes to Eli Hunter, John Kerfoot, Mike Crowley, Steve Levenson, Patty Gillen, Greg Seroka, Yi Xu, Donglai Gong, Joe Jurisa, Laura Palmara and all of the past and present graduate students who have provided me with friendship and helpful commentary.

I would like to give a special thanks to my family, Wesley, Charles and Cindy Miles for inspiring my excitement and interest in the ocean for as long as I can remember. To Katie Brennan, my fiancé and future wife, thank you for not only loving and supporting me, but also literally traveling to the ends of the earth with me.

Table of Contents

List of Figures

Chapter 1

Introduction

The New York Metropolitan area adjacent to the Mid-Atlantic Bight (MAB) has a population of over 19 million people and accounts for close to 10% of the United States Gross Domestic Product. Tropical and extra-tropical cyclones have extensively impacted the MAB, with Hurricanes Irene and Sandy, the 8th and 2nd costliest storms in U.S. history respectively, making landfall in New Jersey in 2011 and 2012 (http://www.ncdc.noaa.gov/billions/events). Hurricane Sandy alone caused over $60 billion in damages through a combination of intense wind and storm surge. Extra-tropical and tropical cyclones such as Sandy also play a large role in shoreline erosion, sediment transport, drive the transition of the coastal ocean from summer to winter conditions and have far reaching ecological implications for the coastal ocean. Despite the importance of such events, the coastal ocean ahead of and beneath these storms are chronically under-sampled. My dissertation focuses on using autonomous underwater vehicles, specifically Teledyne-Webb Slocum gliders to observe the coastal ocean beneath these storms.

In Chapter 2, using two autonomous underwater gliders, long-range high frequency radar and buoy data, we quantified spatial variability of sediment resuspension and transport in a large fall storm in November of 2009. Wave, wind and current data in conjunction with glider profiles showed that waves and winds mixed the water column, waves initially mobilized the sediment and shear induced turbulence advected sediment throughout the water column. The separation of over

50 km between the two gliders (RU05 and RU21) is used to highlight the spatial variability of sediment resuspension. Both gliders were operating along the 40 m isobath with RU21 located 50 km north of RU05. Sediment resuspension on the New Jersey shelf responded to synoptically forced turbulent motions. Currents transported this sediment toward the southwest in the along-shelf direction and onshore on the cross-shelf direction during the peak resuspension on November 13th through November 14th of 2009, with resuspension and transport on the southern New Jersey shelf measured by RU05 approximately twice that of RU21 on the northern MAB. Variability in resuspension profiles between the two gliders was largely a product of smaller mean grain sizes on the southern portion of the NJ shelf. These smaller grain sediment particles had a reduced fall velocity and were more easily retained throughout the water column by turbulent motions. This chapter has been published in Continental Shelf Research [*Miles et al.,* 2013]. Myself, Scott Glenn and Oscar Schofield are co-authors on this work.

In Chapter 3, we present unique observations from a Teledyne-Webb Slocum glider RU23, which was equipped with an upward looking Nortek Aquadopp current profiler. This instrument was deployed on the MAB ahead of Hurricane Sandy and remained in the northeast quadrant of the storms, a region of typically strongest winds, waves and currents. Using these observations as well as other regional assets we showed that downwelling favorable wind lead to sea level setup along the coast, which drove two-layer cross-shelf circulation while the water column remained stratified and along-shelf geostrophic flow toward the southwest. The glider observed deepening of the thermocline and the transition from one- to two- layer flow in approximately 12 hours

due to offshore advection of the cold bottom layer. This resulted in a uniformly warm water column on the continental shelf 18 hours before the eye of the storm crossed the shelf. This work is in preparation to be submitted to Journal of Physical Oceanography.

In Chapter 4, we use the Regional Ocean Modeling System (ROMS) on the ESPreSSO domain for the New Jersey shelf to model sediment resuspension and transport during Hurricane Sandy. In this study we use the standard ESPreSSO setup but include a coupled bottom boundary layer formulation, force with the National Oceanographic and Atmospheric Administration (NOAA) WAVEWATCH III wave model and model sediment with the community sediment transport model included in ROMS. We provide the first ever *in situ* glider validation of sediment resuspension and transport using a combination of acoustic and optical backscatter sensors to validate modeled medium (0.4mm) and fine (0.1mm) sand concentrations. Full water column resuspension and transport was apparent in both the model and observations, with along-shelf currents of over 1 m s^{-1} toward the southwest and wave bottom orbital velocities of over 2 m s^{-}1. The model showed erosion on the northern side of the storm track of over 2 cm and deposition south of the storm track of over 2 cm. Deposition was the result of a switch from along-shore to offshore wind stress on the southern portion of the MAB, which reduced wave heights and subsequently bottom orbital velocities over a short time period. Typically validation datasets for sediment modeling in storms are limited to point measurements or post-storm surveys. This study is the first to use glider technologies to validate regional scale sediment resuspension and transport, and demonstrates a new application for future glider deployments.

Chapter 2

Temporal and spatial variability in fall storm induced sediment resuspension on the Mid-Atlantic bight.

2.1 Introduction

Coastal storm-driven mixing events are episodic processes [*Wiggert et al.*, 2000; *Chang et al.*, 2001; *Zedler et al.*, 2002] that are important for sediment transport. Despite numerous focused field campaigns on storm induced sediment resuspension [*Traykovski et al.*, 1999; *Styles and Glenn*, 2002b; *Traykovski*, 2007], the processes dominating the spatial variability of the storm response remains unresolved. The Mid-Atlantic Bight (MAB) is a region impacted by numerous physical forcing processes such as freshwater input from a complex network of rivers and estuaries, wave tidal and inertial fluctuations, variable topographic features such as the Hudson Shelf Valley and the ridge and swale topography [*Beardsley and Boicourt*, 1981; *McBride and Moslow*, 1991] the shelf-break jet [*Chen and He*, 2010]and Gulf Stream eddies near the shelf-break, seasonal wind variability [*Gong et al.*, 2010], the summer cold pool [*Lentz*, 2008] and powerful winter storms [*Beardsley and Boicourt*, 1981].

Strong solar insolation drives the formation of the summer cold pool that results in large seasonal variations in the water column stratification between winter and summer seasons [*Houghton et al.*, 1982; *Lentz*, 2003]. This stratification is broken down by extra-tropical cyclones, commonly referred to as fall transition storms [*Bigelow*, 1933; *Beardsley and Boicourt*, 1981]. These storms result in a well-mixed water column in the winter until early spring [*Lentz*, 2003]. The erosion of

the stratification is important for the MAB ecosystem as it replenishes nutrients to the surface layer, which stimulates phytoplankton blooms [*Xu et al.*, 2011]. The winter phytoplankton bloom is the largest and most predictable biological event on the MAB [*Xu et al.*, 2011]. Resuspension of sandy sediments, which are dominant on the middle- to outer- shelf of the MAB [*Swift and Field*, 1981; *Amato*, 1994; *Reid et al.*, 2005; *Goff et al.*, 2008], is commonly driven by fall transition storms through a combination of waves and currents [*Glenn et al.*, 2008]. For example, *Styles and Glenn* (2005) identified 25 sediment transport events over a 2-year period, with 63% of these events occurring in fall and winter on the MAB.

A combination of waves and currents are responsible for the resuspension and transport of sediment on the continental shelf. Though non-linear interactions between waves and currents dominate sediment resuspension, seminal work by *Grant and Madsen* (1979) provides a qualitative explanation of the independent role each process plays. Wave bottom boundary shear stress can be an order of magnitude larger than current bottom boundary shear stress. Wave-induced bottom orbital velocities have a similar magnitude to low-frequency currents but operate over a much smaller bottom boundary layer and thus result in an observed order of magnitude larger shear stress. Despite the high shear stress, wave velocities are orbital and therefore result in little net horizontal transport to first order. When sediment is suspended in the water column even relatively minor low-frequency currents are capable of horizontal sediment transport.

Keen and Glenn (1995) and *Styles and Glenn* (2005) show storm-induced sediment transport is generally aligned along-shelf toward the southwest through

modeled and observed bottom currents during Nor'easter storms. Modeled cross-shelf sediment transport was offshore *Keen and Glenn* (1995); however the observed cross-shelf component of the transport was predominantly onshore in *Styles and Glenn* (2005). These observations are surprising as it might be expected that Nor'easters produce downwelling circulation with offshore bottom transport that is reinforced by the tides; therefore a more complex combination of processes must be important.

Several processes have been hypothesized to account for the onshore transport. Potential factors include topographic interactions that operate over the relatively small (a few kilometers) scale of the ubiquitous ridge and swale topography of the MAB inner shelf [*McBride and Moslow*, 1991], or over the larger (a few tens of kilometers) scale of the topographic highs associated with ancient river deltas [*Glenn*, 2004]. Additionally, *Gargett et al.* (2004) identified full water column Langmuir cells as a significant driver of sediment resuspension events on the Mid-Atlantic Bight. *Keen and Glenn* (1995) also identified tides as critical to resuspension and transport modulation, as tidal currents can alternately enhance or reduce the more slowly varying storm driven currents. In their work, the tidal phase was important in determining onshore or offshore veering of the predominant alongshore bottom current. *Styles and Glenn* (2005) did not observe current veering with tidal phase and saw onshore transport near bottom, though their observations were limited to the 10 meter water depth. Given this, the cross-shelf magnitude and direction of sediment transport are still unresolved.

Shipboard observations are likely biased to fair weather conditions as these

sampling techniques are limited by the extreme conditions experienced in storms.
Benthic tripods are ideally suited to resolve temporal variability effectively during
extreme conditions but are expensive to deploy and are not designed to sample
horizontal spatial variability. Recent work by *Glenn et al.* (2008) has demonstrated
the potential of using autonomous Slocum gliders for sampling sediment transport
events on the continental shelves. This work demonstrated that it is possible to
average optical backscatter profiles of a single sensor and obtain results that are
consistent with the theoretical understanding of coastal storm induced sediment
resuspension. This manuscript builds on these results, using two simultaneously
deployed gliders to examine the spatial and temporal variability during a fall
transition storm on the MAB as well as introducing glider vertical motions as a
proxy for turbulence.

Hurricane Ida, was a low pressure system that developed into a category two
hurricane over the Gulf of Mexico. Ida transitioned into an extra-tropical cyclone
over the southeastern United States on November 10th, 2009. This system,
commonly referred to as Nor'Ida, tracked northeastward along the eastern United
States coast and into Canada causing extensive damage and coastal flooding. We
present data from multiple gliders during Nor'Ida over large along- and cross- shelf
spatial scales and incorporate shelf-wide HF radar surface currents [*Roarty et al.*,
2010] measured with 6 km resolution for the duration of a fall transition storm.
Both gliders started from the same location off Tuckerton, New Jersey (Figure 2.1)
and performed cross-shelf transects offshore. As in *Glenn et al.* (2008), deviation
from flight paths and increases in glider depth-averaged currents indicate storm

passage. Glider tracks and depth averaged currents for RU05 and RU21 can be seen in Figures 2.2 and 2.3. RU05 took a brief northeastward turn followed by a long southwestward along-isobath track, which was enhanced by southwestward storm induced currents. RU21 finished its offshore cross-shelf transect and returned to complete an onshore cross-shelf transect, with deviations as a result of southwestward storm induced currents.

2.2 Materials and Methods

This project relied on infrastructure operated by the Mid-Atlantic Regional Association Coastal Ocean Observing System (MARACOOS) that is part of the United States Integrated Ocean Observing System (U.S. IOOS) [*Roarty et al.*, 2010; *Schofield et al.*, 2010b]. MARACOOS provides a suite of data collected by satellites, a high frequency CODAR network, and a fleet of Webb Slocum gliders [*Glenn and Schofield*, 2009]. All of the above remote sensing techniques are coupled to a super ensemble of data assimilative numerical ocean models (see below).

2.2.1 Ocean Observation Dataset

A network of CODAR Ocean Sensors SeaSonde HF Radar systems measures surface currents on the MAB. The CODAR network consisted of 13 5-MHz HF Radar systems located along the northeast of the United States (Figure 2.1). The HF Radar uses the Doppler Shift of a radio signal backscattered off the ocean surface to measure the component of the flow in the direction of the antenna [*Barrick*, 1971a, 1971b; *Teague*, 1971]. Descriptions of the CODAR data and its shelf-wide applications are outlined in *Dzwonkowski et al.* (2009) and *Gong et al.* (2010). The network provides surface current observations at the estimated equivalent depth of

2.4 m [*Stewart and Joy*, 1974]. To minimize the geometric uncertainty in the radials we used the recommended threshold for the Geometric Dilution of Precision (GDOP) [*Chapman and Graber*, 1997]value of 1.5 or less to identify the vectors with acceptable GDOP [*Dzwonkowski et al.*, 2009a]. This value is chosen based on current comparison studies using CODAR and ship-mounted Acoustic Doppler Current Profilers [*Kohut et al.*, 2006] and drifters [*Ohlmann et al.*, 2007]. The spatial resolution of the final total vector current maps is 6 km with a typical cross-shelf range of 150 km.

Sediment mean grain size is determined by taking a regional subsample of a 2 km resolution interpolated sediment map developed by *Goff et al.* (2008) from data compiled as part of the usSEABED project (http://walrus.wr.usgs.gov/usseabed/). We convert phi units into mm grain size since the sandy sediment only varies over two phi units (Figure 2.1).

Oceanographic data from NOAA NDBC buoys 44009 and 44025 were used in this effort (Figure 2.1). The moorings provided data on atmospheric pressure, wind speed/direction, wave-height, period and direction.

Slocum gliders are an autonomous underwater scientific platform [*Davis et al.*, 2003; *Schofield et al.*, 2007] manufactured by the Teledyne Webb Research Corporation. They are 1.8-m long, torpedo-shaped, buoyancy-driven vehicles with wings that enable them to maneuver through the ocean at a forward speed of 20–30 cm s^{-1} in a sawtooth-shaped gliding trajectory. A full description of our scientific operation of the Slocum gliders can be found in L. Each Slocum glider has a payload bay that houses a SeaBird conductivity–temperature–depth sensor and includes

space for a range of additional sensors. The glider acquires its global positioning system (GPS) location every time it surfaces, a programmable interval that was set to 3 hours for the purposes of this study. By dead reckoning along a compass bearing while flying underwater, estimates of depth averaged current can be calculated based on the difference between the glider's expected surfacing location and the actual new GPS position. These physical measurements are complemented with several bio-optical sensors [*Glenn and Schofield*, 2009].

Two Webb Slocum gliders were deployed prior to November 1, 2009 and operated for two weeks. During that period the gliders traversed 1673 kilometers underwater collecting 23,332 vertical profiles (Figure 2.1). The gliders were outfitted with WetLabs Inc. EcoPucks, which provide measurements of optical backscatter, chlorophyll fluorescence and colored dissolved organic fluorescence. The EcoPucks measure optical backscatter at 440 (b_b470) and 660 (b_b660) nm. Optical backscatter, to first order, is used to measure the relative concentration of particulate matter [*Roesler and Boss*, 2008]. A growing body of work indicates that optical backscatter is not only a function of particle concentration but also sediment characteristics such as refractive index, size, shape and particle composition [*Twardowski et al.*, 2001; *Boss et al.*, 2004]. While we do not characterize sediment in great detail during the measured resuspension events, we use changes in backscatter ratios to indicate a change in character of suspended particles.

2.2.2 Adaptive Sampling

To coordinate the numerous observed and forecast model data streams, we were able to utilize a novel cyberinfrastructure (CI) tool set being developed as part

of the Ocean Observing Initiative (OOI). The software was used to coordinate

sampling using multi-model forecasts to optimize glider missions [*Schofield et al.*,

2010a]. In brief, numerical model ocean forecasts allowed the simulation of future

in situ glider trajectories. This guidance could be used by the team to optimize

sampling based on the science needs. This provided scientists with a guide to

determine whether desired target areas could be reached by Webb Slocum gliders

in a predicted current field. Thus the CI software could deliver the community

science needs back to the *in situ* observation network in a timely manner. Field

operations were coordinated through a web portal

(http://ourocean.jpl.nasa.gov/CI) that provided an access point for real-time

observational data and model forecasts.

2.3 Results

2.3.1 Pre-storm Hydrography

Pre-storm conditions were typical for fall on the MAB with predominantly

vertical isotherms and a cross-shelf temperature gradient. RU21, on its offshore

transect (Figure 2.2) between October 31st and November 5th, showed a near-shore

water mass that was approximately 1 kg m^{-3} lighter than offshore waters (Figure

2.5). This lower density coastal water was largely due to the variability in salinity.

Additionally, there was a warm core of water centered at 15m depth, on the 35m

isobath, which contributed to the regional vertical and horizontal density gradients.

This glider data shows that New Jersey shelf waters were generally colder, saltier

and denser in the offshore direction. B_b470 was low (< 0.005 m^{-1}) for the majority of

the offshore pre-storm transect. There is a small region of elevated backscatter

near-shore located below the pycnocline. RU21 was not programmed to dive below 20m until after it reached the 25m isobath so the optical backscatter at the bottom in the near-shore region was not completely sampled. Pre-storm water column b_b470 to b_b660 ratios were high (~ 3) relative to storm signatures (see below). There was a short period of elevated currents toward the northeast in the coastal region (Figure 2.2). Prior to the storm both the gliders and CODAR (Figure 2.2, 2.3, 2.6) showed variable currents between 5 and 40 cm s^{-1} along the coast of New Jersey, with daily averaged currents immediately prior to the storm event somewhat higher than the climatological mean of 5 cm s^{-1} [*Beardsley and Boicourt*, 1981].

2.3.2 Storm Data

Buoy 44009, off of Delaware Bay, and 44025, off Long Island are separated by approximately 230 km with 44009 encountering Nor'Ida first (Figure 2.4). As the storm entered the MAB region from the southwest, pressure fell from above 1020 mbar at both buoys to a minimum of 1002 mbar on November 13th at 2000 Greenwich Mean Time (GMT) at 44009 and a minimum of 1007 mbar on November 13th at 2350 GMT at 44025 (Figure 2.4A). Winds at both locations began to increase at 0000 GMT on November 11th, but peak winds at 44025 lagged 44009 by 28 hours with slightly lower magnitude until they reached a maximum of 20.5 ms^{-1} at 23:50 GMT on November 13th (Figure 2.4B). Prior to November 11th wind direction was variable. Between November 11th and late on the 15th,wind direction at both buoys was from the northeast (Figure 2.4C). Wave-heights began to build after a few hours of rising winds at both locations (Figure 2.4D). Wave heights reached over 8 meters at 0050 GMT on November 13th at 44009 and over 6 meters at 0350 GMT on the 14th

at 44025. Wave spectral periods were between 7 and 9 s for the duration of the storm at both locations and continued to increase after storm passage, eventually peaking at ~10 s on the morning of November 16th (Figure 2.4E). Maximum wave bottom orbital velocities were calculated from buoy data using linear wave theory as described by Glenn et al. (2008). Wave bottom orbital velocity estimates peaked at 2.4 m s^{-1} and 1.8 m s^{-1} at buoy 44009 and 44025 respectively (Figure 2.4F), significantly higher than glider depth-averaged and CODAR surface currents (Figure 2.2, 2.5, 2.8).

CODAR daily averaged currents (Figure 2.6) were toward the southwest on November 11th and reached 30 cm s^{-1} on the central and southern MAB with values offshore nearing 50 cm s^{-1}. CODAR daily averaged surface currents peaked in excess of 50 cm s^{-1} shelf-wide on the central and southern MAB on the 13th. There was a low velocity region on the northwestern MAB near the Hudson River outflow. Over the two days following peak values, shelf-wide currents decreased back to near pre-storm values, below ~15 cm s^{-1}.

2.3.3 RU21 Northern Glider Storm Variability

As Nor'Ida approached the New Jersey shelf, RU21 turned onshore and attempted to retrace the path of the offshore transect (Figure 2.2). Initially it flew southwestward along the 40m isobath until it turned onshore on the 15th. Cross-sections of glider measurements (Figure 2.7) show that during its southwestward transect RU21 initially measured vertically uniform temperatures of 15°C, salinity of 33 PSU, density near 1024.6 kg m^{-1}, optical backscatter at b_b470 nm was near 0 m^{-1} and the ratio of b_b470 to b_b660 was ~ 3. Downcast vertical glider velocities were

uniform at ~ 0.3 m s^{-1}. Vertical glider velocities were calculated by the change in

measured pressure over time and we used them to serve as a proxy for vertical

water velocities. In uniform water masses with no external turbulent forcing and the

glider on a new constant glide slope, vertical velocities should have also remained

approximately constant except when the glider was inflecting near-bottom or near

surface.

As winds, waves and currents increased beginning on the 11th, there was a

distinct water column response. First, glider vertical velocities began to undergo

high-frequency variability of ~ 0.1 to 0.2 m s^{-1} through the entire water column.

These vertical velocity variations persisted through the 14th until they were

restricted to a bottom layer and eventually relaxed after the 16th. As the magnitude

of vertical velocities increased, temperatures cooled to 14° C, salinity was elevated

above 33 PSU and 1025 kg m^{-1} density water was raised to the surface. Values of

b_b470 of ~ 0.05 m^{-1} were evident throughout the water column on the 13th. The

enhanced particle load remained suspended until the afternoon of the 14th. Optical

backscatter spectral ratios changed from 3 to 1 as Nor'Ida impacted the region,

reflecting a flattening of the backscatter spectra consistent with changes in either

particle type and/or particle size in the water-column [*Boss et al.*, 2004].

Previous studies have clearly defined the Rouse profile above the wave

boundary layer [*Glenn and Grant*, 1987; *Styles and Glenn*, 2000; *Glenn et al.*, 2008] as:

$$C(z) = C(z_r) \left[\frac{z}{z_r}\right]^{\left[-\frac{\gamma w_f}{\kappa u_*}\right]} \qquad (2.1)$$

where $C(z)$ is the concentration profile varying with depth z, $C(z_r)$ is the

concentration at the reference height z_r, γ is a constant ratio of eddy diffusivities

between momentum and mass, κ is von Karman's constant and u_* is friction

velocity. Assuming constant γ (Glenn and Grant, 1987), the slope of $\ln\left(\frac{C(z)}{C(z_r)}\right)$ to

$\ln\left(\frac{z}{z_r}\right)$ is proportional to the ratio of the fall velocity, the tendency of sediment to fall

out of the water column, to the friction velocity representing the turbulent shear

that acts to keep sediment suspended in the water column, or $\frac{w_f}{u_*}$. In order to identify

this ratio, we use optical backscatter as a proxy for sediment concentration similar

to Glenn et al. (2008). Optical backscatter profiles were interpolated every 1 m in a

reference frame measured from the bottom and averaged over three-hours. These

three-hour profiles were then normalized using the backscatter observed at a 3.5 m

reference height and plotted as the $\ln(\frac{z}{z_r})$ versus $\ln(\frac{b_b(z)}{b_b(z_r)})$. The 3.5 m reference

height ensures all profiles in each three-hour segment have data at this height and

above. Normalized backscatter profiles from RU21 (Figure 2.8) demonstrated

Rouse-like character from the 14th at 04:24 GMT until the 14th at 21:23 GMT. High

near-surface values in rough seas are likely due to bubbles being entrained by

breaking waves. *Terrill et al.* (2001) has observed optical backscatter values of over

0.016 m^{-1} inside bubble clouds.

On November 15th, at approximately 06:00 GMT, RU21 turned onshore and

left the 40 m isobath, indicated by the green section of Figure 2.2b. As the glider

entered the shallow coastal region, temperature, salinity and density remained well-

mixed in the vertical while there were horizontal gradients of $\sim$ 1 ^{o}C, $\sim$ 1.5 PSU and

~ 1.5 kg m^{-3} respectively (Figure 2.7). On the 15th to the 18th a layer of high b$_b$470, over 0.1 m^{-1}, was apparent, elevated to 10 to 15 m off the bottom (Figure 2.7). Profiles (Figure 2.8) show a layer restricted below $\ln\left(\frac{z}{z_r}\right) = $ 1.5, roughly equivalent to 15 meters. The lower layer persists through the remainder of the deployment. Though winds and currents were reduced, wave-heights, wave-periods and bottom orbital velocities remained significantly elevated (Figure 2.4). Glider measured vertical velocity variability remained elevated in the near-bottom layer through the 16th (Figure 2.7).

2.3.4 RU05 Southern Glider Storm Variability

Between the 10th and 16th of November, RU05 was on a southwestward track along the 40 m isobath (Figure 2.3). RU05 turned onshore toward the mouth of the Delaware River on the 16th through the 18th. RU05 cross-sections (Figure 2.9) show that on Nov 10th the water column was initially stratified with relatively cool (~14 ^{o}C) and salty (~33.5 PSU) bottom water, likely a remnant of the summer cold pool. Cross-sections show that dense bottom water was advected through the lower half of the water column late on the 10th into the 11th. There were periodic bulges of weakly stratified water (0.6 to 0.2 kg m^{-3}), which grew progressively weaker until the water column was vertically well mixed on the 16th. Similar to RU21, b$_b$470 was low initially and spectral ratios of b$_b$470 to b$_b$660 were ~ 3. Vertical velocities were initially constant at ~ 0.3 m s^{-1} and variations of 0.1 to 0.2 m s^{-1} were apparent during elevated wind, waves and currents. A consistent background b$_b$470 value of 0.05 m^{-1} is apparent throughout the water column, and near-bottom values are near 0.1 m^{-1} until RU05 turns onshore on the 16th. Unlike RU21, there were periodic full

water column resuspension events with b_b470 of 0.1 m^{-1} that occur on time-scales less than a day. Similar to RU21, ratios of b_b470 to b_b660 dropped, which indicated changes in either particle type and/or particle size. Regardless of the periodicity seen in b_b470 cross-sections, the ratios are constant and ~ 1 after the resuspension event was initiated.

RU05 profiles of optical backscatter (Figure 2.10) were calculated in the same manner as for RU21 and for the same duration, from November 13th through the 15th. Reference depth normalized profiles were near 0 until 21:02 GMT on the 13th when the profiles became Rouse-like. Post-storm approximately eight hours earlier than the northern glider, RU21. RU05 then turned onshore toward the Delaware River mouth on the 16th to the 18th (indicated by green in Figure 2.3), vertical velocities, winds and currents were reduced, while wave- height, period and orbital velocities remained elevated relative to pre-storm conditions.

2.3.5 Sediment Transport

Three-hourly averaged CODAR surface velocities were compared with approximately three-hourly depth-averaged glider currents (Figure 2.11). CODAR velocities are averaged in a 10km radius of each glider surfacing latitude and longitude. There is a minor temporal and spatial mismatch between glider depth-averaged and CODAR currents as glider currents are averaged over a three-hour subsurface transit obtained by dead reckoning along a compass bearing and then comparing the expected glider surfacing location with the actual surfacing location. Depth-averaged currents obtained in this manner have been validated against traditional current measurements from stationary ADCPs [*Davis et al.*, 2003] While

we could not obtain any subsurface current structure information directly, by comparing depth-averaged and surface currents, we can make some inferences about how subsurface currents change during the storm.

RU21 and RU05 depth-averaged along-shelf currents both showed similar results when compared with CODAR currents for the duration of each glider deployment. The storm event is easily identifiable in both gliders, which were approximately along the 40 m isobath, between the 10th and 15th, with onshore currents up to 40 cm s^{-1} and alongshore currents toward the southwest of up to 80 cm s^{-1}. Correlation coefficients calculated between glider and CODAR currents for the entire deployment showed a weak correlation in cross-shelf currents of 0.30 for RU05 and 0.33 for RU21. Correlation coefficients in the along-shelf direction were much greater, with values of 0.81 for RU05 and 0.77 for RU21. Correlation coefficients of CODAR and glider comparisons limited to during and after the storm, from the 10th to the 18th, showed that the cross-shelf components increased to 0.44 for RU05 and 0.5 for RU21 and the along-shelf components remained essentially the same at 0.81 for RU05 and 0.84 for RU21. The weak cross-shelf correlation coefficients suggest that deeper currents were initially weaker and not necessarily in the same direction as surface currents. Increased correlation during and after the storm suggest that subsurface currents in the cross-shelf direction either increased in magnitude or aligned more closely with surface currents.

In order to estimate sediment transport magnitude and direction, a time-series of integrated b_b470 was calculated by integrating over depth and segment b_b470 during the RU05 and RU21 deployments and then (Figure 2.12). These depth

and time integrated plots show elevated values of backscatter that initiated on the 13th and remained elevated through the duration of the storm until the 16th with the southern glider, RU05, showing much larger values during the storm. The northern glider, RU21, had a second peak after the storm, which was approximately double the size of the storm-induced values. Estimated transport was calculated by multiplying the integrated backscatter by the along- and cross- shelf depth-averaged currents reported by the gliders (Figure 2.12). Prior to the storm, low sediment concentrations and low currents result in transport near 0 s^{-1}. During the resuspension event, sediment was transported toward the southwest in the along-shelf (Figure 2.12) direction for both RU05 and RU21. RU05 showed approximately twice the along-shelf sediment transport as RU21 during the storm. RU05 and RU21 cross-shelf transport was approximately half of the along-shelf transport and in the onshore direction during the storm. Following the storm RU05 transport was reduced to near 0 s^{-1} when currents and integrated backscatter were both reduced (Figure 2.12). RU21 transport shifted to the offshore direction as high b_b470 still remained in the water column (Figure 2.12) and current velocities were reduced (Figure 2.11) as it approached the coast.

2.4 Discussion

While many studies have focused on sediment resuspension at a single point on the MAB shelf [*Traykovski et al.*, 1999; *Agrawal and Pottsmith*, 2000; *Harris et al.*, 2003; *Agrawal*, 2005; *Cacchione et al.*, 2008] few observational studies have focused on the shelf-wide spatial variability of these processes. We were fortunate to have several gliders deployed to assess the spatial variability of sediment resuspension

on the MAB during the Nor'Ida fall transition storm. The two gliders equipped with optical sensors, separated by ~50 km at the onset of storm conditions, documented the initiation of sediment resuspension through the increases in optical backscatter. Just like the two gliders, buoys 44009 and 44025 (separated by 230 kilometers) showed similar characteristics, with a 1-day lag in peak values, through the initiation of elevated storm winds and waves. Despite the separation distances, along-shelf transport toward the southwest was a ubiquitous feature of both glider deployments with a lag in resuspension of approximately eight hours. With a separation distance of ~ 50 km this lag is on the same order as the lag seen in peak storm conditions at buoys 44025 and 44009. Peak sediment transport was associated with a combination of a maximum in suspended sediment concentration and high relative along-shelf southwestward currents. The nearly coincident maximum in sediment transport suggests that along-shelf transport is a common feature of the entire NJ shelf and MAB and is consistent with previous modeling studies [*e.g. Keen and Glenn*, 1995]. The event duration is longer than the temporal lag between the southern and northern gliders so the large-scale storm effectively forces the shelf as a whole and there is little spatial variability in the timing of resuspension and transport as a result of storm passage.

While resuspension and transport occurred with an approximately eight hour lag, the strength of resuspension and transport varied by as much as a factor of two in the along-shelf direction, with higher transport associated with RU05 located on the southern NJ shelf. The major difference in sediment resuspension, and consequent transport, was related to the numerous discrete resuspension events

that resulted in high sediment concentrations up into the water-column during the storm. The difference in the scale and frequency of resuspension events over spatial scales much smaller than the storm event points out the importance of local processes, which affect the magnitude of sediment resuspension and transport. Previous work by [*Keen and Glenn*, 1995; *Gargett et al.*, 2004; *Styles and Glenn*, 2005] have highlighted tidal forcing, topographic variations and Langmuir cells as potential processes affecting sediment resuspension and transport on time-periods shorter than a day. For both gliders, vertical velocity variability appeared random rather than spatially banded (Figure 2.7, 2.9), indicating that Langmuir cells were not likely the cause of the suspended sediment spatial heterogeneity. RU21 and RU05 were both flying approximately southwestward along the 40 m isobath during elevated winds, currents and waves therefore topography was essentially constant during the resuspension event (Figure 2.7, 2.9). RU21 did not experience fluctuations of sediment resuspension or transport on time-scales shorter than a day after the resuspension event was initiated, thus tidal forcing was not likely a dominant modulation process as in Keen and Glenn (1995). The scale of tidal forcing on the shelf is also much larger than the separation distance between the gliders; therefore variability seen in RU05 on shorter time-scales is likely not related to tidal fluctuations.

     Glenn et al. (2008) suggested that in the absence of stratification, turbulence in the combined wind-driven surface layer and wave-enhanced bottom boundary layer is responsible for sediment resuspension upward through the water column, but observations were sparse. During the Nor'Ida storm there was a distinct change

in vertical glider velocities, which serves as evidence of turbulence in the water column. The standard deviation of each three-hour glider segment for RU21 and RU05 vertical velocities show a distinct increase in vertical velocity variability beginning on the morning of the 12th and persisting through the 16th (Figure 2.12). These fluctuations in the glider's vertical velocity serve as an estimate of the turbulent motions due to high storm-induced current-shear, similar to neutrally buoyant lagrangian floats used in [*Harcourt and D'Asaro*, 2010]. Vertical velocity standard deviation values were approximately the same for RU05 and RU21. Uniform vertical velocity standard deviations suggest that the vertical component of turbulence was similar between the northern and southern portions of the NJ shelf, which is consistent with the scale of the storm and the uniform winds, waves and currents.

With little variability in turbulent vertical velocities between gliders, the differences in bed grain size likely play a major role in modulating the magnitude of resuspension by storm-induced turbulence. In order to assess the importance of local variability in grain size we interpolate mapped values [*Reid et al.*, 2005; *Goff et al.*, 2008] plotted in Figure 2.1 to glider latitude and longitude. The resulting time-series (Figure 2.13) shows mean grain size below the gliders throughout the deployment. The time-series shows mean grain sizes ranged from ~0.3 to ~1.4 mm with largest grain sizes seen by RU05 after storm passage, when it turned into the mouth of the Delaware. RU21 passed over a region of over 1mm grain sizes between the 11th and 13th, after storm initiation but prior to peak conditions. The map in Figure 1 shows a patch of coarse sediment along the northern portion of the NJ shelf

where RU21 was flying and relatively smaller grain sizes in the along-shelf region

where RU05 sampled, prior to turning in toward Delaware Bay. During the

resuspension events on the 13th through the 15th, RU05 was located over a patch of

sand with a mean grain size of 0.3 mm to 0.4 mm (Figure 2.13) before flying through

a region with mean grain size of over 0.8 mm on the 15th. Conversely, RU21 was in a

region with mean grain sizes from 0.4 mm to 0.6 mm on the 13th.through 14th. On

the 15th RU21 entered a region of reduced mean grain size of ~0.3 m^{-1} and.

A study by *Agrawal and Pottsmith* (2000) as part of the LEO-15 project,

which took place within a few kilometers of the deployment location of RU05 and

RU21, developed a local model for the fall velocity:

$$w_{f,n} = 0.45 \times 10^{-3} a_n^{1.2} \qquad (2.2)$$

where a_n is the radius in microns and w_f is the settling velocity in cm s^{-1}. As

mentioned previously fall velocity is essentially the tendency of sediment to fall out

of concentration and u_* is the tendency for particles to remain in suspension.

Following the above equation we calculate fall velocities for the sediment grain sizes

mapped below the glider during the resuspension event on the 13th through 15th

(Figure 2.14). Fall velocities are initially greater for RU21 at the peak of the storm,

and initiation of the resuspension event at midnight on November 13th. As the

gliders progress fall velocities are approximately equal for RU21 and RU05 until the

14th when RU21 fall velocities increase and RU05 fall velocities decrease. While we

use the standard deviation of glider vertical velocities as a relative approximation of

the timing of turbulent motions, these values are not sufficient to directly substitute

for values of u_*. Lentz et al. (1999) uses depth-averaged velocities to estimate

bottom stress τ_b. If we follow this model and subsequently calculate a depth-averaged representative friction velocity then we would see u_* values proportional to glider velocities. A time-series of depth-averaged velocities during the storm event are shown in Figure 14. RU05 depth-averaged velocities are ~ 5-10 cm/s greater than RU21 through the 13th and are approximately equal on the 14th. As our depth-averaged velocities are only proportional to friction velocity we cannot calculate a direct ratio of $\frac{w_f}{u_*}$. For comparison, we calculated the ratio of RU21 to RU05 estimated fall velocities between the two gliders as well as the ratio of RU21 to RU05 depth-averaged glider velocities, which should be approximately equal to the ratio of friction velocities (Figure 2.14). Fall velocity ratios were initially high, similar to RU21 fall velocities and grain-size. From 4:00 to 22:00 GMT on the 13th fall velocity ratios are near one. On the 14th the RU21 to RU05 fall velocity ratio increased by over a factor of two, until they drop again late on the 14th as the gliders began to turn onshore. The ratio of RU21 to RU05 depth-averaged glider velocities was just below one for the duration of the resuspension event on November 13th through the 14th. Calculated standard deviations of RU21 to RU05 fall velocities and depth-averaged glider velocities are 0.62 and 0.08 respectively. The much larger standard deviation in the estimated fall velocity ratio shows that differences in grain size and subsequently fall velocity plays a larger role than current variability in the resuspension and transport dynamics during this storm event. Comparison of our fall velocity ratio to slopes of optical backscatter profiles in Figure 2.8 and 2.9 for RU21 and RU05 respectively, show that profiles were Rouse-like throughout the water column for the 13th and 14th for RU05. These profiles are indicative of full

water column resuspension of relatively smaller particles, which remained in suspension for the duration of the event. Optical backscatter profiles from RU21 were much more vertical than RU05 until mid-day on the 14th when resuspension peaked throughout the water column. Later on the 14th and into the 15th profiles of RU21 optical backscatter demonstrated a near bottom layer, which along with fall velocities indicates that larger particles were falling out of suspension or unable to make it into the upper portion of the water column. The differences in grain size and resuspension characteristics from the northern glider, RU21 and southern glider RU05 show that even during the largest storms local variability in bed characteristics can play a major role in modulating sediment resuspension and subsequently transport on the continental shelf. Our study demonstrates that during storms on the continental shelf, variability in bottom character also drives local variability in the magnitude and direction of sediment transport. Through glider spatial surveys of sediment transport and resuspension, we have shown that detailed spatial surveys and continually updated spatial maps similar to those produced by *Goff et al.* (2008) may be necessary to fully understand water-column sediment transport. These spatial surveys will not only support further understanding of observational data over shelf-wide spatial scales, but can also be used to quantitatively enhance realistic regional sediment resuspension and transport models.

2.5 Conclusion

Here we have demonstrated the importance of utilizing novel ocean observation technology, such as gliders and CODAR to resolve shelf-scale

resuspension and transport during storms. A fleet of autonomous gliders not only provided information on sediment transport and resuspension over large spatial areas, but also emphasized the importance of local variability in grain-size on estimates of shelf-wide sediment resuspension and transport, even in the largest storms. With little observed influence from tides, Langmuir cells or topography, the simple balance between turbulent shear stress and fall velocity, which varies with grain-size, played a major role in observed differences in sediment resuspension and transport along the mid-shelf. Future inclusion of glider fleets and CODAR networks along with traditional tripod and buoy instrumentation will allow for a more holistic view of sediment transport and resuspension along continental shelves, during storm events in particular, when shipboard measurements are not possible. These data will also aid in developing more robust regional models by feeding real data into predictive models as storms occur. In order to further understand the dynamics of sediment resuspension and transport on shelf-wide scales, the inclusion of acoustic and holographic sensors in addition to optical sensors on glider platforms will be necessary. This will help to accurately identify the nature of suspended particles when sediment bed information is lacking and will also provide more *in situ* information regarding the magnitude and direction of current profiles and transport during storm events.
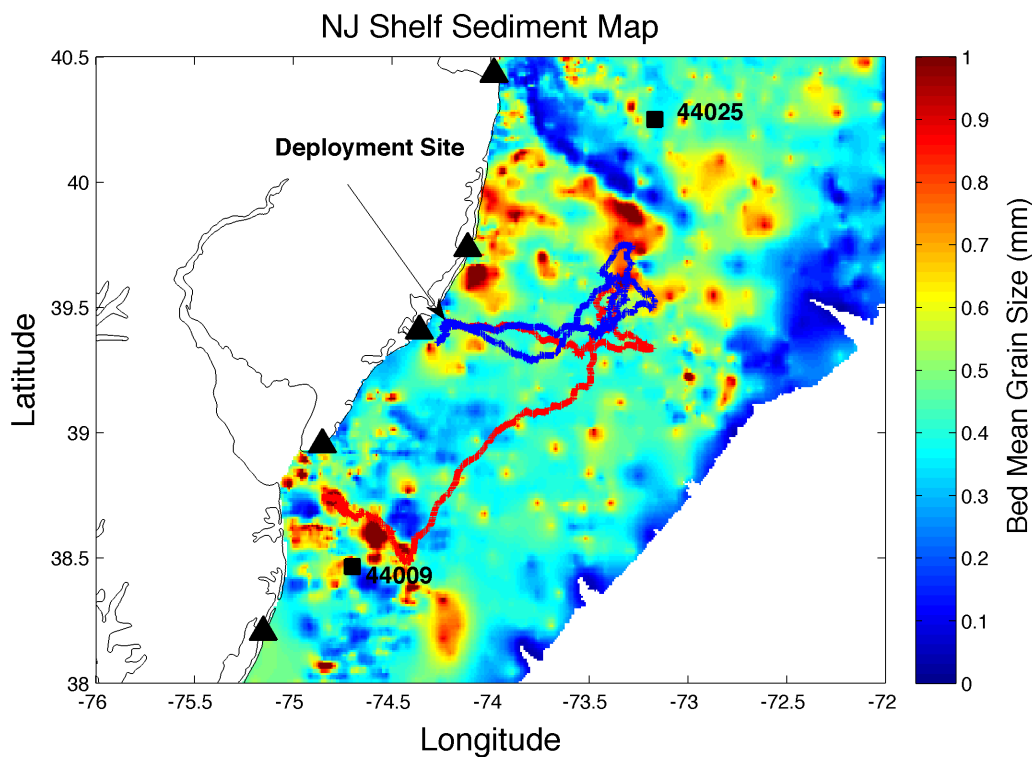
NJ Shelf Sediment Map

Figure 2.1. The study location and 2 km resolution mean grain size map in mm with glider tracks from RU05(red), RU21 (blue), CODAR locations within the study region (black triangles) and Buoys 44009 and 44025 (black squares). Only CODAR stations in the immediate vicinity are shown, though others contributed to the data. The deployment site for both gliders is off Tuckerton, NJ. RU21 was recovered near the deployment site while RU05 was recovered in the south off of Delaware Bay, near buoy 44009. Details of sediment compilation from the usSEABED program are covered in Goff et al. (2008).
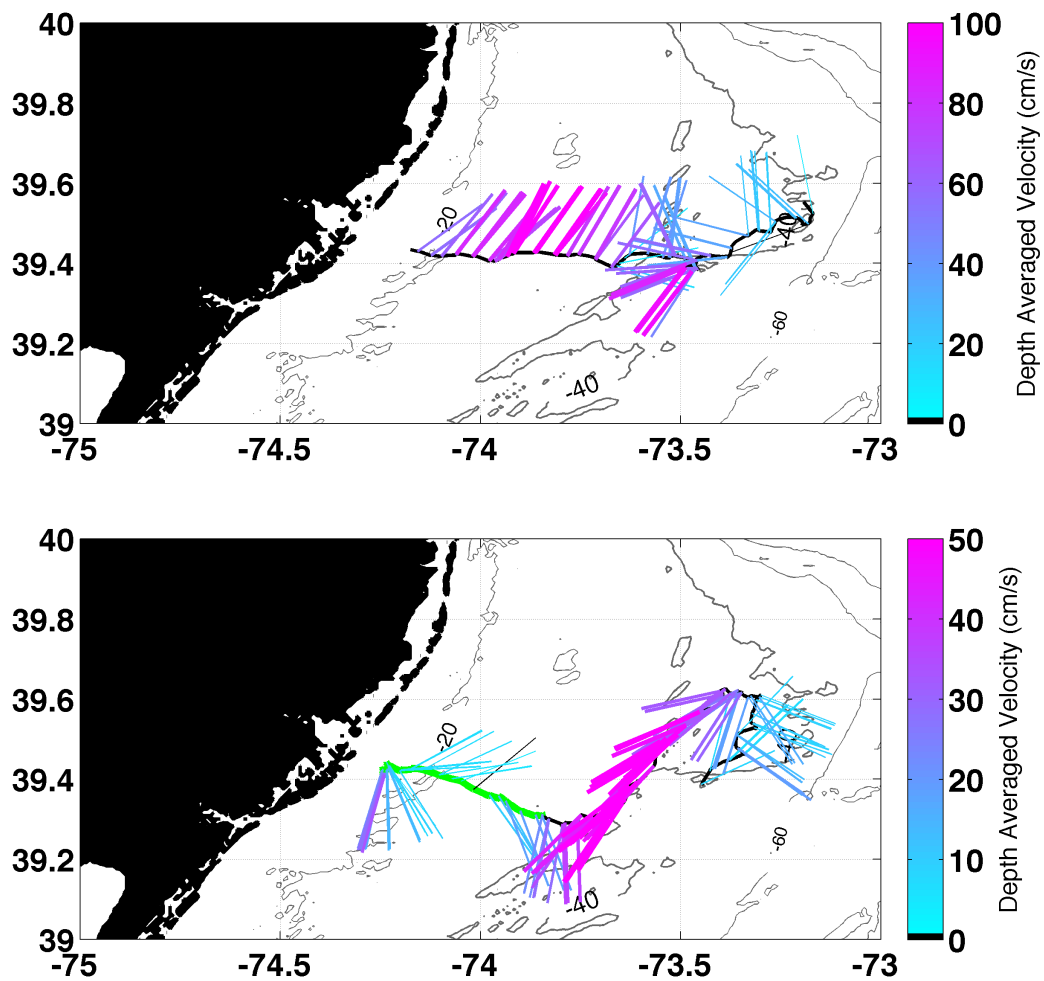
Figure 2.2 RU21 depth averaged currents and offshore glider track from 10/31 to 11/05 (Top Panel) and onshore glider track from 11/10 to 11/18 (Bottom Panel). The green line indicates the portion of the transect from 11/15 to 11/18.
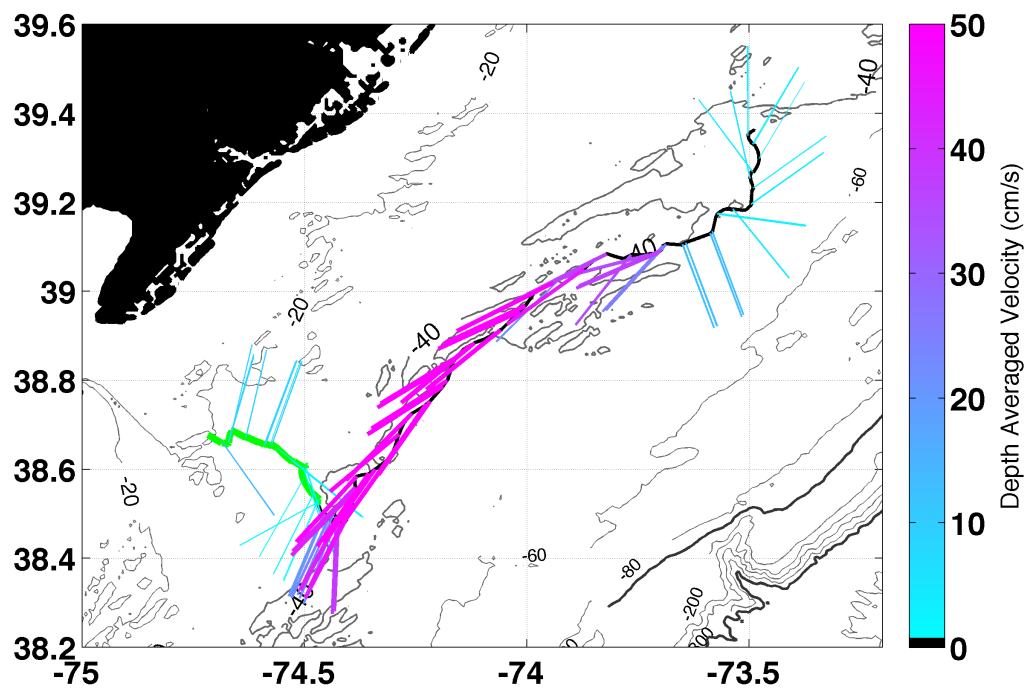
Figure 2.3 RU05 glider track and depth-averaged currents between 11/10 and 11/18. The green line indicates the onshore glider track on 11/16 to 11/18.
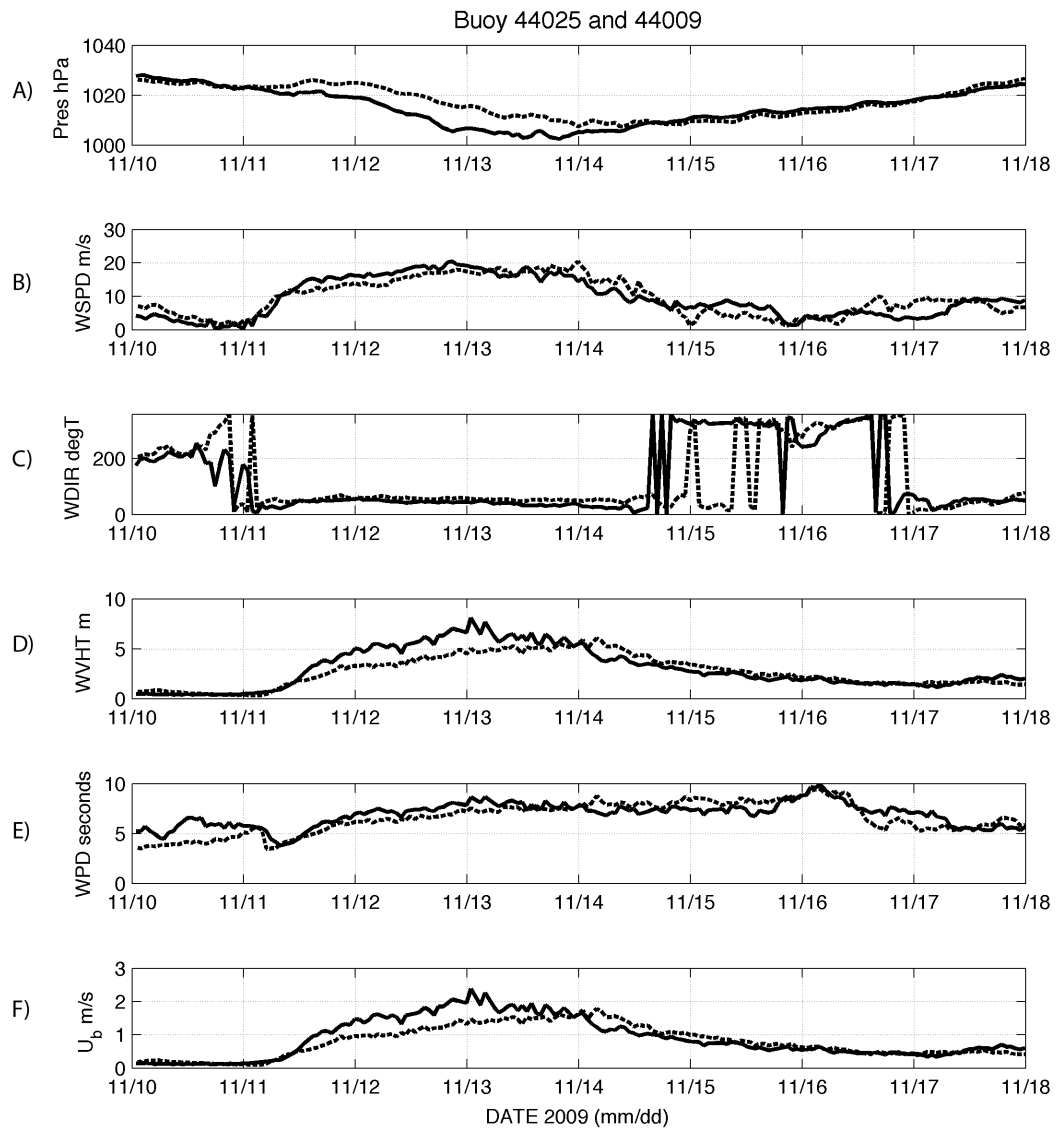
Figure 2.4 Buoy 44009 (solid line) and 44025 (dashed line) (A) pressure, (B) wind speed, (C) wind direction (D) wave height (E) wave period and (F) bottom orbital velocities for 11/10 to 11/18.

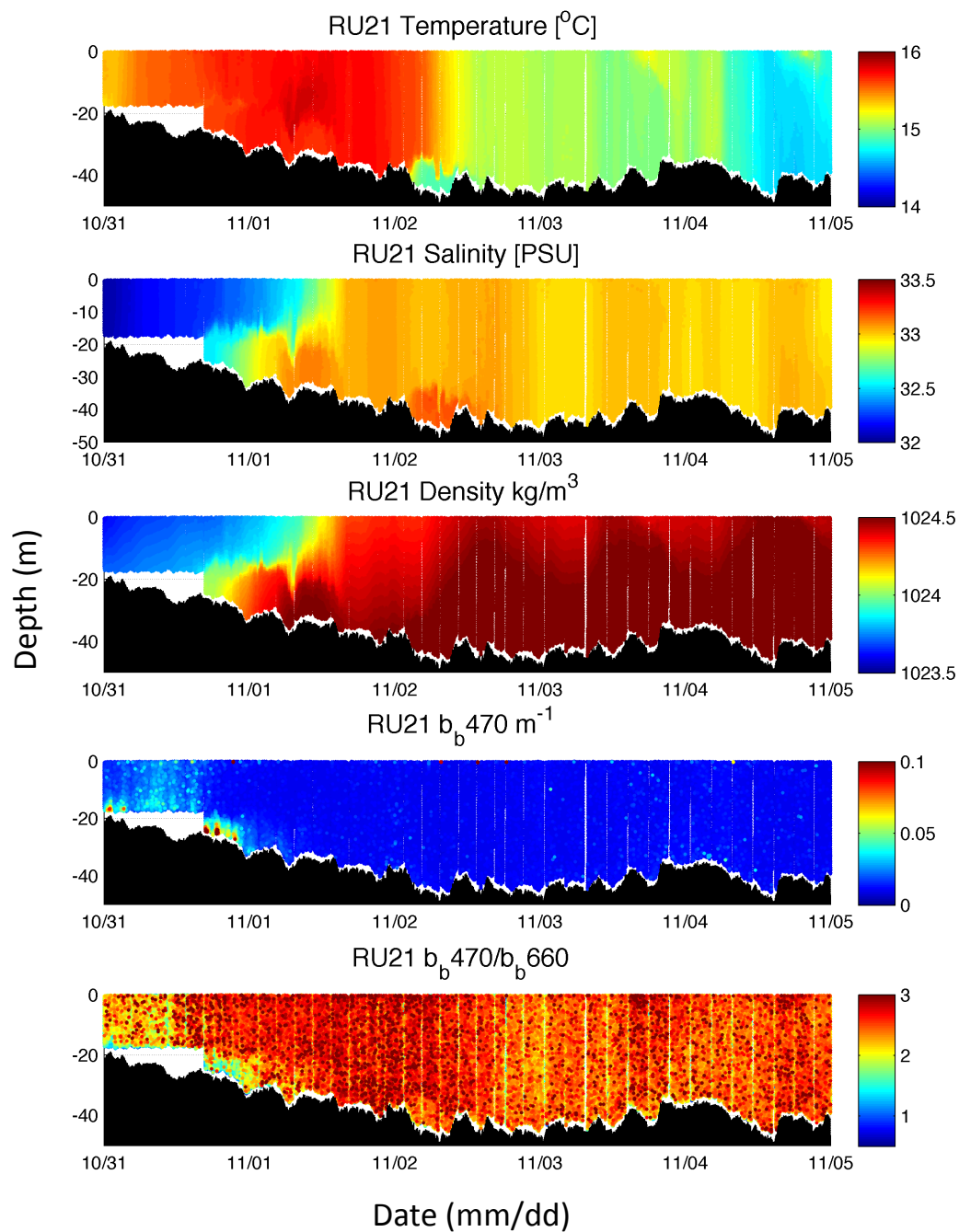**Figure 2.5** RU21 Pre-storm cross sections of temperature, salinity, density, b_b470 and the ratio of b_b470/b_b660.
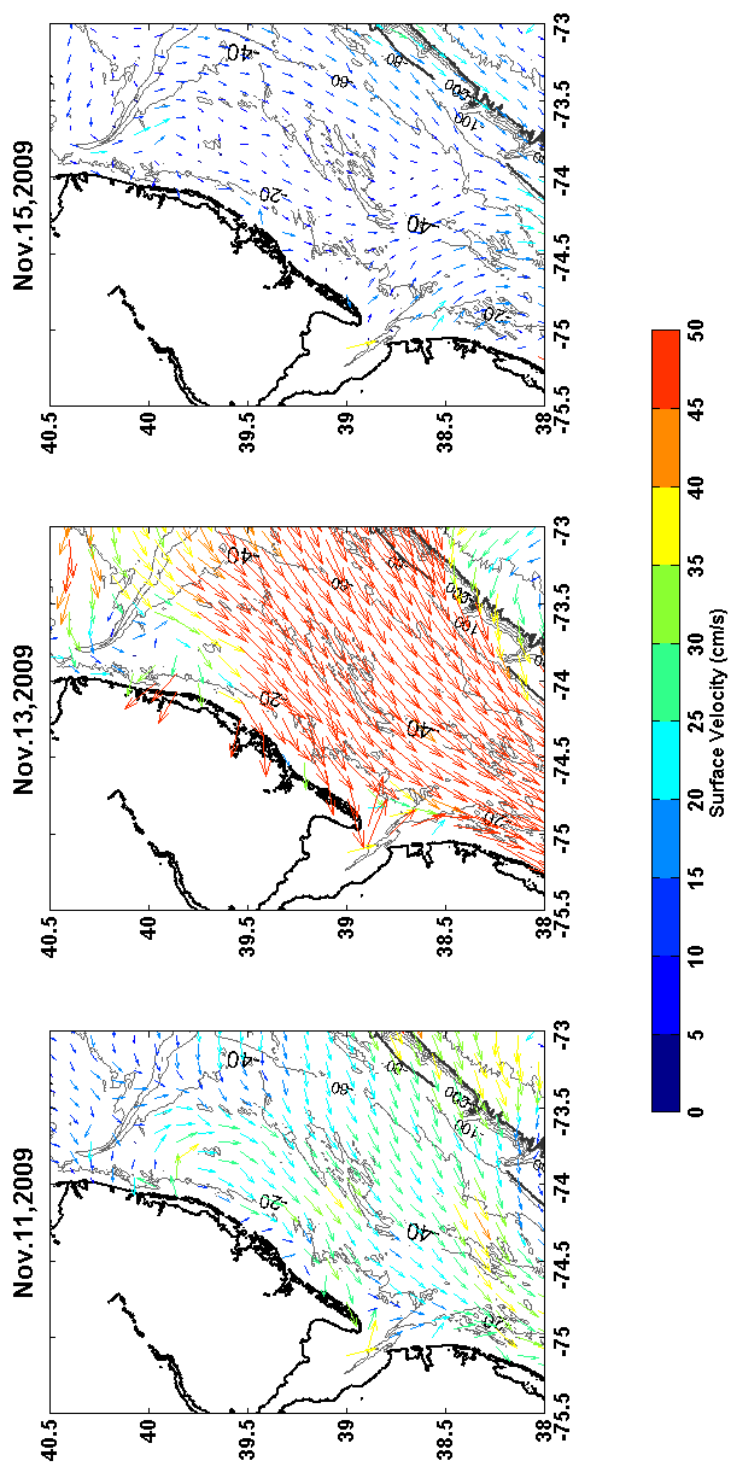
Figure 2.6 Daily averaged CODAR surface currents for the New Jersey shelf for Nov. 11th 13th and the 15th.
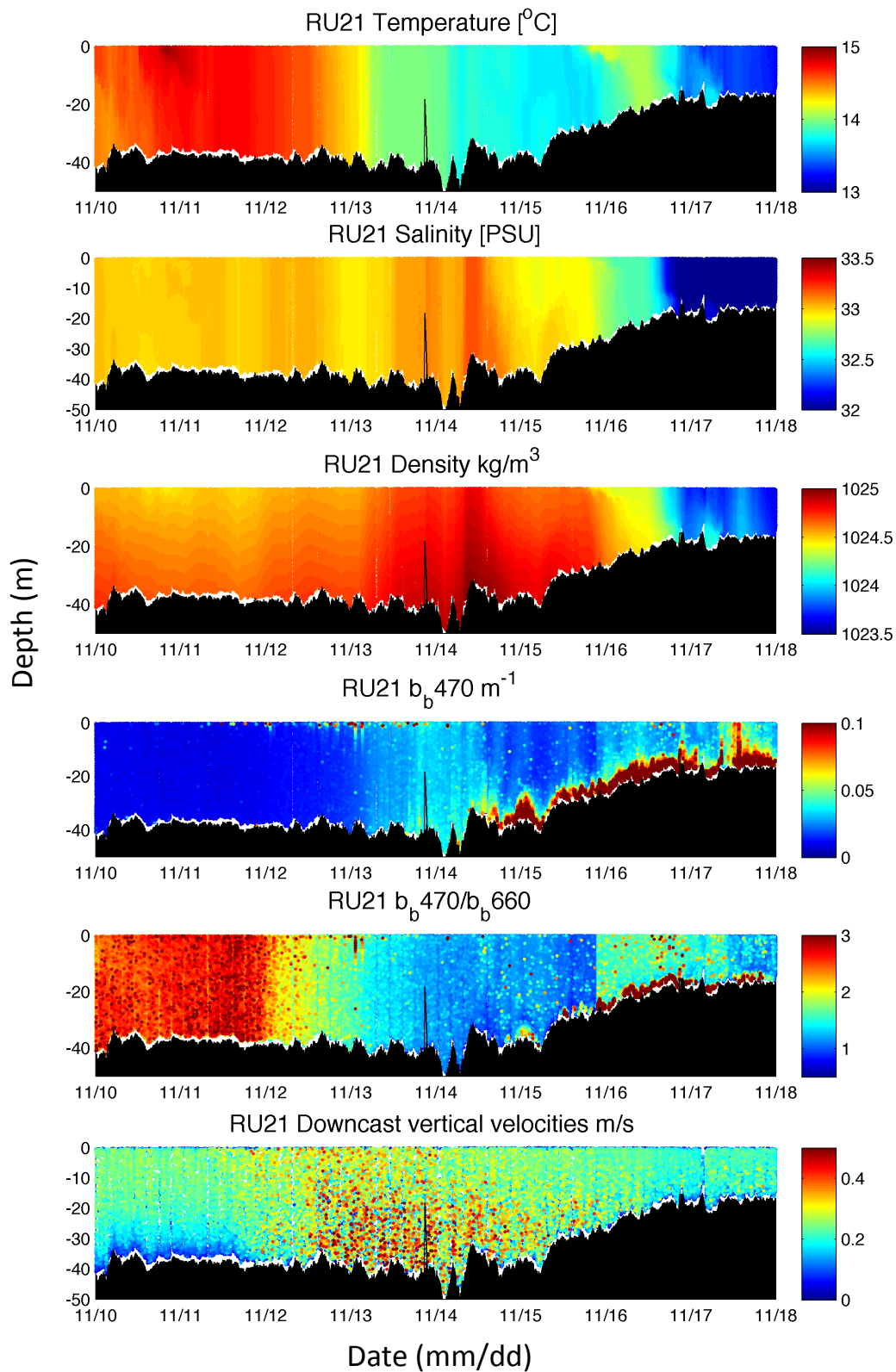
Figure 2.7 RU21 during and post-storm cross-sections of temperature, salinity, density, b_b470, b_b470/b_b660 and downcast glider vertical velocities.

Figure 2.8 RU21 log-normalized profiles of optical backscatter at b_b470 (red) and b_b660 (black). Y-axis is the natural logarithm of depth divided by z_r , a reference depth of 3.5 meters. The X-axis is the natural logarithm of optical backscatter, b_b, divided by the optical backscatter at the reference depth b_r or $\ln(b/b_{zr})$. Titles are timestamps of November dd HH:MM.
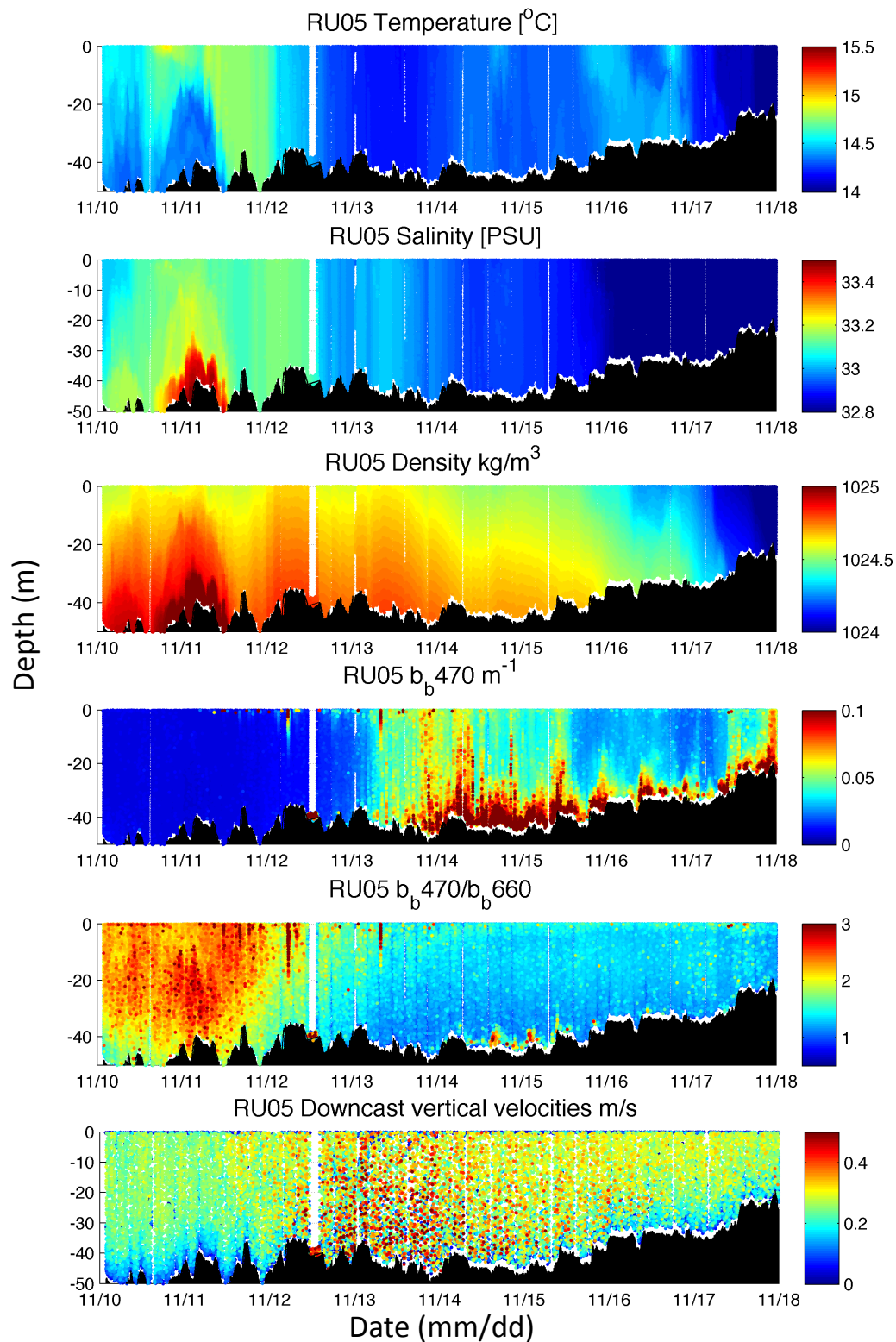
Figure 2.9 RU05 cross-section of temperature, salinity, density, b_b470, b_b470/b_b660 and downcast glider vertical velocities.

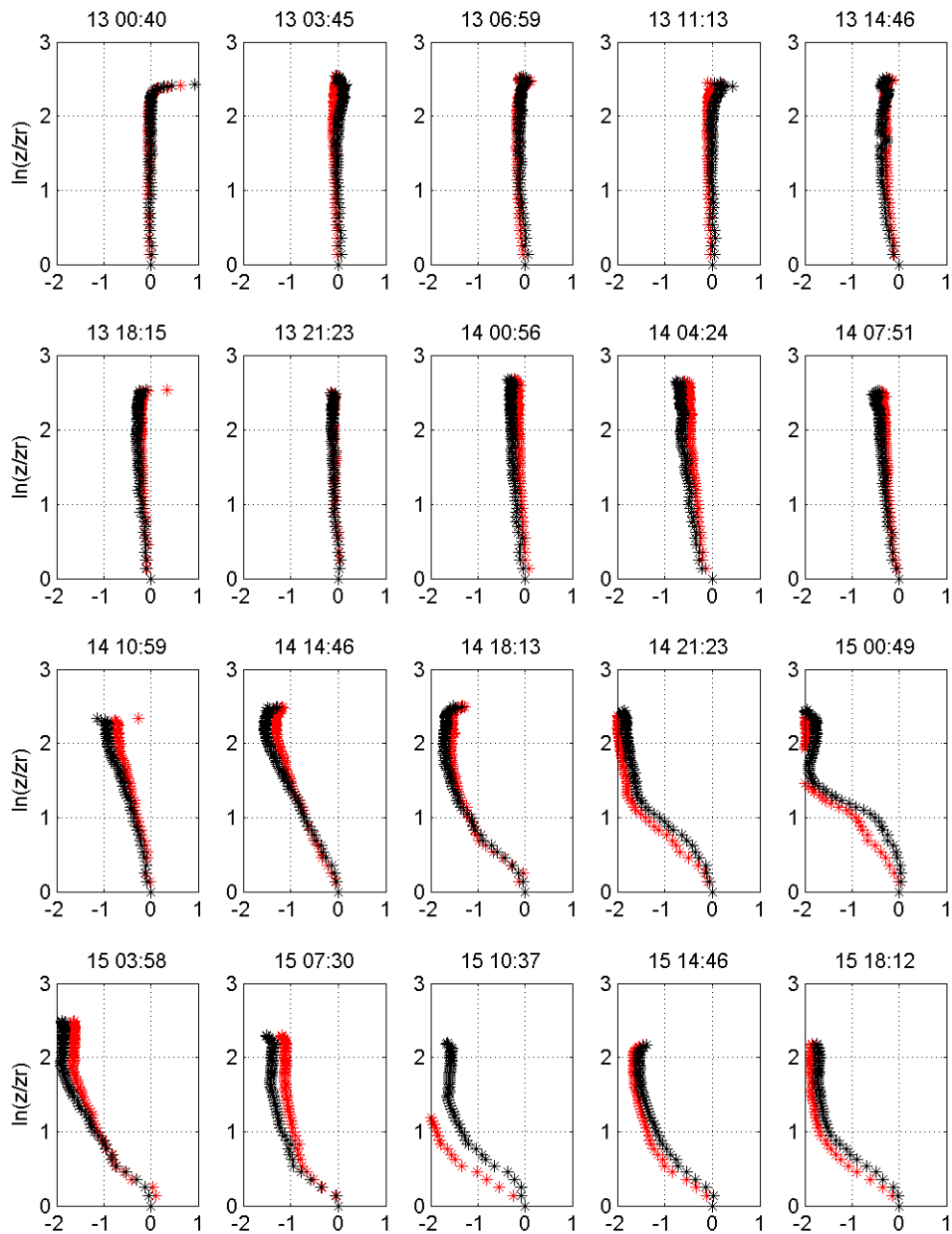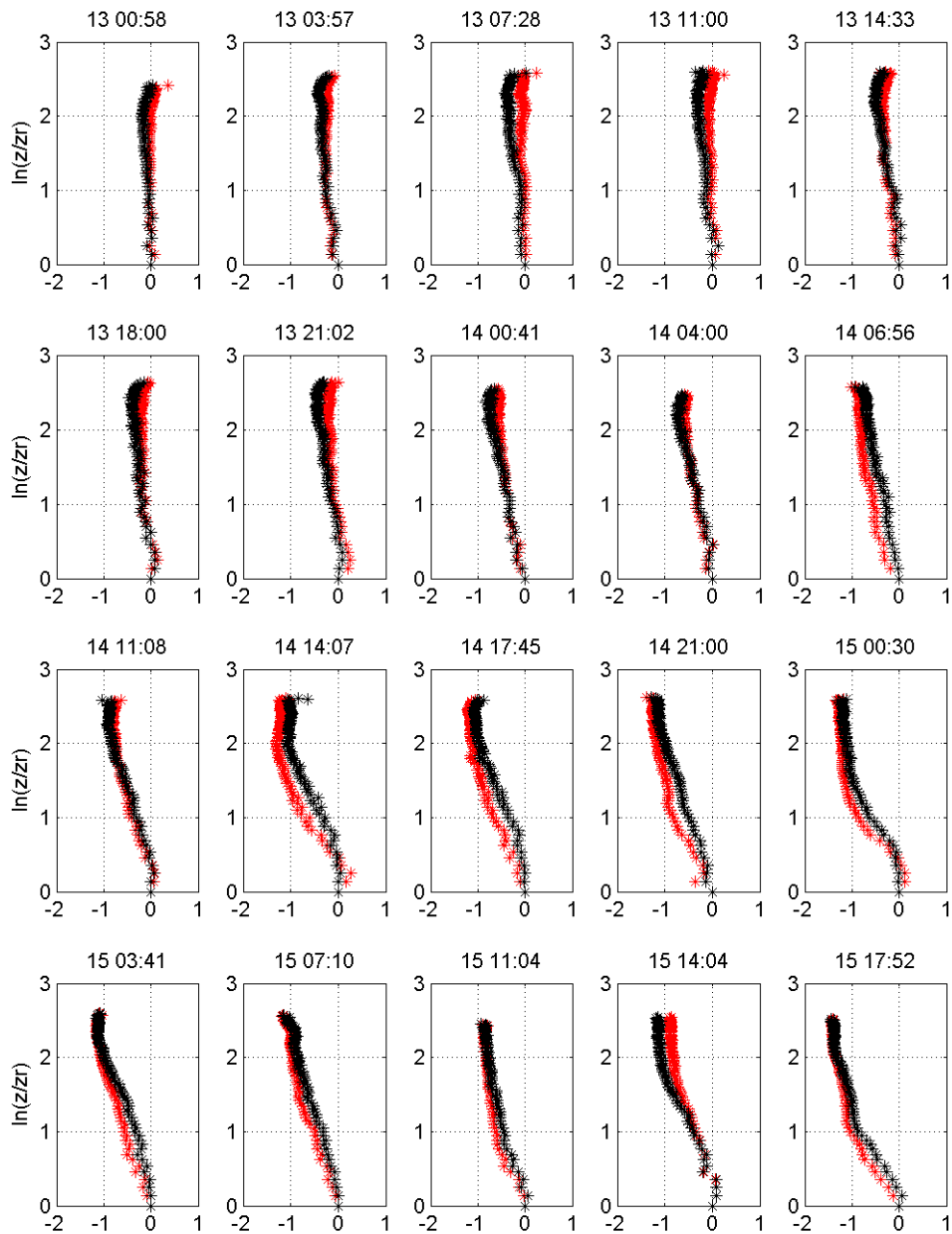**Fig 2.10** RU05 log-normalized profiles of b_b470 (red) and b_b660 (black). Y-axis is the natural logarithm of depth divided by z_r, a reference depth of 3.5 meters. The X-axis is the natural logarithm of optical backscatter, b_b, divided by the optical backscatter at the reference depth b_r or $\ln(b/b_{zr})$. Titles are timestamps of November dd HH:MM.
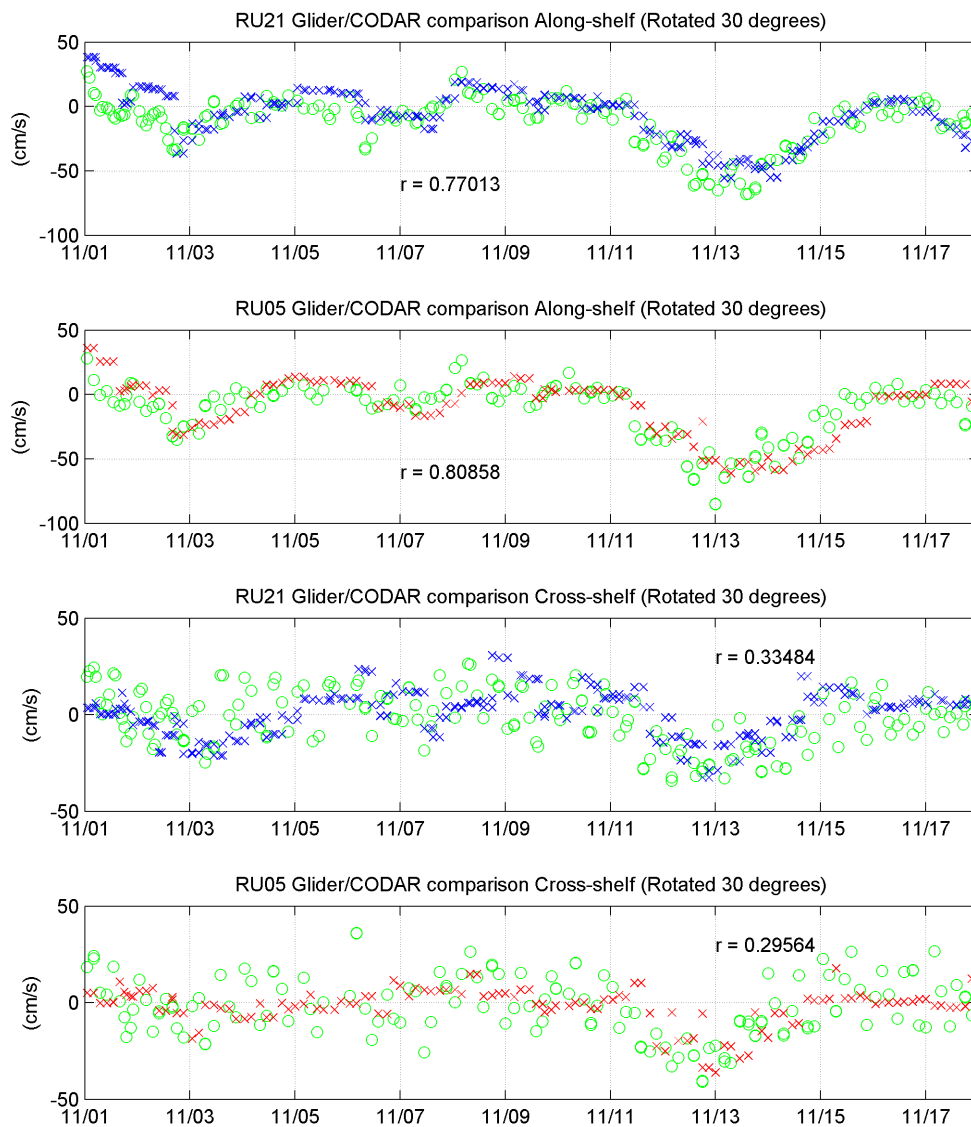
Figure 2.11 Along-shelf currents for RU21 and RU05 (Top two panels) and cross-shelf currents for RU21 and RU05 (Bottom two panels) depth averaged glider currents(x's) and along-track 3-hourly averaged CODAR surface currents (o's) rotated clockwise 30 degrees to be in the cross- and along- shelf directions with positive along-shelf currents to the northeast and positive cross-shelf currents to the southeast. Correlation coefficients for the full time-period are displayed as r.
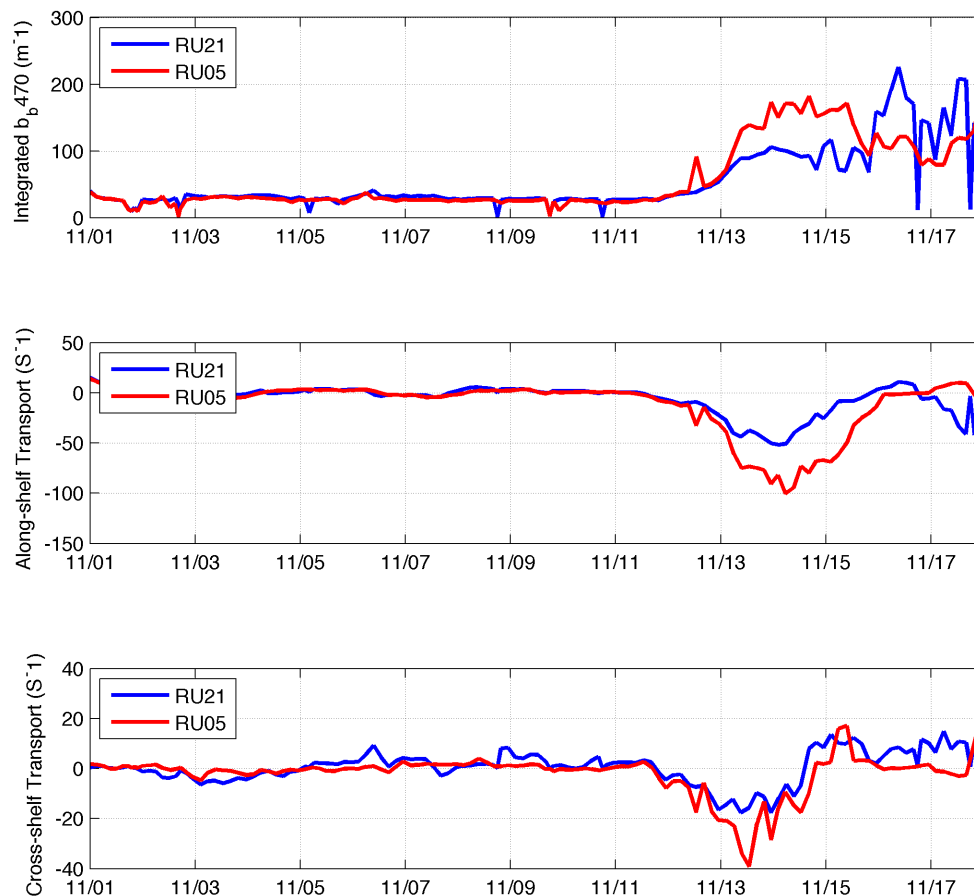
Figure 2.12 Time-series of the (blue) RU21 and (red) RU05 (top) three-hour integrated b_b470 (m^{-1}) and estimated transport in the (middle) along- and (bottom) cross- shelf directions. Positive values indicate northeastward transport for along-shelf and southeastward transport for cross-shelf transport. Estimated transport is calculated by multiplying depth-averaged glider currents by integrated optical backscatter at b_b470.
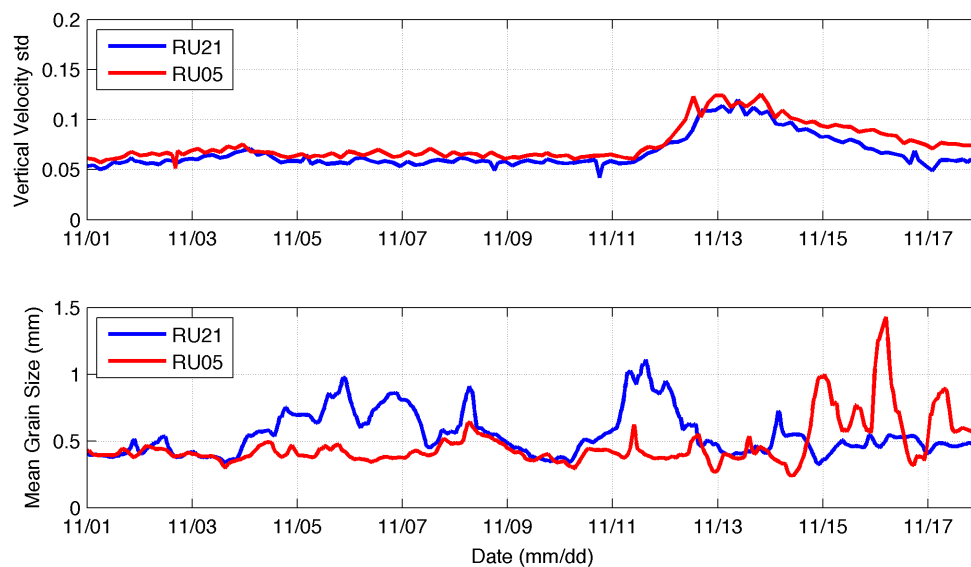
Figure 2.13 Time-series of the (blue) RU21 and (red) RU05 (top) three-hour segment standard deviation of vertical velocity (cm s^{-1}) and (bottom) mean bed grain-size from Figure 1 interpolated to the along-track glider positions.
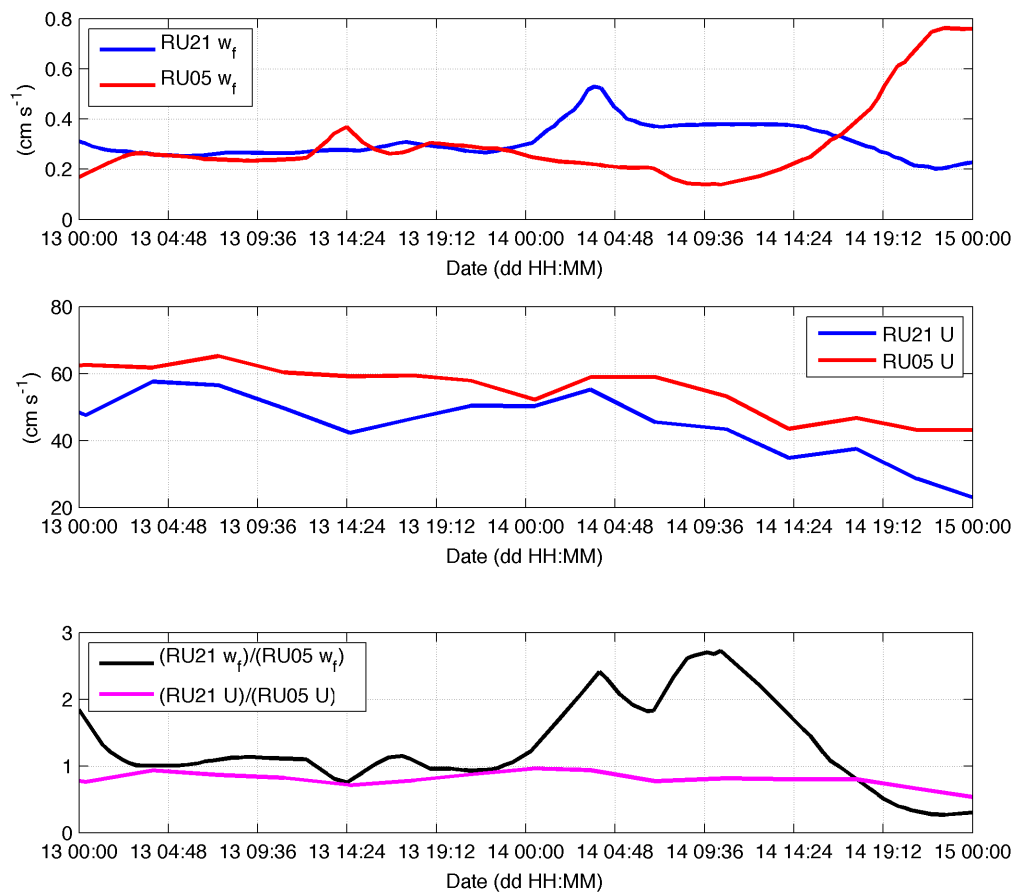
Figure 2.14 Time-series of (top) estimated fall velocities for (blue) RU21 and (red) RU05, (middle) magnitude of depth-averaged currents for (blue) RU21 and (red) RU05, and (bottom) the ratio of (black) RU21 to RU05 fall velocities and (magenta) depth-averaged currents, all during the resuspension event.

Chapter 3

Offshore advection of cold bottom water ahead of Hurricane Sandy

3.1 Introduction

Tropical and extra-tropical cyclones are important episodic events for sediment

transport [*Traykovski et al.*, 1999; *Styles and Glenn*, 2005; *Traykovski*, 2007; *Glenn et al.*, 2008; *Miles et al.*, 2013] and coastal ocean mixing. These storms may also play a

critical role in initiation of the fall phytoplankton bloom directly [*Babin*, 2004] or

indirectly by eroding summer stratification and allowing nutrients to replenish the

shallow coastal ocean [*Xu et al.*, 2011]. Despite the importance of such events, *in situ*

observations of the coastal ocean response to these storms are rare, primarily due

to difficulty in safely sampling in extreme conditions.

Observations in the deep ocean during large storms are commonly made

with airborne expendable bathythermograph (AXBT) [*Cione and Uhlhorn*, 2003] or

surface and profiling drifters also deployed by aircraft [*D'Asaro et al.*, 2007; *Sanford et al.*, 2007, 2011]. These observations have aided in development of new

parameterizations [*Black et al.*, 2007] and aided in a dramatic decline in storm

induced human fatalities [*Walker*, 2006; *Keim et al.*, 2007], but they are largely

limited to the deep ocean off of continental shelves. In near shore regions (< 100 m)

opportunistically placed moorings [*Kohut et al.*, 2006; *Jarosz et al.*, 2007] or cabled

observations have captured storm events at single locations. While data from these

systems are critical to understanding storm development they rely on placement

weeks to months before storms, cannot be adapted based on storm track forecasts and can be expensive to maintain.

Recent studies have used autonomous-underwater-vehicles, specifically Teledyne-Webb Research Slocum gliders to adaptively sample the coastal water-column before, during and after storms in a variety of regions and conditions [*Glenn et al.*, 2008; *Ruiz et al.*, 2012; *Miles et al.*, 2013]. These instruments have not only provided a wealth of data, but they are capable of real-time data transmission that may be assimilated into ocean models [*Gangopadhyay et al.*, 2013].

In October of 2012, we had the unique opportunity to deploy a glider in rapid response to Hurricane Sandy, the second costliest storm to make landfall in the United States. In addition to standard sensor packages included on Slocum Gliders, we mounted an upward looking Nortek Aquadopp current profiler (Aquadopp) to collect depth dependent current information beneath the storm. In this paper we use this glider along with other regional observational assets to detail the temperature evolution of the water-column beneath Sandy as well as the time-evolution of the current structure beneath the storm.

3.1.1 Synoptic Conditions

Hurricane Sandy developed as a tropical wave off the coast of Africa on October 11th 2012 and made landfall in Jamaica as a category 1 Hurricane on October 24th. As Sandy made landfall in Cuba as a category 3 hurricane on October 25th. Sandy transited parallel to the east coast of the United States and passed the North Carolina coast on October 28th. At this point the storm had maximum winds extending over 150 kilometers from the eye center and tropical storm force winds

extending over 500 kilometers. On October 29th Sandy made a turn to the west-northwest toward the NJ coast. The eye of Hurricane Sandy passed between buoys 44009 and 44025, off Delaware Bay and New York Harbor respectively (Figure 3.1), and was less than 50 kilometers south of our glider, RU23 (Figure 3.1). The National Hurricane Center (NHC) designated Sandy as 'post-tropical' as it made landfall over Brigantine, NJ at 23:30 GMT on October 29th. Despite this designation Sandy had the lowest central pressure on record for the region (945 mb), and made landfall at astronomical high tide, which maximized the storm surge impact on coastal communities [*Blake et al.*, 2013].

3.2 Instrumentation

3.2.1 Gliders

Teledyne-Webb Research Slocum gliders are buoyancy driven autonomous underwater vehicles that are mobile profiling sensor platforms, with interchangeable science bays [*Schofield et al.*, 2007, 2010a] that are ideally suited to shallow coastal applications. Two gliders, Darwin and RU23, provided data for this study (Figure 3.1). Darwin was equipped with a standard Seabird Electronics (SBE) conductivity, temperature and depth (CTD) sensor and Wetlabs Ecopuck, which uses fluorescence excitation and emission to estimate chlorophyll concentration. RU23 was also equipped with an SBE-CTD and Wetlabs Ecopuck as well as an additional Optical Backscatter puck (BB3). Darwin was piloted in a cross-shelf trajectory from the shelf-break on October 13th 2012 (73.5^o West and 38.75^o North) to near-shore on October 22nd 2012 (74° West and 39.75^o North) and surfaced every 6 hours. RU23 was deployed on the southern flank of the Hudson Shelf Valley

(73.75^o West and 40.1^o North) on October 25th 2012 and transited along the 40

meter isobath southeastward until it was advected southwestward until the end of

the storm period on October 30th at 12:00 GMT to 73.6^o West and 39.4^o North. RU23

was programed to surface approximately hourly in an effort to resolve tidal

variability, and insure high temporal resolution.

3.2.2 Aquadopp Current Calculations

To measure water-column currents a 2 MHz Nortek Aquadopp current profiler with

a custom glider head was mounted on RU23 in an upward looking orientation and

logged data internally. The Aquadopp was configured to collect data in beam

coordinates in one meter bins with a beam length of ten meters every two seconds.

On downcasts with a glider pitch angle of 26.5^o the Aquadopp had a pitch angle of

0°. We employ a shear-least squares method originally detailed for lowered current

profilers [*Visbeck*, 2002] and adapted for use on autonomous platforms [*Todd et al.*,

2011a] in order to estimate realistic currents from the glider mounted Aquadopp.

The shear-least squares method provides an estimate of the depth varying

currents only for each segment and must be referenced to depth independent

currents to obtain realistic water column velocities. To obtain the depth

independent velocities we used a combination of pitch angle, heading and depth to

calculate depth and time averaged currents each segment using a technique known

as dead-reckoning [*Sherman et al.*, 2001; *Davis et al.*, 2003]. Generally, glider dead

reckoning is done by taking the dive position from the dive latitude and longitude

position, calculating horizontal displacement underwater using a calculated vertical

dive speed using $\partial p / \partial t$ and a set pitch angle. When the glider surfaces the

difference between the estimated position from the horizontal displacement calculation and the actual surfacing latitude and longitude is used as the estimated displacement due to the background depth averaged current while the glider was underwater. External mounting of the Aquadopp likely increased drag on the glider and altered the actual glide angle relative to the programmed pitch angle, thus resulting in a heading dependent bias in dead-reckoned currents. Qualitative comparisons to past glider deployments suggested the glider horizontal speeds were reduced by approximately a third. Glide angle is the actual dive angle through the water and angle of attack is the difference between the programmed pitch angle and the glide angle. A detailed explanation of glider flight dynamics can be found in *Sherman et al.* (2001). Previous studies with Spray gliders [*Todd et al.*, 2011a] observed this bias and adjusted angle of attack for each current calculation. In order to account for this bias we iteratively re-calculated dead-reckoned currents, adjusting angle of attack by 0.2 degrees on each iteration. We then took the variance of each time series of depth-averaged currents and use the angle of attack that generates the minimum variance to calculate our 'unbiased' dead-reckoned currents. The angle of attack that yields the minimum variance for our deployment is near 7.6 degrees which is quite large relative to a typical angle of attack of 1-3 degrees for a glider with no externally mounted sensors. This number should be approached with caution as these estimates are glider specific and cannot be applied uniformly.

After corrections are made and dead-reckoned currents are calculated for each segment, shear currents are then referenced to dead-reckoned currents to

estimate realistic water column velocities. During the storm we programmed RU23 to surface at hourly intervals to increase dead-reckoned data resolution. All glider and Aquadopp data were interpolated to one hour and one meter bins using a Gaussian weighting function with one-meter vertical radius and one hour temporal radius. We used least squares to remove the barotropic tidal component from all depth bins. Impacts of baroclinic tides may be present, but in the context of storm current speeds of between well over 0.5 ms^{-1} previously seen on the shelf [*Miles et al.*, 2013] we expect them to have little impact on the final results. For studies that focus on processes with weaker (O10 cm s^{-1}) mean velocities these uncertainties cannot be ignored. Currents were rotated 30° clockwise from North to align approximately along and cross shelf.

3.2.3 Additional Observational Assets

Buoy data were obtained from National Oceanographic and Atmospheric Association (NOAA) National Data Buoy Center (NDBC) buoys 44009 off Delaware Bay and 44025 off Long Island. These buoys collected standard meteorological data including atmospheric pressure, temperature, winds, wave-heights, wave-period wave-direction and sea-surface temperature (SST). Winds were rotated 30° clockwise from north to align along- and cross- shelf and are reported in direction toward with positive values northeastward and offshore, respectively. Coastal Sea-level height data (mean lower low water) were used from NOAA pressure gauges in Cape May, NJ and Sandy Hook, NJ. Satellite data, presented in Figure 3.1, is from the NOAA-18 and NOAA-19 Advanced Very High Resolution Radiometer (AVHRR) 3-day coldest-pixel composite from October 24th to the 26th 2012. Surface currents were

measured using 5MHz High-Frequency radar stations along the Mid-Atlantic bight

with a nominal horizontal resolution of 6 kilometers and extending from near shore

to the shelf-break [*Barrick*, 1971a, 1971b; *Dzwonkowski et al.*, 2009a, 2009b; *Roarty*

et al., 2010].

3.2.4 Depth Averaged Momentum Balance

Previous studies [*Fandry and Steedman*, 1994; *Lentz et al.*, 1999; *Lentz*, 2001;

Kohut et al., 2006] have used the depth-averaged momentum equations to detail the

near-shore coastal ocean response to atmospheric forcing. The study *Kohut et al.*

(2006) uses these equations off the New Jersey Shelf during Tropical Storm Floyd. In

order to obtain an estimate of the force balances on the continental shelf in

Hurricane Sandy we assume the nonlinear terms are small and use the following

governing equations:

$$\frac{\partial u}{\partial t} = -g\frac{\partial \eta}{\partial x} + fv + \frac{\tau_{wx}}{\rho H} - \frac{\tau_{bx}}{\rho H} \qquad (3.1)$$

$$\frac{\partial v}{\partial t} = -g\frac{\partial \eta}{\partial y} - fu + \frac{\tau_{wy}}{\rho H} - \frac{\tau_{by}}{\rho H} \qquad (3.2)$$

With u and v as the cross-shore and along-shore depth-averaged velocities, g is

gravity, η is sea-surface height assuming a barotropic pressure gradient, f is the

Coriolis frequency, H is water-depth, τ_{wx} (τ_{wy}) is the cross-shelf (along-shelf) wind

stress and τ_{bx} (τ_{by}) is the cross-shelf (along-shelf) bottom stress.

We calculated wind stress at buoy 44025 following [*Fairall et al.*, 2003] for

high-wind conditions and used it to approximately represent wind at the glider

location, as both buoy and glider were on the northern side of the storm track, in the

vicinity of peak winds. To calculate depth averaged wind stress we divide the

surface wind stress from buoy 44025 by the along-track glider observed water-

column depth.

Our Aquadopp was oriented in an upward-looking position so as not to

obstruct measurements by the Ecopuck or BB3. The upward looking orientation

results in the lowest depth-bin measured approximately a meter above the glider

and limits our proximity and data near the bottom as the glider must begin to inflect

within 3 meters of the bottom. This makes observed log-profiles during extreme

forcing conditions difficult to obtain from a moving platform. Bottom stress can be

represented as:

$$\tau_b = \rho u_*^2 \qquad (3.3)$$

where u_* is the friction velocity. With a linear eddy viscosity and a constant stress

layer:

$$u_* = u(z)\kappa/\ln\left(\frac{z}{z_o}\right) \quad (3.4)$$

Where $u(z)$ is a near-bottom velocity at depth z, κ is Von Karman's constant of 0.4

and z_0 is the roughness length scale. Determination of z_0 has been the subject of

numerous studies over the past 40 years. As we only attempted to estimate the force

balances we used a roughness length z_0 of 0.1 cm similar to a study by *Kim et al.*

(1997) on the southern MAB and determined u_* from velocities and directions

measured 5 meters off the bottom. Future studies should include downward looking

current profilers in order to obtain more data in much closer proximity to the bottom. Validation in the vicinity of the bottom with more traditional bottom mounted current profilers or tripod systems are necessary.

We could not measure the sea-surface slope directly in the vicinity of the glider, but we estimate the magnitude of the alongshore sea-surface slope from coastal tide gauges at Sandy Hook, NJ, and Cape May, NJ, (Figure 3.1) and compare them to the inferred slope calculated by the residual necessary to balance the depth-averaged momentum equations. All terms were filtered with a 20 hour lowpass filter to highlight the large scale storm forcing and remove tidal and inertial signals.

Coriolis and acceleration terms were calculated directly from the depth-averaged glider velocities. We used a Coriolis frequency, f, of 10^{-4} to estimate the Coriolis force. Along- and cross- shelf accelerations were calculated by taking the hourly centered difference of the cross- and along- shelf depth-averaged velocities.

3.3 Results

3.3.1 Initial Ocean Conditions

Two weeks prior to the storm arrival, the glider Darwin, which was performing a cross-shelf transect from the shelf-break toward coastal NJ, measured surface temperatures over 18°C and a 30 meter deep upper-mixed layer. Bottom waters showed the presence of the remnant summer Cold Pool [*Houghton et al.*, 1982]. During the deployment this water mass extended from offshore of the 60 meter isobath to the 40 meter isobath with a cold core of 9°C at the 50 meter isobath (Figure 3.2). The depth of the thermocline (defined as the maximum per-meter temperature gradient along each profile greater than 0.25°C) varied between 20 and

30 meters for the majority of the cross-section with cooler (17°C) surface waters inshore and warmer (18 to 19°C) waters offshore. Three-day coldest-pixel composite satellite SST data collected for October 26th (Figure 3.1) showed cooler SST of 14 to 15°C on the northern portion of the MAB, off of Long Island and New York harbor. SSTs were warmer, between 18°C and 20°C, in the southern MAB and offshore toward the Gulf Stream. Surface currents from high frequency radar on October 22nd 2012 (not shown) were weak (~0.1 ms^{-1}) and variable in direction. These conditions are typical of the MAB transition period between late summer stratification, and well-mixed winter conditions [*Castelao et al.*, 2010].

3.3.2 Storm Observations

Winds at buoy 44009 and 44025 increased in intensity beginning late on October 27th (Figure 3.3) and were initially oriented along-shelf and downwelling favorable toward the southwest at both locations. Along-shelf winds persisted for over 24 hours. As the storm passed between buoys 44009 and 44025 late on October 29th winds rotated opposite directions, counter-clockwise to offshore and clockwise to onshore at buoy 44009 and 44025 respectively, with strongest sustained winds at buoy 44025 on the northern side of the storm in excess of 20 m s^{-1} and minimum pressures recorded at both buoys below 960 mb (not shown).

Cross-sections of RU23 temperature and currents (Figure 3.4) show three distinct time periods based on the evolution of the thermocline, which we refer to as T1, T2 and T3. The initial stratified period T1 was between 00:00 and 12:00 GMT on October 28th (over 36 hours before landfall) and showed warm surface temperatures of over 17°C consistent with pre-storm conditions sampled by Darwin

and a sharp thermocline at 25 meters depth (Figure 3.4A). Here we define the thermocline as the maximum per-meter temperature gradient along each profile greater that 0.25°C m^{-1}. Below the thermocline temperatures were 11°C and uniform to the bottom. During T1 de-tided along-shelf surface currents were weak and southwestward with flow below 0.1 m s^{-1}, while the lower layer showed bottom intensified flow over 0.2 m s^{-1} (Figure 3.4C). In the cross-shelf direction there was slight onshore flow near the surface and offshore flow near the bottom of ~ 0.1 m s^{-1} (Figure 3.4D).

During T2 between 18:00 GMT on October 28th and 06:00 GMT on October 29th (Figure 3.4A) the thermocline deepened, reaching the bottom in twelve hours. Along-shore currents increased to over 0.6 m s^{-1} in the surface layer and remained near 0.2 m s^{-1} in the bottom similar to the initial stratified phase (Figure 3.4C). In the cross-shelf direction (Figure 3.4D) currents were onshore in the surface near 0.3 m s^{-1} and offshore in the bottom layer near 0.3 m s^{-1}.

Between T2 and T3 the water column became uniformly well mixed with temperatures of near 15°C (Figure 3.4A) and currents transitioned from two-layer to one-layer flow (Figure 3.4C-D). Along-shelf currents peaked over 1 m s^{-1} toward the southwest and cross-shelf currents were onshore near 0.2 m s^{-1}.

Chlorophyll measurements from the glider showed concentrations of over 2 mg m^{-3} in the lower layer and little to no chlorophyll in the surface layer during T1 (Figure 3.4B). During T2 chlorophyll concentrations remained elevated in the lower layer and did not cross the stable thermocline despite the high wind forcing and tis deepening. Chlorophyll concentrations after the thermocline deepened were low

throughout the water-column. During T1 and T2 the observed distribution was likely a result of depleted nutrients in the surface and high nutrients in the remnant summer Cold Pool [*Falkowski et al.*, 1983], as well as near-bed concentrations being resuspended elevated storm forcing.

3.4 Forcing and Response

3.4.1 Cross-shelf Depth Averaged Momentum Balance

Beginning during T2, in the cross-shelf direction (Figure 3.5A) (positive offshore) the depth averaged Coriolis term was large, while acceleration, wind stress and bottom stress terms were an order of magnitude smaller. This resulted in Coriolis force being balanced by the calculated pressure gradient force. There were no direct measurements of sea-surface slope to confirm the estimated pressure gradient force, but winds were downwelling favorable (Figure 3.3), which were likely responsible for driving surface water onshore (evident in Figure 3.4D) and sea-levels at coastal tides stations (Figure 3.6) suggest that there was sea-surface setup along the coast. After the shelf was uniformly mixed during T3 (Figure 3.4A) the calculated pressure gradient force increased rapidly due to the removal of the near-bottom offshore flow and the transition to full water column onshore flow. A snapshot of High Frequency radar surface currents (Figure 3.7) prior to site outages along the coast generally supports the along-shelf geostrophic flow as a result of the balance between the Coriolis and pressure gradient force.

3.4.2 Along-shelf Depth Averaged Momentum Balance

As the storm approached there were clear shifts in the dominant forces in the along-shelf depth-averaged momentum balance (Figure 3.5B). Initially during T2 a

calculated positive along-shelf pressure gradient force balanced the wind stress and Coriolis force. The strong stratification as the storm approached kept observed bottom stresses low, as enhanced along-shelf southwestward currents were limited to the surface layer (Figure 3.4C). After the water-column near the glider became uniformly mixed during T3 along-shelf bottom stresses quickly increased. The positive bottom-stress, Coriolis and acceleration terms balanced the negative along-shelf wind stress and pressure gradient. As the eye of the storm passed the glider location between 18:00 GMT and landfall at 23:30 GMT on October 29th (Figure 3.1) acceleration terms became negative and wind stress became positive. Bottom stress remained high as the negative along-shelf pressure gradient and geostrophic cross-shelf balance continued to drive currents along-shelf toward the southwest.

To validate the calculated along-shelf depth-averaged pressure gradient term we compared it with a series of coastal tide gauges (Figure 3.6). We estimated the near shore pressure gradient force by calculating the de-tided sea-surface slope between Sandy Hook, NJ and Cape May, NJ. At the peak of the storm-surge there was a one-meter difference between the two locations, with a higher level at Sandy Hook, NJ in the north. These sites were separated by approximately 200 kilometers and the sea-surface slope calculated between the two locations yielded an estimated peak pressure gradient force of 6×10^5 m s^{-2} just prior to landfall on October 29th at 23:30 GMT, approximately a factor of two larger but on the same order of magnitude and similarly timed as the calculated pressure gradient force at the glider location (Figure 3.5B). The rotation of the winds (Figure 3.3) as the storm made landfall also supported a building sea-surface height on the northern NJ shelf with

onshore winds at buoy 44025, while offshore winds at buoy 44009 on the southern

NJ shelf supported a falling sea-surface height, which may have contributed to the

along-shelf sea-surface slope at landfall.

3.4.3 Mixing or Advection

An open question that may have implications for the ocean impact on atmospheric

forecasts, storm surge and the impact of storms on coastal nutrient regeneration is

whether the transition from stratified to well-mixed conditions was driven by

mixing of bottom Cold Pool water across the thermocline or advection of this

bottom water offshore. In order to assess this we calculate gradient Richardson

numbers across the stable thermocline following:

$$Ri = N^2/(\partial u/\partial z)^2 \qquad (3.5)$$

where N^2 is the maximum per-meter hourly averaged water-column buoyancy

frequency across the thermocline, and $(\partial u/\partial z)^2$ is the maximum per-meter hourly

averaged shear across the thermocline calculated from the Aquadopp. Studies that

use the gradient Richardson number [*Trowbridge*, 1992; *Chant et al.*, 2007]

generally consider the water column to be stable when Richardson numbers are

above 1 and unstable when Richardson numbers are below a critical Richardson

number of 0.25. Values between 1 and 0.25 generally indicate that mixing may be

occurring and are sensitive to the scale of the observations used in the calculation.

Richardson numbers were greater than one (Figure 3.8A) during T1 and T2 until

October 28th at 18:00 GMT and greater than 0.25 until October 29th at 06:00 GMT

consistent with the timing of the deepening of the thermocline and peak shear

currents observed by the Aquadopp (Figure 3.4A and 3.4D). As Richardson numbers

were between 1 and 0.25 while the thermocline was deepening this is not a definitive metric on whether mixing or advection were responsible for the transition from two- to one- layer.

A mixing dominated system should result in no net change in water-column temperature, and a decrease (increase) in surface (bottom) layer averaged temperatures. Layer averaged temperatures (Figure 3.8B) showed gradually decreasing temperature during T2 in the surface layer, while bottom temperatures stayed uniform until they increased dramatically from $\sim$11°C on October 29th at 00:00 GMT to over 15°C in just 6 hours. Total depth averaged temperatures increased over 1°C between 18:00 GMT on October 28th at 06:00 GMT on the 29th, which indicates there was a net increase in total water-column heat. While 1°C is not a large increase it is indicative that mixing was not the main process occurring as the thermocline was deepening.

Layer-averaged chlorophyll concentrations measured by the glider (Figure 3.8C) showed a net increase in the bottom layer concentration during T2, and a decrease from 2 mg l^{-1} to 0.5 mg l^{-1} between 06:00 and 07:00 GMT on October 29th, while concentrations stayed constant near 0.5 mg l^{-1} in the surface layer throughout the entire storm. Phytoplankton growth rates are on the order of one division per day [*Falkowski and Raven*, 2007], which is twice as long as the 6-12 hour potential observed mixing period. Other sources of increased fluorescence measurements by the glider may be from resuspended near-bed material in the lower layer, observed between October 29th at 00:00 GMT and the 29th at 06:00 GMT, but aside from

advection there are limited sources and sinks for phytoplankton in the surface layer on short time scales.

3.5 Discussion

While Richardson numbers do not definitively indicate whether mixing or advection was responsible for the transition from stratified to destratified conditions, the net increase in depth averaged temperature, sharp increase in bottom temperatures (Figure 3.8B), rapid decrease in bottom chlorophyll concentrations, near constant surface chlorophyll concentrations (Figure 3.8C), downwelling favorable winds (Figure 3.3) and offshore bottom currents (Figure 3.4D) indicate that stratification likely significantly inhibited vertical mixing and offshore advection was the primary cause of the transition from two-layer stratified conditions to one-layer destratified conditions.

3.6 Conclusions

Hurricane Sandy was a major event that caused extensive storm surge and coastal flooding along the U.S. Mid-Atlantic Bight. Observations from a Teledyne-Webb Slocum glider, RU23, equipped with a Nortek Aquadopp current profiler deployed in rapid-response to an accurate storm track forecast showed a transition from summer, stratified conditions, to winter destratified conditions in approximately 12 hours. Temperature, chlorophyll and current data indicate that this transition occurred 18 hours before the eye made landfall, primarily due to downwelling favorable winds and offshore advection of the bottom Cold Pool. The two-layer cross-shelf flow during the deepening period, T2, between 12:00 GMT on the 28th and 06:00 GMT on the 29th was similar to the seaward side of a

downwelling front, while one-layer flow was consistent with the shoreward side of a downwelling front similar to results discussed in *Lentz* (2001) and *Austin and Lentz* (2002).

Past studies have focused on mixing as the dominant process controlling sea-surface temperature ahead of and beneath storms in the deep ocean [*Price*, 1981], but few studies have detailed the evolution of the thermocline and coastal circulation ahead of and beneath hurricanes, as observations are typically difficult to obtain on continental shelves in extreme conditions. Numerous studies have demonstrated that small changes in upper-ocean heat content and sea-surface temperature can affect hurricane intensity [*Price*, 1981; *Emanuel*, 1999; *Bender and Ginis*, 2000; *Emanuel et al.*, 2004; *Yablonsky and Ginis*, 2008] as the ocean provides a source of heat for atmospheric convection through moist enthalpy flux [*Black et al.*, 2007]. While some forecast models include a fully coupled three-dimensional ocean [*Yablonsky and Ginis*, 2008; *Warner et al.*, 2010], the majority of models parameterize air-sea heat fluxes with static pre-storm satellite sea-surface temperature (SST) and one-dimensional vertical mixing models that neglect advective processes [*Emanuel et al.*, 2004]. [*Price*, 2009] concluded that continental shelves and shallow water regions may significantly impact hurricane intensification, and may have significant impacts immediately before landfall, but conditions such as those seen on the MAB with a summer Cold Pool and temperatures much below the 26°C isotherm, used to define the upper mixed layer, were not addressed in that study. Future sensitivity studies that include realistic representations of the MAB summer and winter conditions, driven by observations

such as those presented in this paper, are necessary to determine the impact of the MAB coastal ocean on storm intensity.

In addition to air-sea interactions, three-dimensional processes have implications for storm-surge models, as the current operational models are primarily two-dimensional [*Jelesnianski et al.*, 1992; *Glahn et al.*, 2009] and do not resolve the impacts of continental shelf stratification on storm surge. Further studies will be needed to assess the impact of three-dimensional processes on storm surge.

Observations of the coastal ocean response to tropical and extra-tropical cyclones have been severely limited, as extreme weather conditions have made sampling difficult. Gliders have become a proven robust sampling platform for extreme weather that can focus on the continental shelf and compliment air-deployed drifters and buoys that primarily focus on the deeper ocean. The addition of a Nortek Aquadopp current profiler onboard a glider provided new insights into the coastal ocean dynamics ahead of and beneath Hurricane Sandy. Further integration of these sensors will allow for real-time data transmission along with more traditional glider data to inform and validate coastal ocean forecast models. Future observational work will include downward looking profilers to more accurately estimate bottom stress and accelerometers to resolve wave motions at glider locations. Continues use of optical sensors is not only critical to resolve environmental properties such as chlorophyll and sediment concentrations, but are also critical for using optical properties as water-mass tracers over short timescales during extreme events.
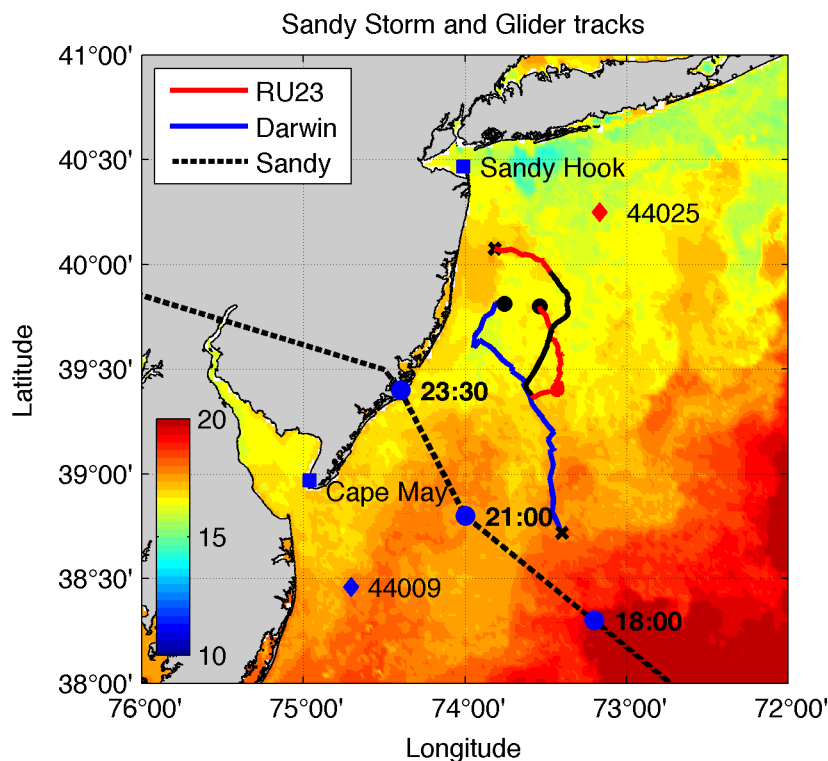
Figure 3.1 A regional map of the Mid-Atlantic Bight overlaid with a pre-storm AVHRR SST 3-day coldest-pixel composite from between 12:00 and 18:00 GMT on October 24th to the 26th, 2012. The National Hurricane Center best track of Sandy (dashed black line) and corresponding time points (blue dots representing the hour and minute of time points on October 29th in GMT). National data buoy center buoys 44025 (red diamond) and 44009 (blue diamond). Total track of glider RU23 (red line) and the storm time period that corresponds with transects in Figure 3.4 (black overlay). RU23 deployment (black x) and recovery location (black circle). Track of glider Darwin (lue line) with the beginning of the cross-shelf transect (black x) and recovery location (black circle).
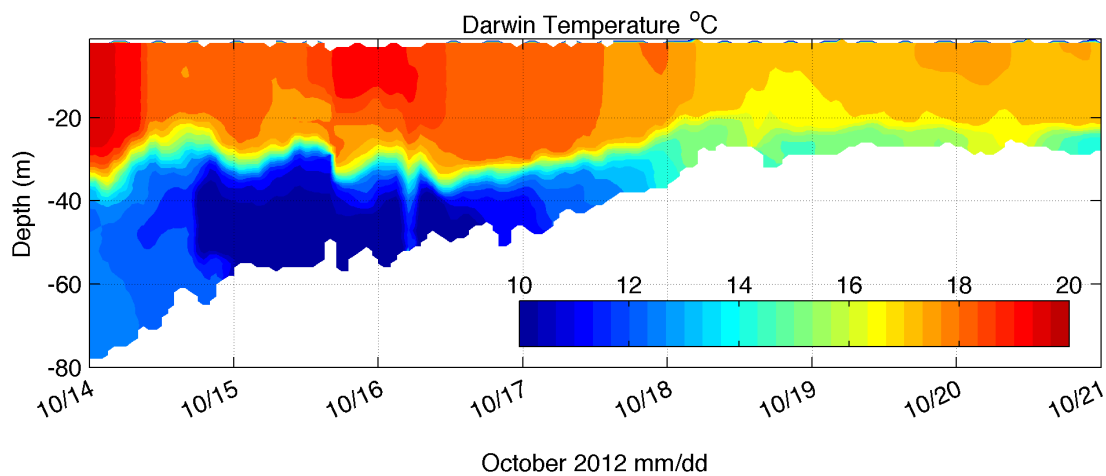
Figure 3.2 A cross-section of temperature from glider Darwin, extending from near the shelf-break at 80 meters depth to the near shore region shallower than 20 meters depth. Darwin's track is plotted in Figure 3.1 and the color bar corresponds to the satellite temperature values in Figure 3.1. Dates along the x-axis are in month/day.

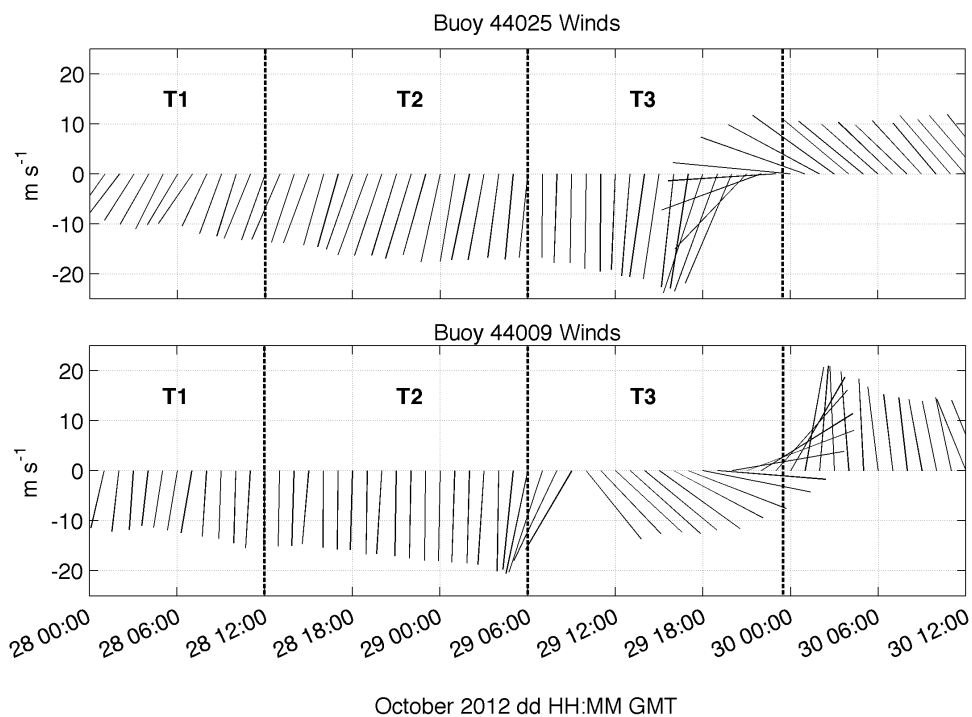**Figure 3.3** Wind speed in meters/second and direction (toward) from NOAA buoys 44025 (top) and 44009 (bottom). Directions are aligned 30° rotated clockwise from north, with up (down) being along-shelf toward the northeast (southwest) and to the right (left) being eastward (westward). Vertical dashed lines separate time periods T1, T2 and T3. The x-axis is time with the format of October 2012 day hour:minute in GMT.
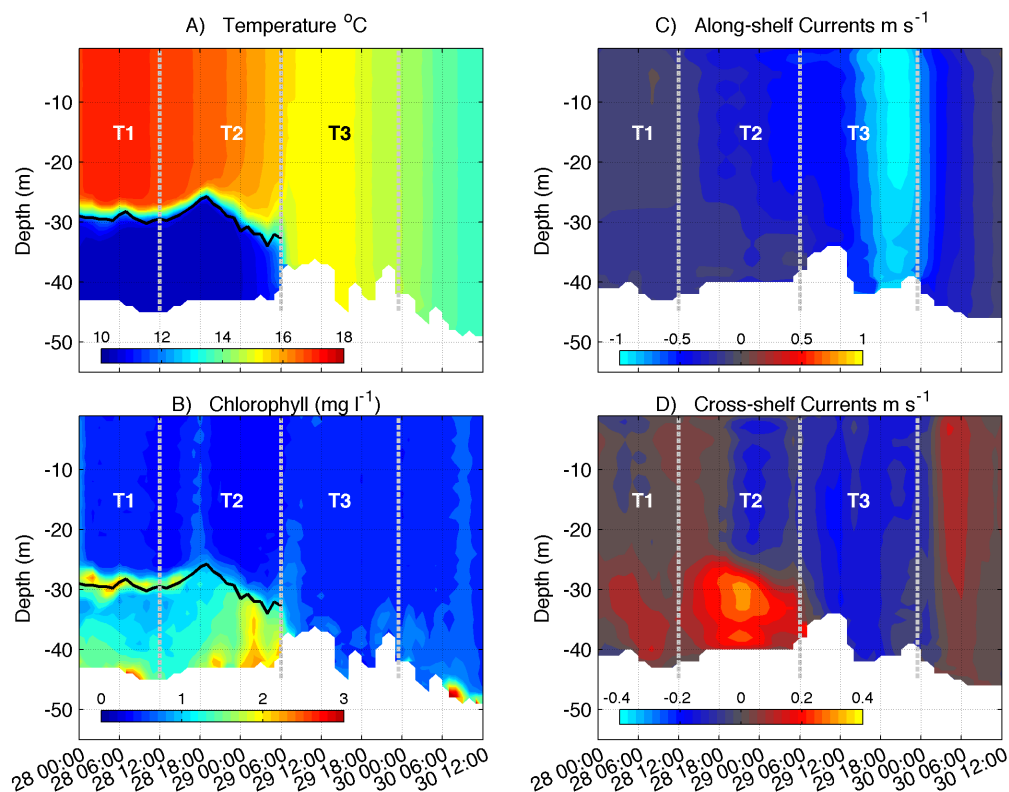
Figure 3.4 RU23 glider data during the storm forcing period on October 28th at 00:00 GMT to the 30th at 12:00 GMT (represented by the black line in Figure 3.1). A) Temperature ^{o}C and B) Chlorophyl (mg/m^3) with a black contour representing the thermocline defined by the largest temperature gradient over 0.25 ^{o}C m^{-1}. C) Along-shelf and D) cross-shelf de-tided currents calculated from the Nortek Aquadopp current profiler. Positive is toward the southwest in the along-shelf direction and offshore in the cross-shelf direction. Note the different color bars for the along and cross- shelf currents. Time formats on the x-axis are as in figure 3.3.
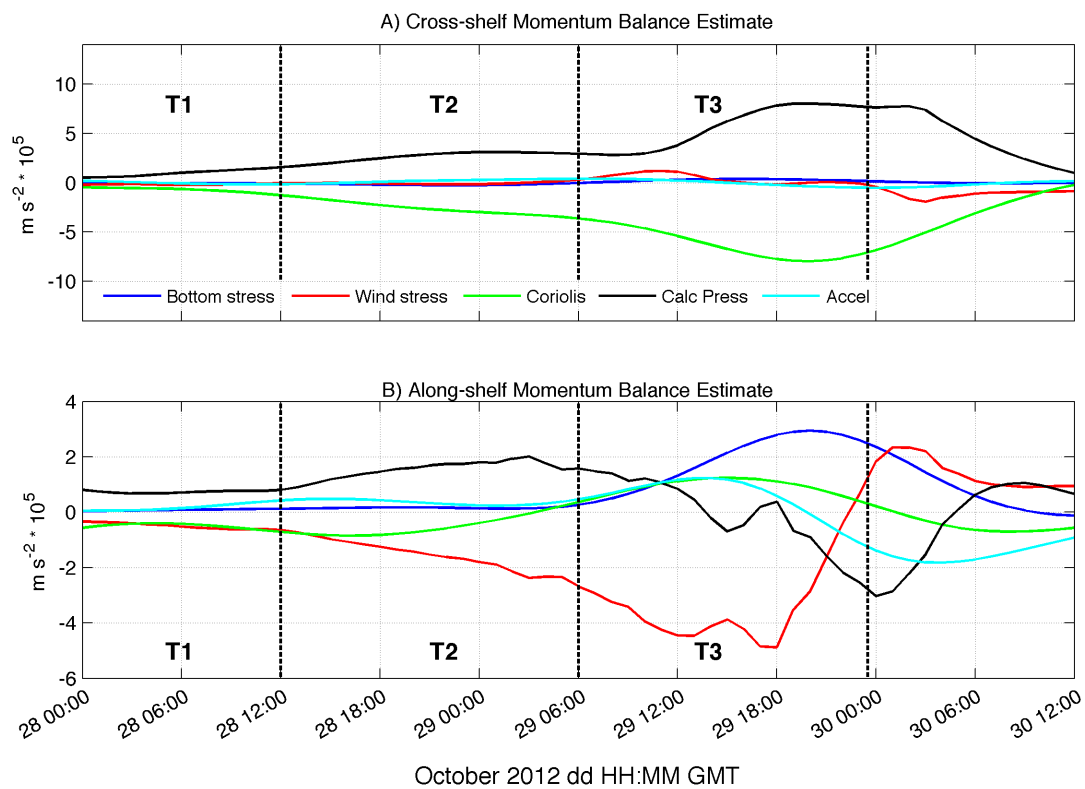
Figure 3.5 Estimates of the A) along- and B) cross- shelf momentum equation terms, (blue) bottom stress, (red) wind stress, (green) Coriolis, (black) calculated pressure gradient and (cyan) acceleration.   Vertical black dashed lines and time formats are as in Figure 3.3.
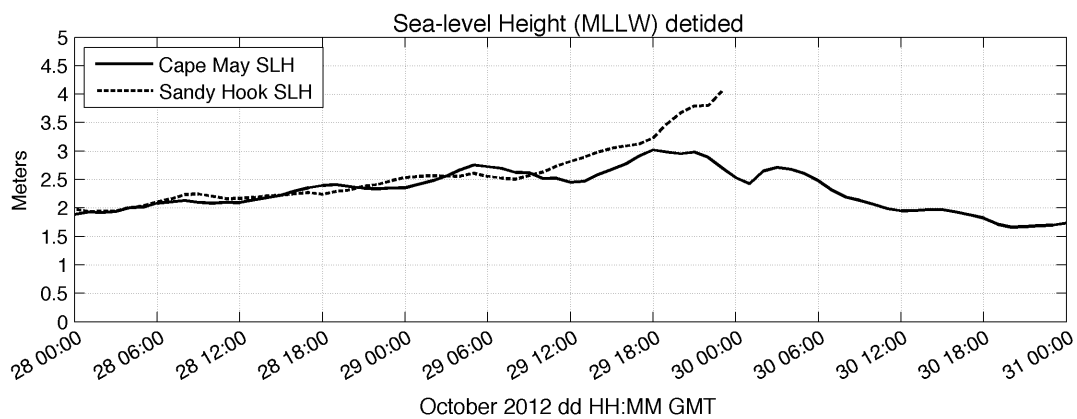
Figure 3.6 Sea-level height relative to mean-lower low water with tides removed using least squares. Records are from (solid line) Cape May New Jersey (Figure 3.1) and Sandy Hook New Jersey (Figure 3.1). The Sandy Hook New Jersey site was destroyed just prior to landfall at 23:30 GMT on October 29th. Time formats on the x-axis are as in Figure 3.3.

Hourly Surface Current Field (5MHz): 2012-Oct-29 00:00
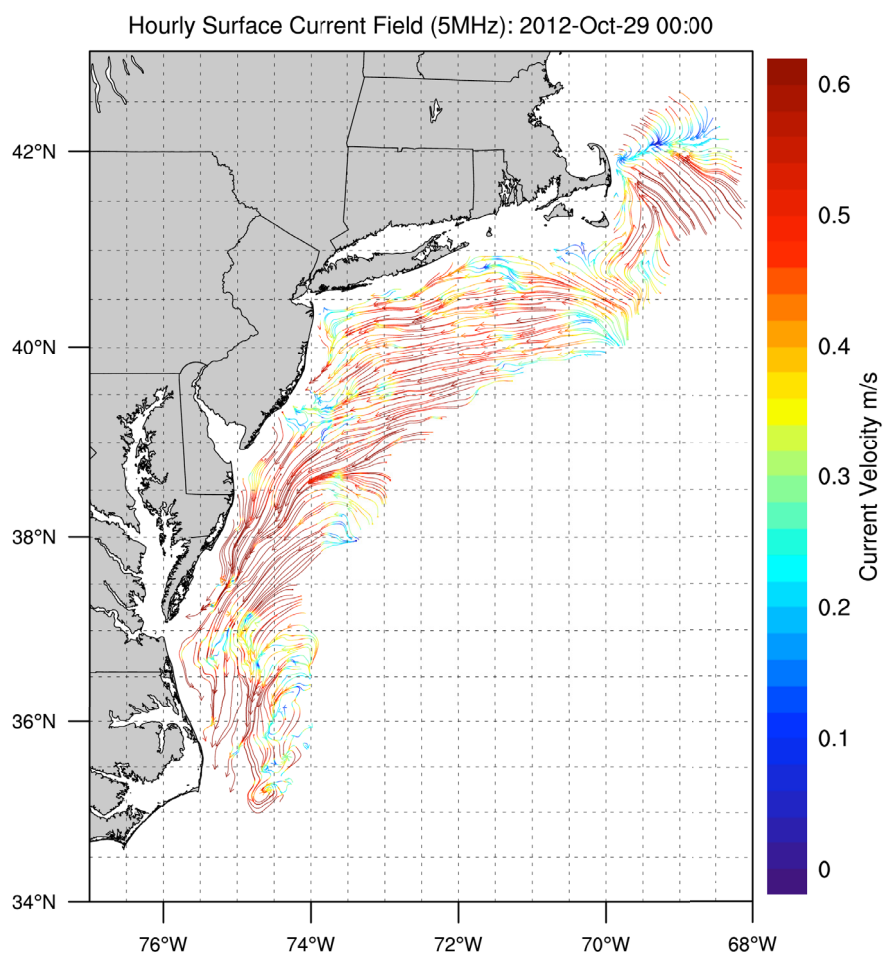
Figure 3.7 A 3-hourly center averaged map of the 5MHz network of High Frequency radar surface currents across the entire Mid-Atlantic region on October 29th at 00:00 GMT.
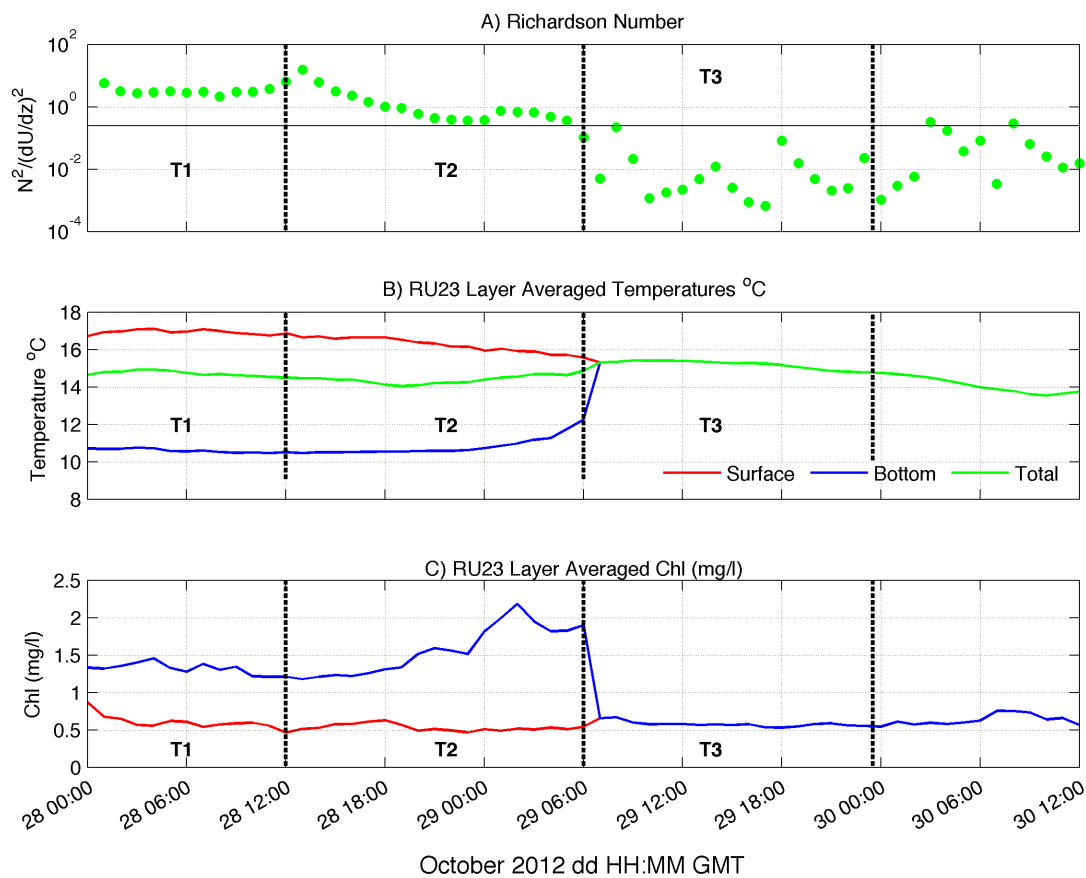
Figure 3.8 Time series of A) the maximum gradient Richardson number calculated for each hourly averaged profile. The y-axis is on a log scale where the horizontal black line represents the critical Richardson number of 0.25. B) Layer averaged temperatures °C and C) layer averaged chlorophyll concentrations (mg l^{-1}) calculated (red) above and (blue) below the thermocline as well as (green) across the full water column depth. Times on the x-axis are as in Figure 3.3.

Chapter 4

Glider observations and modeling of sediment transport in Hurricane Sandy

4.1 Introduction

Storms are important episodic events that redistribute sediment on continental shelves [*Cacchione and Grant*, 1987; *Drake and Cacchione*, 1992; *Sherwood et al.*, 1994; *Ogston et al.*, 2000; *Keen and Glenn*, 2002; *Styles and Glenn*, 2005; *Teague et al.*, 2006; *Warner et al.*, 2008a]. Many of the field programs over the past two decades used benthic landers and tripods equipped with a suite of optical and acoustic sensors at a single location to understand sediment resuspension and transport dynamics [*Trowbridge and Nowell*, 1994; *Agrawal and Pottsmith*, 2000; *Harris et al.*, 2003; *Styles and Glenn*, 2005]. These sensor platforms have provided a wealth of information that have aided in the development of one-dimensional bottom boundary layer models (BBLMs) that take into account combined wave and current interactions [*Grant and Madsen*, 1979, 1986; *Glenn and Grant*, 1987; *Madsen and Wikramanayake*, 1991; *Madsen*, 1994; *Styles and Glenn*, 2000, 2002a; *Warner et al.*, 2008b]. These one-dimensional models generally require input of wave and current data and a significant amount of tuning in order to accurately predict sediment resuspension and transport at a specific location.

In the past decade these one-dimensional BBLMs have been coupled to three-dimensional hydrographic models to understand broader scale erosion and deposition at regional scales [*Blaas et al.*, 2007; *Papanicolaou and Elhakeem*, 2008; *Warner et al.*, 2008b; *Hu et al.*, 2009]. With the development of these regional scale

sediment resuspension and transport studies new technologies are necessary to supplement single point measurements of sediment resuspension and transport on continental shelves. Many of the sensors included on tripods and benthic landers have now been developed for autonomous platforms such as Teledyne-Webb Slocum gliders [*Davis et al.*, 2003; *Schofield et al.*, 2007; *Glenn et al.*, 2008]. A study by *Glenn et al.*, (2008) presented data from two gliders deployed on the New Jersey shelf during storm conditions, one during stratified summer months and the other after the fall transition to well-mixed winter conditions. The stratified summer deployment showed sediment resuspension throughout the bottom layer, restricted by thermal stratification, during a summer hurricane, while the deployment after the fall transition identified full water column sediment resuspension, which followed a Rousian distribution[*McLean*, 1991], where suspended sediment concentration decreased logarithmically with height above the bed. A follow up study [*Miles et al.*, 2013] used two simultaneously deployed gliders during a Nor'Easter in fall of 2009 to identify spatial variability in sediment resuspension and transport.

The present work builds on previous sediment resuspension and transport work by using a combination of modeling and glider observations to identify idealized broad spatial patterns of sediment resuspension, transport and deposition on the New Jersey (NJ) continental shelf during Hurricane Sandy in October of 2012. We use observations from a Teledyne-Webb Slocum glider equipped with acoustic and optical sensors, which provide *in situ* model validation data at mid-shelf before, during and after the storm event

4.2 Methods

4.2.1 Gliders

Teledyne-Webb Slocum gliders have become robust tools for sampling storm

conditions [*Glenn et al.*, 2008; *Ruiz et al.*, 2012; *Miles et al.*, 2013]. These instruments

are mobile sensor platforms that profile through the water column using a

combination of buoyancy and a set pitch angle to move vertically and horizontally in

a sawtooth pattern. Data is logged every two seconds on downcast and upcast with

vertical speeds of ~20 cm/s resulting in high data density relative to traditional

shipboard techniques. A single hour long sampling segment may include

approximately 5 to 10 profiles depending on water column depth. After each

segment is complete the glider surfaces and relays its position and data back to

Rutgers using an Iridium satellite phone in the aft section of the glider. Further

details of Rutgers glider operations can be found in *Schofield et al.*, (2007a) .

The glider used in this study was RU23, a first generation shallow (100 meter

rated) glider equipped with a suite of oceanographic sensors. RU23 included three

science sensors, a Seabird un-pumped conductivity temperature and depth (CTD)

sensor, two Wetlabs triplet sensors and an externally mounted Nortek Aquadopp

current profiler. One Wetlabs triplet was an optical backscatter puck (bb3) that

measured the volume scattering function (VSF) at three wavelengths 470-, 532- and

660 nanometers in the 117° back direction. We converted from the VSF to estimated

backscatter coefficients following *Boss and Pegau* (2001). For our analysis we use

the 660 nanometer channel as it is less impacted by absorption effects than the

shorter wavelength channels (Emmanuel Boss, personal communication). These

instruments respond linearly to increased suspended particulate matter concentrations [*Boss et al.*, 2009], but are also sensitive to variability in particle size, shape and composition; similar sensors were used onboard previous glider observations of storm driven sediment resuspension and transport [*Glenn et al.*, 2008; *Miles et al.*, 2013]. The second Wetlabs triplet was an ecopuck that we used primarily to measure chlorophyll fluorescence.

The Nortek Aquadopp was a three-beam two-megahertz system with a 0.2 meter blanking distance that collected data in ten one-meter bins. The Aquadopp was externally mounted in an upward looking position, with a custom glider head that measured 0 degrees pitch at a nominal glider pitch angle of 26.5 degrees. Data was logged internally and downloaded post-deployment. This instrument served two purposes: the first, detailed in *Chapter 3*, was to estimate realistic water-column velocities following methods developed for lowered acoustic doppler current profilers [*Visbeck*, 2002] and recently adapted to use on glider platforms[*Todd et al.*, 2011a, 2011b]. The second purpose was to provide acoustic backscatter observations coincident with optical measurements. Acoustic return (*Amp*) strength along each beam was converted to echo level (*EL*), with units of decibels (dB) following *Lohrmann*, (2001):

$$EL = Amp \times 0.43 + 20 \log_{10}(R) + 2\alpha_w R + 20R \int \alpha_p \times dr \qquad (4.1)$$

where, R is the range along each beam, α_w is water absorption in db/m, and α_p is particle attenuation in db/m.

Previous studies [*e.g. Lynch et al.*, 1997] have used co-located optical and acoustic backscatter sensors on bottom tripods to assess the relative contribution of

small and large sediment particles. The difference in acoustic and optical response to different size classes is most clearly illustrated in Figure 4 of [*Lynch et al.*, 1997], with an optical backscatter sensor and a 1MHz and 5MHz acoustic backscatter sensor. An Aquadopp is most sensitive to particles with a $k*a$ = 1, where k is the acoustic wave number and a is the particle radius, [*Lohrmann*, 2001; *Thorne and Hanes*, 2002]. For a 2MHz system a k*a value is most sensitive to particles with a 0.25 mm diameter with a reduction in sensitivity raised to the 4th power for particles smaller than a and inversely proportional for particles with a diameter larger than a. Optical backscatter sensors generally respond to the cross-sectional area [*Bunt et al.*, 1999] and have been shown to have large increases in observed optical backscatter for similar concentrations of small versus large particles, thus in the presence of significant concentrations of small suspended particles these sensors are largely unresponsive to additional concentrations of large particles [*Chris Sherwood, personal communication*].

As the glider was deployed over a broad spatial region with varying bottom types, sediment types and optical properties we did not attempt to calibrate either optical or acoustic backscatter sensors using *in situ* sediment, but rather focus on inter-comparison of the suite of sensors to estimate sediment resuspension and transport throughout the deployment.

4.2.2 Additional Observational Assets

We use National Oceanographic and Atmospheric Association (NOAA) buoy 44025 and 44009 data to supplement glider data and validate numerical model results. NOAA buoy 44025 is located at 40.250 N and 73.167 W off of Long Island,

New York and NOAA buoy 44009 is located at 38.461 N and 74.703 W just offshore of Delaware Bay (Figure 4.1). Buoy data included in this study are hourly wind speed and direction collected at a height of four meters, barometric pressure, significant wave height, dominant wave period, wave spectra and mean wave direction from buoy 44025 only.

4.2.3 Hydrodynamic Model

The Regional Ocean Modeling System (ROMS) [*Shchepetkin and McWilliams*, 2005, 2009; *Haidvogel et al.*, 2008] version 3.6, was used to simulate the ocean response to storm forcing. ROMS is a free-surface, sigma coordinate primitive equation model that is widely used for coastal applications. The configuration here is a modified version of the Experimental System for Predicting Shelf and Slope Optics (ESPreSSO) (http://www.myroms.org/espresso/) with 5 kilometer horizontal resolution and 36 vertical levels, which extends from Cape Cod, MA to Cape Hatteras, NC, and near shore to beyond the shelf-break (Figure 4.2). The ESPreSSO domain has been used extensively on the MAB to study a diverse array of physical and biological processes [*Cahill et al.*, 2008; *Haidvogel et al.*, 2008; *Hofmann et al.*, 2008; *Zhang et al.*, 2009a, 2009b; *Wilkin and Hunter*, 2013; *Xu et al.*, 2013].

We used the original assimilative ESPreSSO 4-dimensional variational data assimilations (IS4DVAR) output as an initial condition starting on October 23rd and ran the model forward including boundary conditions from HYCOM-NCODA (http://hycom.org/), tidal boundary conditions from the ADCIRC tidal model (http://adcirc.org/) atmospheric forcing from the National Center for Environmental Prediction (NCEP) North American Mesoscale (NAM)

(http://nomads.ncep.noaa.gov/txt_descriptions/WRF_NMM_doc.shtml) forecast

system. Air-sea heat and momentum fluxes are calculated by the bulk formulae of

[*Fairall and Bradley*, 1996; *Fairall et al.*, 2003] using the model sea surface

temperature, sea level air temperature, pressure, relative humidity, and 10-meter

winds.

For this study we modify the standard ESPreSSO setup by turning on the

sediment features detailed in section 4.2.4 the BBLM detailed in section 4.2.5 and

drive this BBLM with the wave information from NOAAs WAVEWATCH III model

detailed in section **3.6**. While numerous studies have used the Coupled Ocean

Atmosphere Wave Sediment Transport (COAWST) system [*Warner et al.*, 2010;

Olabarrieta et al., 2012] for sediment transport, which includes a coupled wave and

atmospheric model, for simplicity we use the Rutgers ROMS ESPreSSO domain as it

has a robust history of reproducing realistic circulation over our study region

[*Wilkin and Hunter*, 2013] and required minimal adjustment from the standard

setup to run for the purposes of this study.

4.2.4 Sediment Model

We used the Community Sediment Transport Model (CSTM) to simulate sediment

resuspension and transport. A detailed description of the CSTM can be found in

[*Warner et al.*, 2008b]. The CSTM requires input of user-defined sediment size

classes, critical shear stress values, fall velocities, densities and erodibility constants.

We initialized with an idealized spatially uniform single, 15 meter deep, bed layer

with two non-cohesive size classes of 0.1 mm and 0.4 mm to represent fine and

medium grain size sands found in the glider sample region (Figure 4.1B). According

to a map generated from data collected by the usSEABED project [*Goff et al.*, 2008]

on October 29th, 2012 during peak storm conditions the glider was sampling over a

region with approximately 0.4 mm mean grain sizes. Additionally a recent

publication [*Trembanis et al.*, 2013] collected grab samples on the southern region,

near buoy 44009 and identified mean grain sizes of approximately 0.3 mm prior to

Sandy impacting the region. Based on the 0.1 mm and 0.4 mm diameters and 2650

kg m^{-3} densities we use settling velocities and critical shear stresses of 5.7 mm s^{-1}

and 0.14 N m^{-2}, respectively for the 0.1 mm sediment and 52 mm s^{-1} and 0.23 N m^{-2}

for the 0.4 mm sediment and erodibility constants of 5E-4 kg m^{-2} s^{-1} for both

sediment types. This uniform bed setup is used to only generally represent sediment

resuspension and transport on the continental shelf, and is primarily used for

simplification of data interpretation and comparison of large and small grain size

particles with glider data. This setup will not address the potential impact of

realistic sediment distributions and bed armoring on sediment resuspension. For

more detailed analysis we recommend using a broader array of sediment types,

higher spatial resolution model grids and coupled ocean-atmosphere-wave model

routines.

At each time step the model uses sediment bed properties to calculate bed

roughness at each grid point and passes this information to the bottom boundary

layer model to calculate bottom stress, τ_{sf}, from combined waves and currents. If

critical shear stresses, τ_{ce}, are exceeded sediment is resuspended into the water-

column and transported as a tracer similar to temperature and salinity, but with an

additional source and sink term, based on the erosional source and settling velocity

respectively. From *Warner et al.*, (2008b):

$$C_{source,m} = \frac{\partial w_{s,m} C_m}{\partial s} + E_{s,m} \qquad (4.2)$$

where *s* is the vertical coordinate for the advection diffusion equation in ROMS w_s is

the vertical settling velocity prescribed by the user for each size class m, C is

sediment concentration and E_s is the erosion source, which follows[*Ariathurai and*

Arulanandan, 1978]:

$$E_{s,m} = E_{0,m}(1 - \phi) \frac{\tau_{sf} - \tau_{ce,m}}{\tau_{ce,m}} \qquad \tau_{sf} > \tau_{ce,m} \qquad (4.3)$$

where again, s is the vertical coordinate in ROMS, E_s is the surface erosion mass flux,

E_0 is a bed erodibility constant, ϕ is bed porosity of the uppermost bed layer and τ_{sf}

and τ_{ce} are defined above. For the purposes of this study we only consider

suspended load transport for direct comparison with glider observed suspended

load transport, though for realistic studies of sediment transport bedload transport

must be considered. Bedload transport routines are also available in ROMS [*Meyer-*

Peter and Müller, 1948; *Soulsby and Damgaard*, 2005].

4.2.5 Bottom Boundary Layer Model

The standard ESPreSSO setup uses a quadratic drag law with a drag coefficient

expression to represent bottom stress. For sediment resuspension and transport a

more detailed calculation of bottom stress is needed as realistically, large gradients

in velocity and sediment concentration occur near the bed. For this study we use the

ssw_bbl model, which follows *Madsen* (1994) for combined waves and currents and

the moveable bed routines from *Wiberg and Harris*, (1994) and *Harris and Wiberg*

(2002). The ssw_bbl routine used in this study is covered in detail in *Warner et al.*, (2008b). Parameters required for the ssw_bbl model include sediment characteristics described in the previous section to determine bed roughness, near-bottom reference velocities, u and v taken as the velocity in the lowest model grid, wave orbital velocities u_b, wave period T and wave direction θ.

4.2.6 Wave Model

The wave parameters used for this study are derived from the third generation NOAA WAVEWATCH III (WWIII) (http://polar.ncep.noaa.gov/waves/index2.shtml) operational wave model. We specifically use data from the hindcast reanalysis version 2.22, with 3-hourly output. We use two WWIII datasets for this study, a 4-degree minute and 10-degree minute resolutions that cover the study region. The 4-minute resolution data does not cover the entire ESPreSSO domain but provides higher resolution in near shore shallow water regions. Both the 4- and 10- minute resolution data are interpolated to the standard ESPreSSO grid with a nominal 5km horizontal resolution. While this may not be an ideal methodology for detailed analysis of coastal change or long-term studies on the continental shelf, interpolation of these readily available products were sufficient for a first order comparison of glider optical data to modeled suspended sediment at the mid-shelf. WWIII model hindcasts also do not include the full wave spectra as the operational and forward run products. To calculate bottom orbital velocities from WWIII data without spectral information we use linear wave theory and follow the method of *Wiberg and Sherwood* (2008) using an assumed Joint North Sea Wave Project

(JONSWAP) spectrum. Matlab codes for this calculation are included in the reference and validation of the calculated product of both buoys is presented in section 4.3.3.

4.3 Results

4.3.1 Storm Conditions

On October 28th, when winds and waves began to steadily increase on the MAB (Figure 4.3) the center of Hurricane Sandy was located nearly due east of the Georgia and South Carolina. On October 29th the storm began a left hand turn toward the New Jersey coastline and made landfall near Brigantine, New Jersey at 23:30 GMT (Figure 4.1A) [*Blake et al.*, 2013]. Buoy 44025 and 44009 were located to the north and south, respectively, of the storm track as it crossed the shelf (Figure 4.1A). Minimum sea-level pressure at 44025 and 44009 was below 960 at both locations, and maximum wind speeds peaked over 20 m s^{-1} (Figure 4.3). Winds were initially downwelling favorable from the northwest at 44025 and north at 44009. Winds shifted counterclockwise to be more northeasterly at 44009 on October 29th as the storm center crossed the shelf. Winds at 44025 maintained a northwesterly direction until just prior to landfall when they shifted clockwise to be from the southwest as the eye passed between the two stations. Significant wave heights first peaked on the southern MAB at 44009 near 7 meters approximately 12 hours before they peaked at 44025 near 10 meters. Dominant wave periods at both buoys reached 15 seconds near landfall. Wave periods dropped immediately following eye passage at 44009, likely due to the rapid shift in wind direction. While no wave direction data was available at 44009, mean wave direction at 44025 was generally in agreement with wind direction.

4.3.2 Glider Deployment

Glider RU23 was deployed on October 25th approximately 15 km off of northern

New Jersey, on the southern flank of the Hudson Shelf Valley (Figure 4.1A). RU23

progressed southeastward in an effort to exit a coastal shipping lane prior to storm

conditions. During the initial storm forcing period from October 28th 00:00 GMT to

the 29th at 06:00 GMT the water-column observed by the glider was highly

thermally stratified with surface temperatures of near 18 ^{o}C and bottom

temperatures as low as 10 ^{o}C separated by a sharp thermocline (Figure 4.4A).

During the stratified phase currents measured by the Nortek Aquadopp showed

two-layer cross-shelf flow consistent with downwelling circulation on the shelf

(Figure 4.4B-C), with offshore flow near the bottom and onshore flow near the

surface. On October 29th at 06:00 GMT the system transitioned from two- to one-

layer with a uniform water column temperature of ~15 ^{o}C and strong along-shore

flow toward the southwest. As glider horizontal speeds are on the order of 0.2 to 0.3

m s^{-1} the glider was rapidly advected along-shore with the mean current until after

the eye passed on October 29th at 23:30 GMT. A further detailed analysis of the

evolution of the glider temperature and current data is presented in *Chapter 2*.

4.3.3 Model Validation

To validate the meteorological and wave forcing parameters we calculated

correlation coefficients, root-mean-square-error and R^2 from a simple linear

regression between modeled and observed winds, sea level pressure, wave height

and calculated bottom orbital velocities at buoy 44025 and 44009. We focused the

comparison on the storm forcing period between October 28th at 00:00 GMT and the

31st at 00:00 GMT so as not to bias the validation to fair-weather conditions.

Quantitative results are detailed in captions for Figures 4.5-4.6.

Qualitatively, the NAM hindcast wind speed and pressure (Figure 4.5) were in good agreement with observations at buoy 44025 with observed and modeled peak wind speeds over 25 m s^{-1} (Figure 4.5A) and minimum sea level pressures near 960 millibars (Figure 4.5C). On the southern side of the storm at buoy 44009 the wind speed was over predicted (Figure 4.5A-4.5B), with a deep trough in wind speed on October 29th at 12:00 GMT not well represented by the model. Additionally modeled pressure at buoy 44009 was approximately 10 millibars higher than observed at 970 and 960 millibars respectively on October 29th at 21:00 GMT (Figure 4.5C-D). Potential errors could be related to the exact position of the storm track in the model. As this paper is focused on direct comparison between the glider and modeled sediment resuspension the agreement on the northern side of the storm, where the glider was also, at buoy 44025 is sufficient for our purposes.

WWIII modeled wave heights (Figure 4.6A-B) were under-predicted at both locations ahead of the storm, particularly at 44009, with peak observed wave heights occurring nearly 12 hours ahead of peak modeled wave heights. Wave heights between October 29th at 12:00 GMT and October 31st at 00:00 GMT were well represented at both locations and peak modeled and observed wave heights occurred at approximately the same time at buoy 44025. Modeled bottom orbital velocities at 44025 were similarly under predicted but generally in good agreement with the observations (Figure 4.6C-D). Differences between modeled and observed waves are likely due to the lack of spectral information included with the archived

WWIII model data and coarse resolution. These properties would likely be improved by use of operational WWIII products with full spectral information or by using a modeling system such as COAWST, which includes three-way coupling between ROMS, the simulating waves nearshore (SWAN) model, and the weather research forecasting (WRF) model [*Warner et al.*, 2010]. Comparisons between the model and observations were sufficient for analysis of concurrent glider and model data north of the eye.

In order to assess modeled ESPreSSO currents we compared depth-averaged values along the glider track to depth- and time- averaged glider currents calculated using dead-reckoning [*Davis et al.*, 2003]. ESPreSSO currents were extracted hourly from the nearest grid point to each hourly glider surfacing. Both glider and ESPreSSO currents were rotated clockwise 30 degrees from true north to align approximately along-shore and cross-shore at the glider location. ESPreSSO currents were in good agreement with the observed dead reckoned glider currents for the majority of the deployment (Figure 4.7A-B). R-squared values were 0.61 and 0.91 for cross- and along- shore currents respectively. Cross-shore currents were generally well represented, though predicted velocities were slightly slower during the main forcing period from October 29th to at 00:00 GMT to the 30th at 06:00 GMT. Both modeled and observed along-shore velocities reached peak values near 1 m s^{-1} at landfall, with modeled peak current speeds leading glider current speeds by approximately half an hour.

4.3.4 Glider and modeled sediment resuspension and transport

Typically validation of regional sediment resuspension and transport is done using post-storm surveys or using single point locations but little *in situ* validation over broad spatial regions and throughout the full water column has previously been possible from a single set of profiling sensors. As our glider, RU23, was equipped with optical and acoustic sensors we compare along-track sediment resuspension and transport between the modeled and glider.

Cross-sections of modeled suspended 0.4 mm and 0.1 mm sediment concentration along the glider track (Figure 4.8A-B) are compared with Aquadopp acoustic backscatter and bb3 optical backscatter (Figure 4.8C-D). Modeled cross-sections of sediment resuspension along the glider track show 0.4 mm and 0.1 mm sediment resuspension initiate in response to storm forcing after October 28th at 12:00 GMT, with concentrations limited to within a few meters of the bed. Full water-column resuspension is evident 24 hours later, on the 29th after 12:00 GMT, with large concentrations evident in the lower 10-15 meters for 0.4 mm sediment, and throughout the entire water column to the surface for 0.1 mm sediment. Peak values for both grain sizes occur on the 29th at 19:00 GMT, a few hours prior to landfall, following peak modeled and observed wave heights and orbital velocities at buoy 44009 but prior to peak values at 44025 (Figure 4.5A-B). This is likely the timing of peak wave heights and orbital velocities at the glider location, which is approximately mid-way between the two buoys. Larger 0.4 mm particles fall out of suspension rapidly after the eye made landfall on October 29th at 23:30 GMT, while smaller particles had persistent elevated concentrations throughout the water

column for 18 hours following landfall. Acoustic backscatter (Figure 4.8C) was significantly different from modeled values in two distinct ways. First, during early stages of the deployment, between October 28th at 06:00 GMT and October 29th at 00:00 GMT there is a clear acoustic backscatter signal that fills the lower stratified (Figure 4.4A) region. Wave heights and orbital velocities were building during this period (Figure 4.6A and 4.6B) but were relatively weak compared to peak values. This feature was also present in optical backscatter values (Figure 4.8D), which indicates that the Aquadopp was likely responding to smaller fine grained sediment in the absence of a significant signal from larger grain sediments near the target 0.25 mm grain size. Cross-sections of chlorophyll concentration (Figure 4.8E) derived from the fluorometer also suggest finer particles or biological material in this lower layer prior to transition from stratified to destratified conditions. The second deviation from the modeled suspended sediment is a persistent near surface acoustic backscatter signal, which peaks during peak wave and wind conditions on October 29th at 19:00 GMT. This signal is likely due to bubble entrainment in the surface boundary layer. In the lower portion of the water column acoustic backscatter qualitatively agrees with modeled 0.4mm suspended sediment, with peak acoustic backscatter near 75 dB just prior to landfall coincident with modeled peak concentrations. After the storm passed between October 30th at 00:00 GMT and the 31st at 00:00 GMT the persistent full water column acoustic backscatter near 55 dB is again likely due to fine particles that remained resuspended after coarse sand fell out of suspension. Cross-sections of optical backscatter at 660 nm (Figure 4.8D) qualitatively agrees with Concentrations of 0.1 mm sediment, which were

elevated to the sea-surface at nearly the same time as observed optical backscatter just prior to October 29th at 18:00 GMT, the peak in 0.1 mm concentrations and optical backscatter occurred in the model and observations similar to the acoustic and modeled 0.4 mm sand just prior to landfall at 19:00 GMT on October 29th. The optical signal remained high throughout the water column until October 30th near 18:00 GMT, persisting longer than modeled 0.1 mm sand. This suggests that there were likely smaller particles present than those modeled, which remained in suspension well after the storm passed. Profiles extracted from each modeled, acoustic and optical cross-section (Figure 4.9) provide a more detailed comparison of sediment resuspension at three time periods, prior to the storm on October 28th at 06:00 GMT, just prior to landfall on October 29th at 21:00 GMT and 18 hours after the storm on October 30th at 18:00 GMT. Shallow slopes were evident in modeled 0.1 mm and 0.4 mm grain sizes as well as acoustic and optical measurements pre-storm, consistent with limited suspended sediment, though there were two features of the optical and acoustic profiles of note. The optics did not have a linear slope on a log-log scale. The sub-thermocline signal is likely related to organic material, detritus, chlorophyll or other fine particulate matter rather than the larger cohesive sediment found on the bottom and was restricted by stratification at 20 meters above the bed. Acoustics (Figure 4.9G) showed a positive slope above the thermocline likely due to bubbles as discussed above. During peak storm conditions modeled and observed profiles were more vertical consistent with large concentrations of suspended sediment. Above 20 meters off the bed acoustics continued to show a positive slope likely due to bubbles and breaking waves (Figure

4.9H). Post-storm profiles were shallower than peak-storm but did not entirely

return to pre-storm conditions consistent with particles continuing to fall out of

suspension.

Depth integrated transport was calculated for modeled sediment

concentrations and observed acoustic and optical backscatter. Acoustic backscatter

responds logarithmically to increased observed concentration [*Lohrmann*, 2001] so

values were raised to the power of 10 and then normalized by dividing by the

maximum observed value. Additionally, acoustic backscatter shallower than 10

meters were neglected from the depth integration to reduce the impact of bubble

entrainment on relative transport estimates. The timing and direction of peak

transport (Figure 4.10) was consistent between modeled and observed transports,

with maximum values in the along-shelf direction on October 29th at 19:00 GMT.

Inconsistency between the modeled and observed cross-shelf currents (Figure 4.7)

during the peak resuspension event is responsible for the limited modeled onshore

transport relative to the observations on the 29th at 19:00 GMT. The model and

observations both captured the offshore cross-shelf transport immediately

following landfall on October 30th at 3:00 GMT.

4.3.5 Regional sediment resuspension and transport

Spatial maps (Figure 4.11) of the modeled storm conditions over the final 12 hours

prior to landfall show snapshots of NAM winds (Figure 4.11A-C) and WWIII waves

(Figure 4.11D-F) on October 29th at 12:00 GMT, 18:00 GMT and October 30th at

00:00 GMT. Winds were initially downwelling favorable and alongshore toward the

southwest on the NJ shelf. WWIII Modeled wave heights were between 9 and 10

meters offshore and decreased with proximity to land. As the storm approached the coast winds shifted to a more onshore direction on the northern portion of the NJ shelf and offshore in the southern portion. Additionally, waves were near 10 meters at the coastline on the northern NJ shelf, and decreased significantly to between 4 and 5 meters on the southern NJ shelf as winds shifted toward the offshore direction.

As bottom orbital velocities and ambient currents are primarily responsible for sediment resuspension and transport, respectively, we present maps of the ROMS Depth-averaged currents with tides retained (Figure 4.12A-C) and WWIII bottom orbital velocities (Figure 4.12D-F) on October 29th at 12:00 GMT, 18:00 GMT and October 30th at 00:00 GMT. Early on October 29th currents were highest south of the Hudson Shelf Valley and nearly uniform across the entire shelf except for a region of weak currents outside of Delaware Bay. As the storm crossed the shelf velocities were elevated to near 1 m s^{-1} across the entire domain. Current speeds were quickly reduced as the storm made landfall, likely due to the shift from along-shore winds to the southwest to weaker along-shore winds to the northeast (Figure 4.13A-C). Bottom orbital velocities throughout the storm forcing duration were highest near shore south of the Hudson Shelf Valley with largest values, over 1.5 m s^{-1} near the glider deployment location on the northern side of the storm track.

Snapshots of depth-integrated suspended sediment concentration for the 0.4 mm (Figure 4.13A-C) and 0.1 mm (Figure 4.13D-F) are additionally mapped for the same time periods as in Figure 4.11 and Figure 4.12 to show regional model estimates of sediment resuspension throughout the storm. On October 29th at 12:00

GMT depth integrated concentrations on the NJ continental shelf south of the Hudson Shelf Valley were near 1.2 kg/m^2 and 10 kg/m^2 for 0.4 mm and 0.1 mm respectively, with highest values in the near shore region for 0.4mm and highest values on the central NJ shelf further offshore for the 0.1 mm sediment. On the 29th at 18:00 GMT 0.4mm sand is resuspended along the entire inner shelf south of the Hudson Shelf Valley, while 0.1 mm sand is mobilized over the entire inner, middle and outer shelf regions. As the storm made landfall near October 30th at 00:00 GMT Figure 4.13C and 4.13F show the 0.4 mm sand is resuspended coincident with peak orbital velocities (Figure 4.12F) and 0.1 mm sand is at a maximum across the entire northern portion of the shelf. Values for both 0.4 mm and 0.1 mm on the southern portion of the NJ shelf dropped significantly between October 29th at 18:00 GMT and October 30th at 00:00 GMT. This reduction is likely a result of the reduction in wave heights and orbital velocities associated with a reversal of wind direction as Sandy crossed the shelf.

Bed thickness change from the initialization to the end of the model run on October 31st at 08:00 GMT (Figure 4.14) shows bed erosion of over 2 cm south of the Hudson Shelf Valley on the northern portion of the NJ shelf. This region is north of the storm track, which had highest waves, orbital velocities, and winds. Deposition of near 2 cm occurred toward the southwest in the direction of along-shelf transport (Figure 4.12A-D).

4.4 Discussion

Previous studies have highlighted along-shore transport as the dominant feature of storm driven sediment transport on continental shelves [*Keen and Glenn*, 1995;

Ogston and Sternberg, 1999; *Styles and Glenn*, 2005; *Miles et al.*, 2013], primarily during winter Nor'easters in the Mid-Atlantic. The typical offshore track of these Nor'easters generally leads to along-shelf wind stress toward the southwest and waves that increase across the entire NJ shelf [*Keim et al.*, 2004]. While Sandy initially had downwelling favorable along-shelf winds (Figure 4.11 A-B), the unique cross-shelf track of the storm [*Hall and Sobel*, 2013] lead to a rotation to offshore winds on the southern portion of the NJ shelf in the 6 hours before landfall. This shift on the southern NJ shelf reduced wave heights (Figure 4.3D and Figure 4.11F), quickly reduced wave periods (Figure 4.3E) and ultimately reduced bottom orbital velocities (Figure 4.6C and Figure 4.11F), which reduced bottom stress and allowed sediment that was continuing to be transported southwestward to fall out of suspension on the southern portion of the domain.

The modeled change in bed thickness of over + and - 2 cm on the northern and southern NJ shelf, respectively, should be approached with caution as the idealized model setup did not account for processes such as bed armoring [*Wiberg et al.*, 1994], which may have reduced available fine grained sediment for resuspension, or bedload transport, which has been shown to be orders of magnitude larger than suspended sediment transport on the continental shelf [*Styles and Glenn*, 2005]. Regardless, the *in situ* observations from acoustic and optical sensors mounted on Slocum glider, RU23, support model results and suggest that a significant portion of the bed was likely eroded from the northern NJ shelf north of the storm track and deposited along the southern portion of the shelf. This modeled erosion and deposition pattern is likely rare on the New Jersey shelf as the

estimated return rate, defined as the occurrence of a sandy-like track with a category 1 or greater under constant climate conditions, is 714 years with a 95% confidence range of 435 to 1429 years [*Hall and Sobel*, 2013].

Autonomous underwater vehicle and ship-based surveys showed partial recovery of the bed near buoy 44009 five weeks after Hurricane Sandy made landfall [*Trembanis et al.*, 2013]. While this suggests that preservation of Sandy's sedimentary signature in the bed is not likely in the active near shore region, the observed deposition toward the shelf break on the southern portion of the domain may be present as reworking in deeper waters is driven by more episodic wave processes [*Wiberg*, 2000].

4.5. Summary and Conclusions

In this study we successfully deployed a Teledyne-Webb Slocum glider in rapid response ahead of Hurricane Sandy on the New Jersey Shelf. This mobile profiling sensor platform proved invaluable in providing *in situ* sediment resuspension and transport model validation, as well as simultaneous validation of currents in the hydrodynamic models. Modeled resuspension and transport showed erosion on the northern portion of the Hudson Shelf Valley, north of the storm track where waves and currents were highest and deposition on the southern NJ shelf just north of Delaware Bay. While glider technologies will not replace high-resolution near bed measurements from moored and bottom mounted sensors they have proven invaluable for providing broader regional validation of three-dimensional models. To the authors knowledge this study provided the first ever assessment of suspended material in a major storm using acoustic sensors on a glider platform.

Future advances that may improve sediment concentration estimates from glider

platforms include downward facing acoustic sensors, which will reduce the impact

of bubble entrainment near the surface, provide data near the bed where

concentrations are highest and allow for detailed estimates of bottom-stress *in situ*
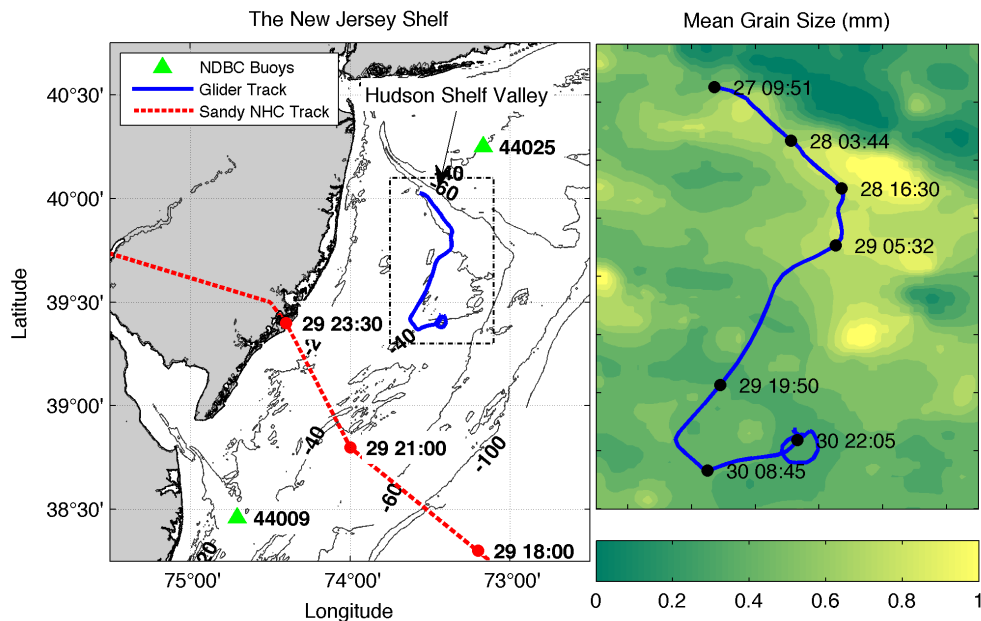
over a large spatial area.

Figure 4.1 Map of the A) New Jersey shelf, with locations of buoys (green diamonds) 44025 and 44009, (blue line) RU23 glider sampling track, the (red dashed line) Hurricane Sandy track from the National Hurricane Center (NHC) with associated time points. A B) map of mean bed grain sizes over the area defined by the dashed box in Figure 4.1A in millimeters compiled from the usSEABED project, with a (blue line) track of the glider consistent with Figure 4.1A overlaied with times in the format of day hour:minute on October 27th through October 30th 2012.
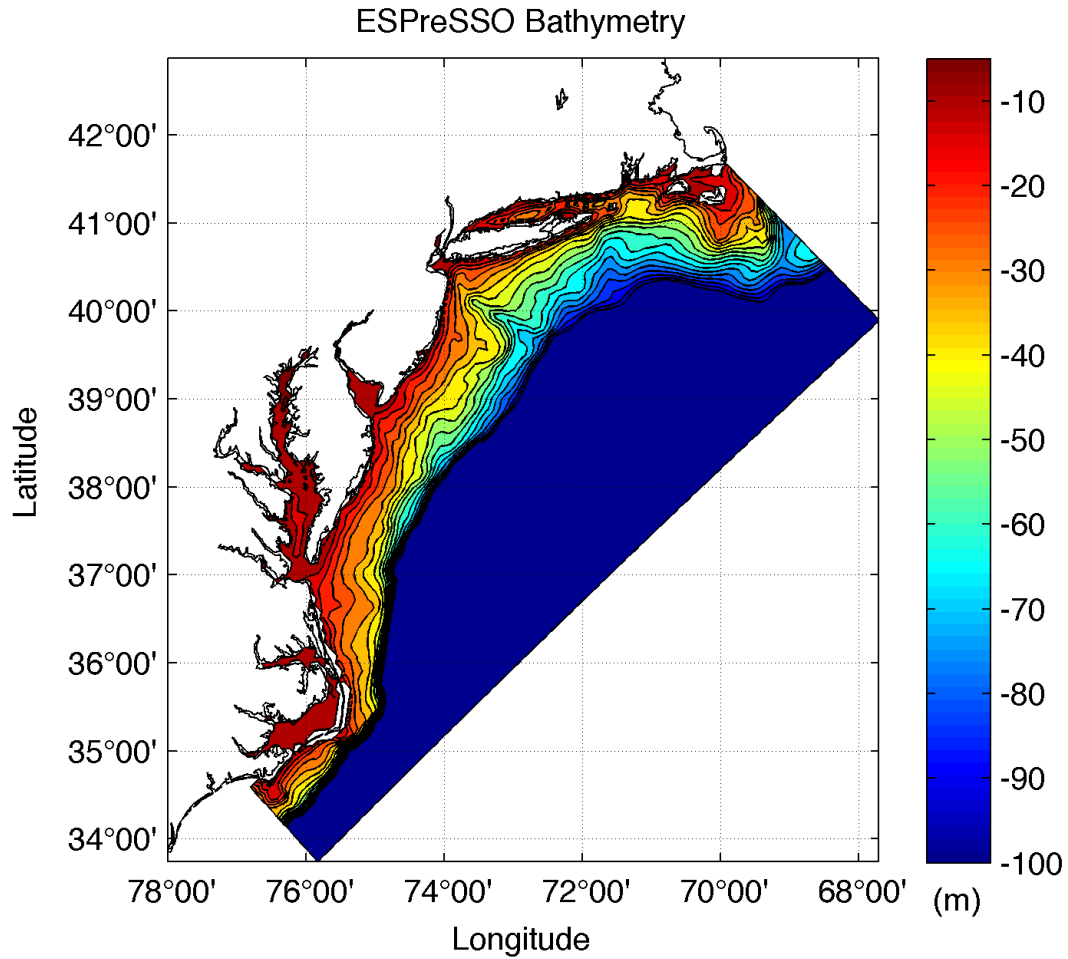
Figure 4.2 A map of bathymetry for the ESPreSSO model domain with contours every 10 meters and the maximum plotted contour of 100 meters depth. Depths go beyond 100 meters off the shelf in the model domain.
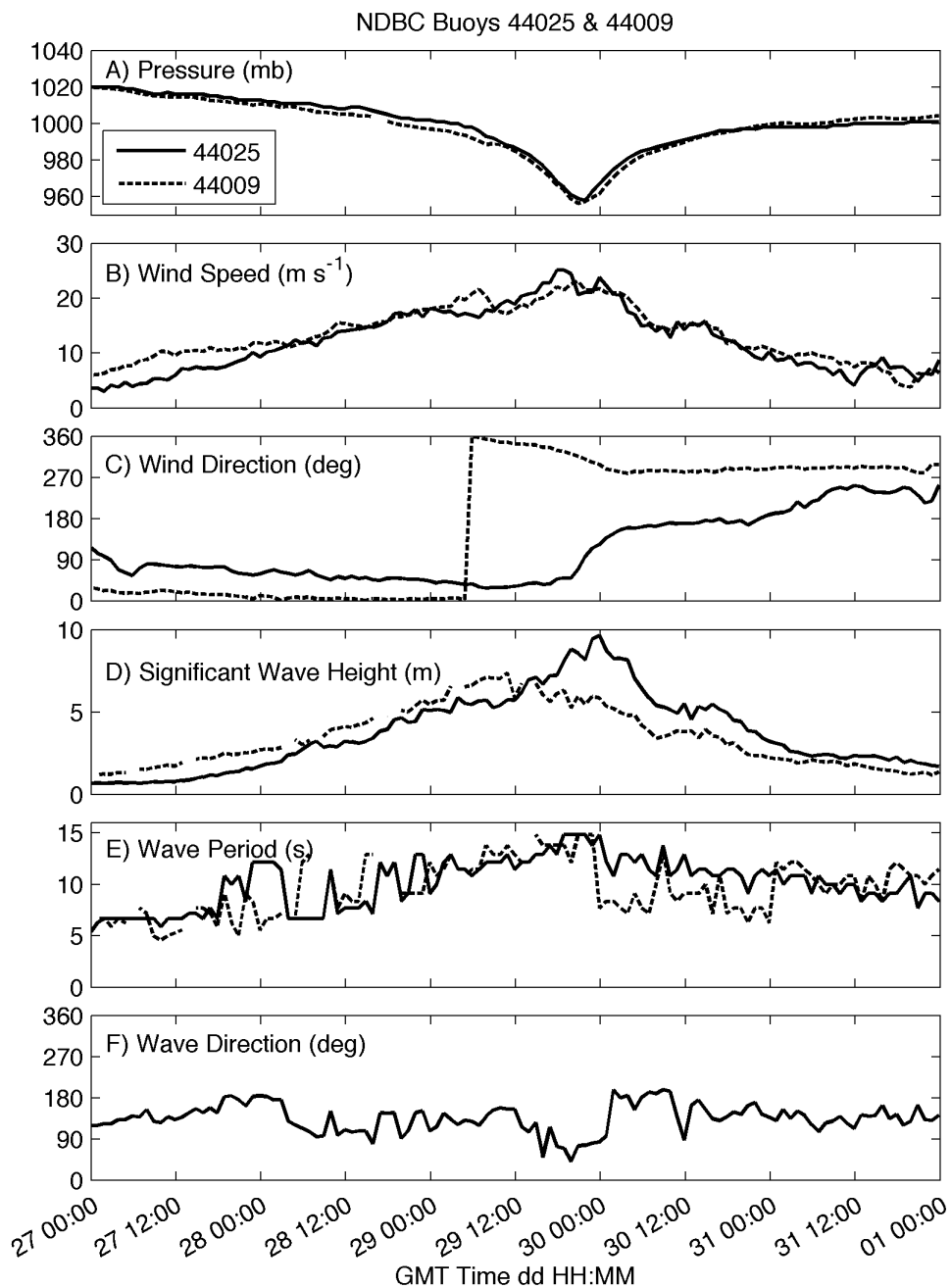
Figure 4.3 Buoy (solid line) 44025 and (dashed line) 44009 A) Pressure, B) wind speed, C) wind direction from north, D) significant wave height, E) wave period, and F) wave direction from north at buoy 44025 only. The x-axis is in days hour:minute for October 2012.
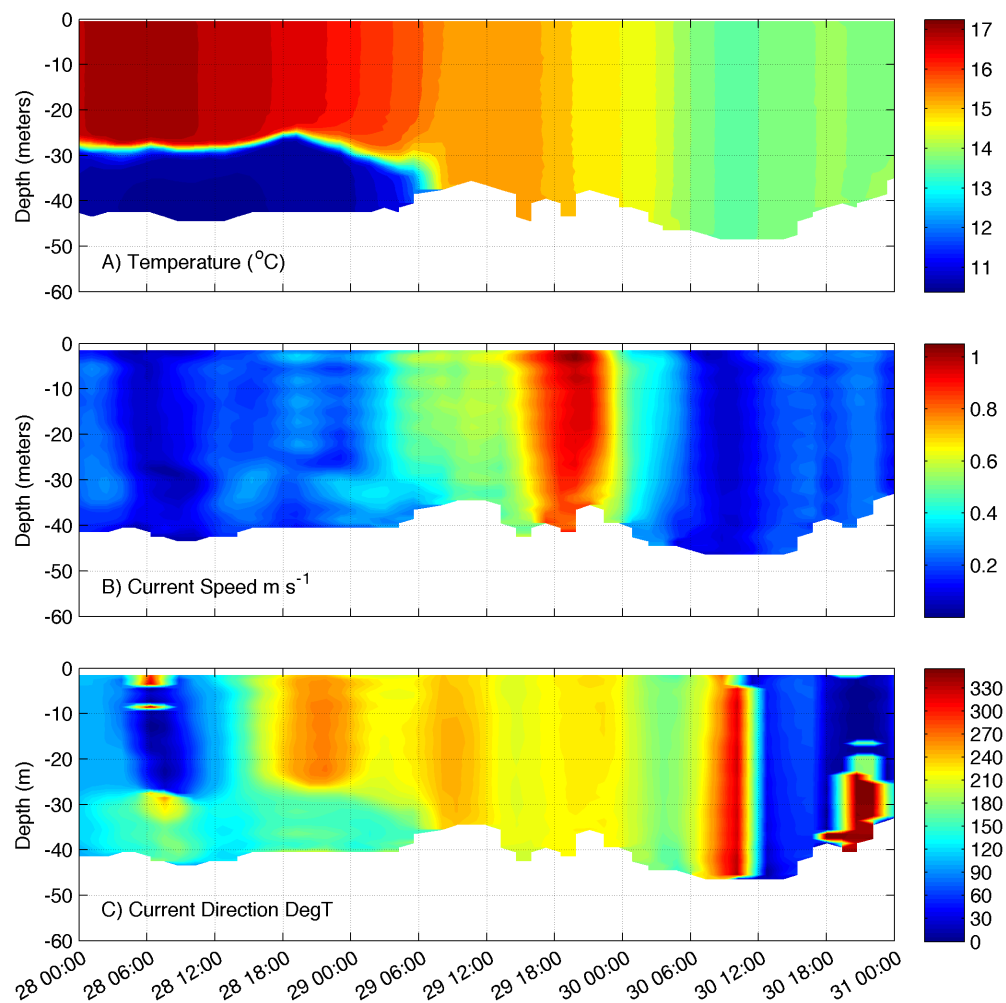
Figure 4.4 Cross-sections along the glider track (Figure 4.1) of A) temperature, B) current speed and C) current direction toward in degrees with north as 0°. Times on the x-axis are as in Figure 4.3.
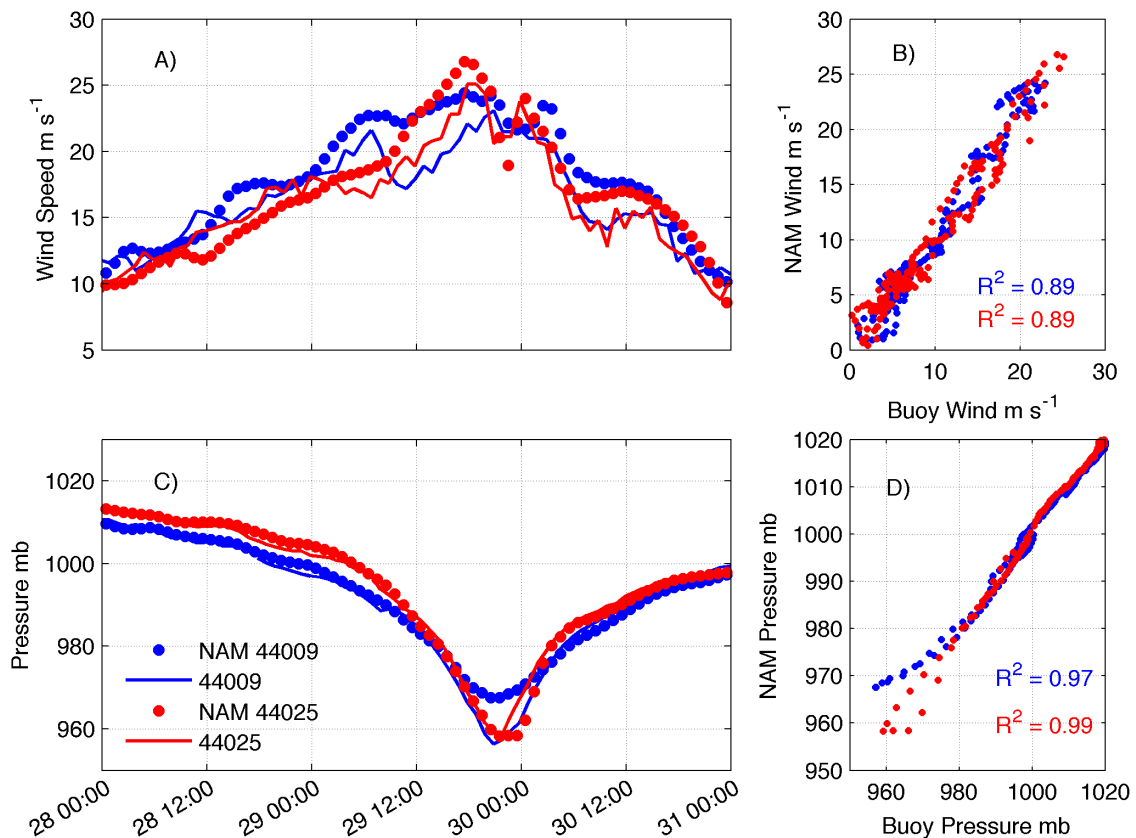
Figure 4.5 Comparisons of (dots) NAM and (lines) buoys (blue) 44009 and (red 44025) of A-B) wind speed and C-D) pressure during the storm forcing period. B) NAM versus buoy winds had R^2 values of 0.89 at both 44009 and 44025, root mean square error (RMSE) of 2.16 and 1.74 m s^{-1} for 44009 and 44025, respectively and correlation coefficients of 0.94 for both 44009 and 44025. D) NAM versus buoy pressures had R^2 values of 0.97 and 0.99, RMSE of 3.08 and 1.83 mb and correlation coefficients of 0.98 and 0.99 for 44009 and 44025 respectively. Time on the x-axis is consistent with Figure 4.3.
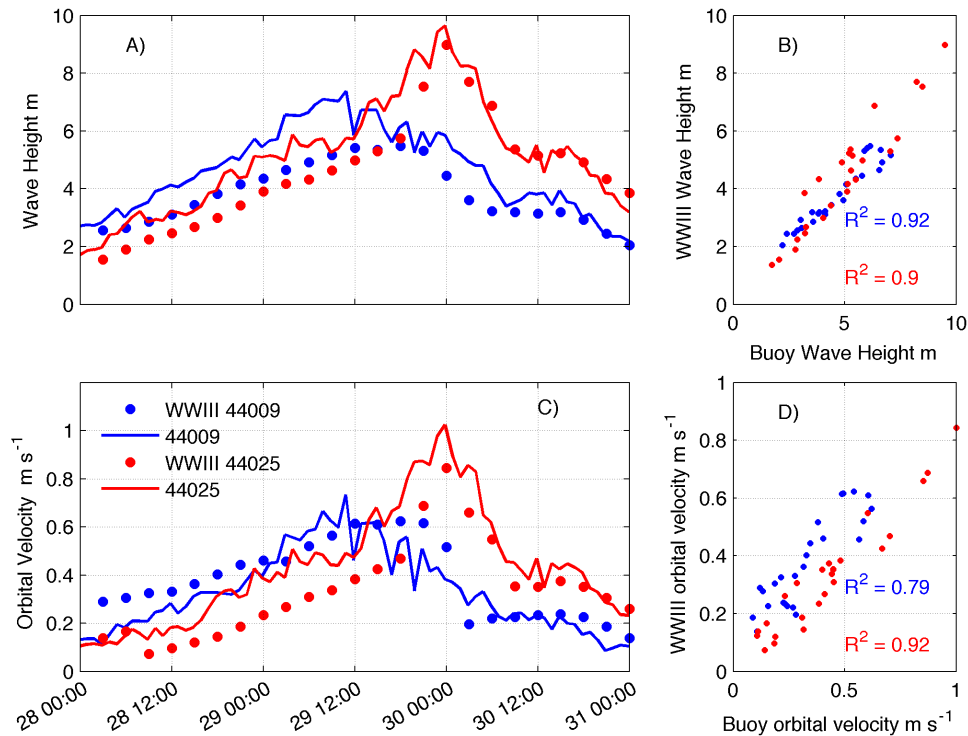
Figure 4.6 Comparisons of (dots) WWIII and (lines) buoys (blue) 44009 and (red 44025) of A-B) wave height and C-D) bottom orbital velocities during the storm forcing period. B) WWIII versus buoy waves had R^2 values of 0.92 and 0.90, root RMSE of 0.98 and 0.83 meters and correlation coefficients of 0.96 and 0.95 for 44009 and 44025, respectively. D) WWIII versus buoy bottom orbital velocities had R^2 values of 0.79 and 0.92, RMSE of 0.09 and 0.12 m s^{-1} and correlation coefficients of 0.88 and 0.96 for 44009 and 44025, respectively. Time on the x-axis is consistent with Figure 4.3.
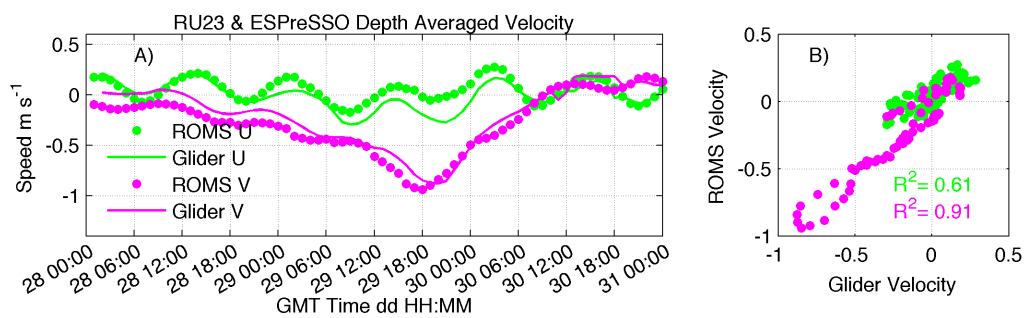
Figure 4.7 Comparisons of depth averaged (dots) ROMS and (lines) glider depth averaged currents calculated along the glider track in the (green) cross-shelf and (pink) along-shelf directions. ROMs versus glider comparisons have R^2 values of 0.61 and 0.91, RMSE values of 0.10 and 0.104 and correlation coefficients of 0.78 and 0.95 for (green) cross- and (pink) along- shelf velocities, respectively. Positive values indicate along-shelf (cross-shelf) toward the northeast (offshore).
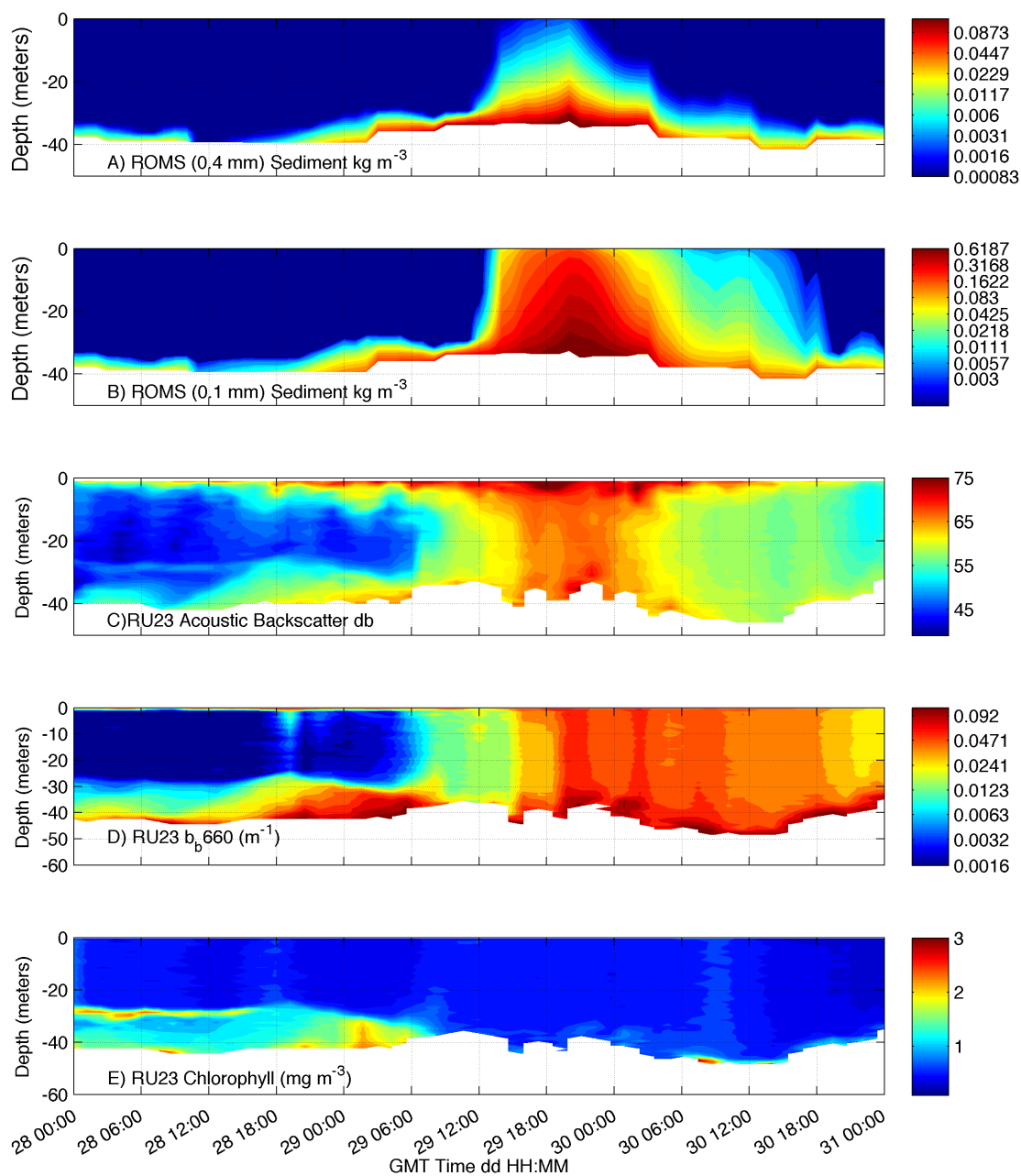
Figure 4.8 Cross-sections of modeled sediment concentrations along the glider track for A) 0.4mm grain sizes, B) 0.1mm grain sizes and observed cross sections of C) Acoustic backscatter, D) Optical backscatter at 660 nanometers and E) Chlorophyll concentration. Times along the x-axis are as in Figure 4.3.
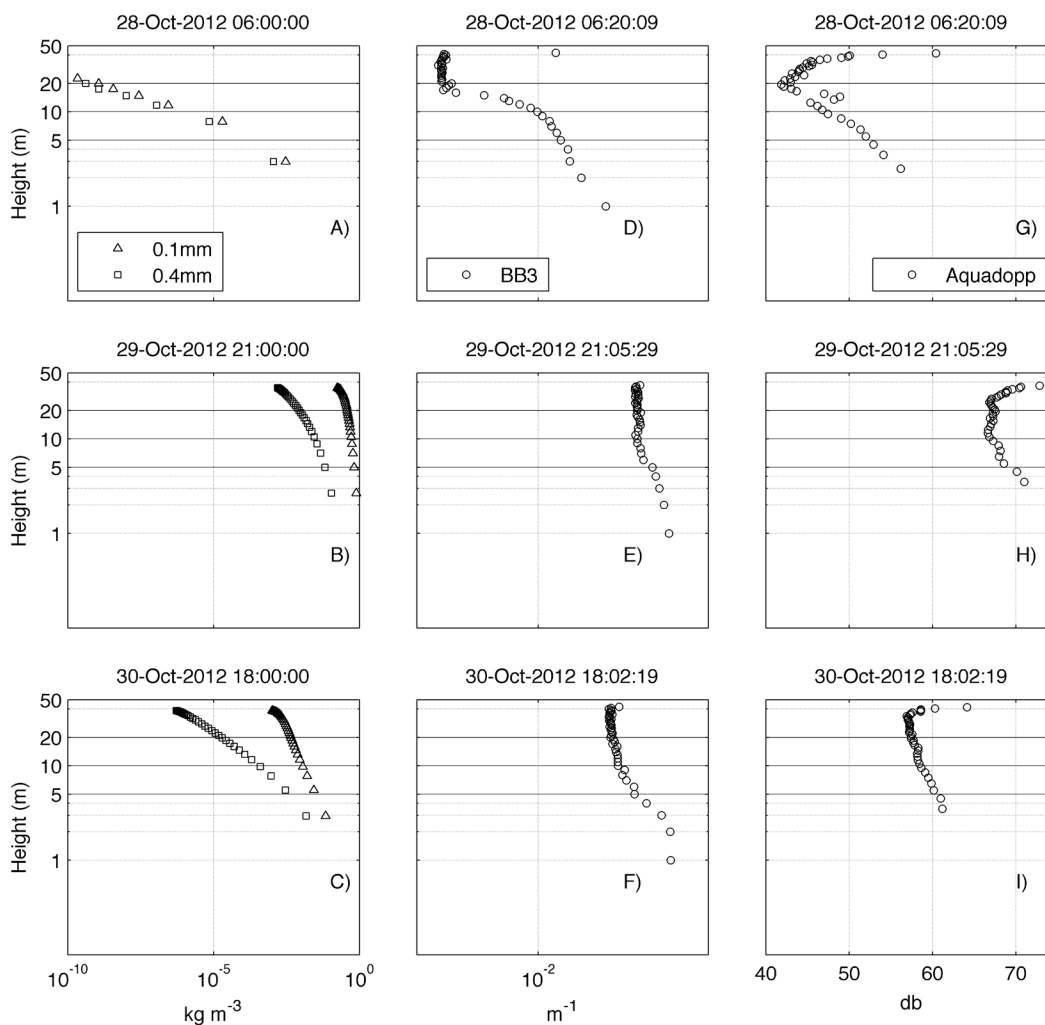
Figure 4.9 Log-log profiles of modeled 0.1 mm (triangles) and 0.4mm (squares) sediment concentration (A-C) optical backscatter (D-F) and semi-log profiles of acoustic backscatter (G-I). Acoustic backscatter has a logarithmic response to increased sediment concentration at the target frequency thus.
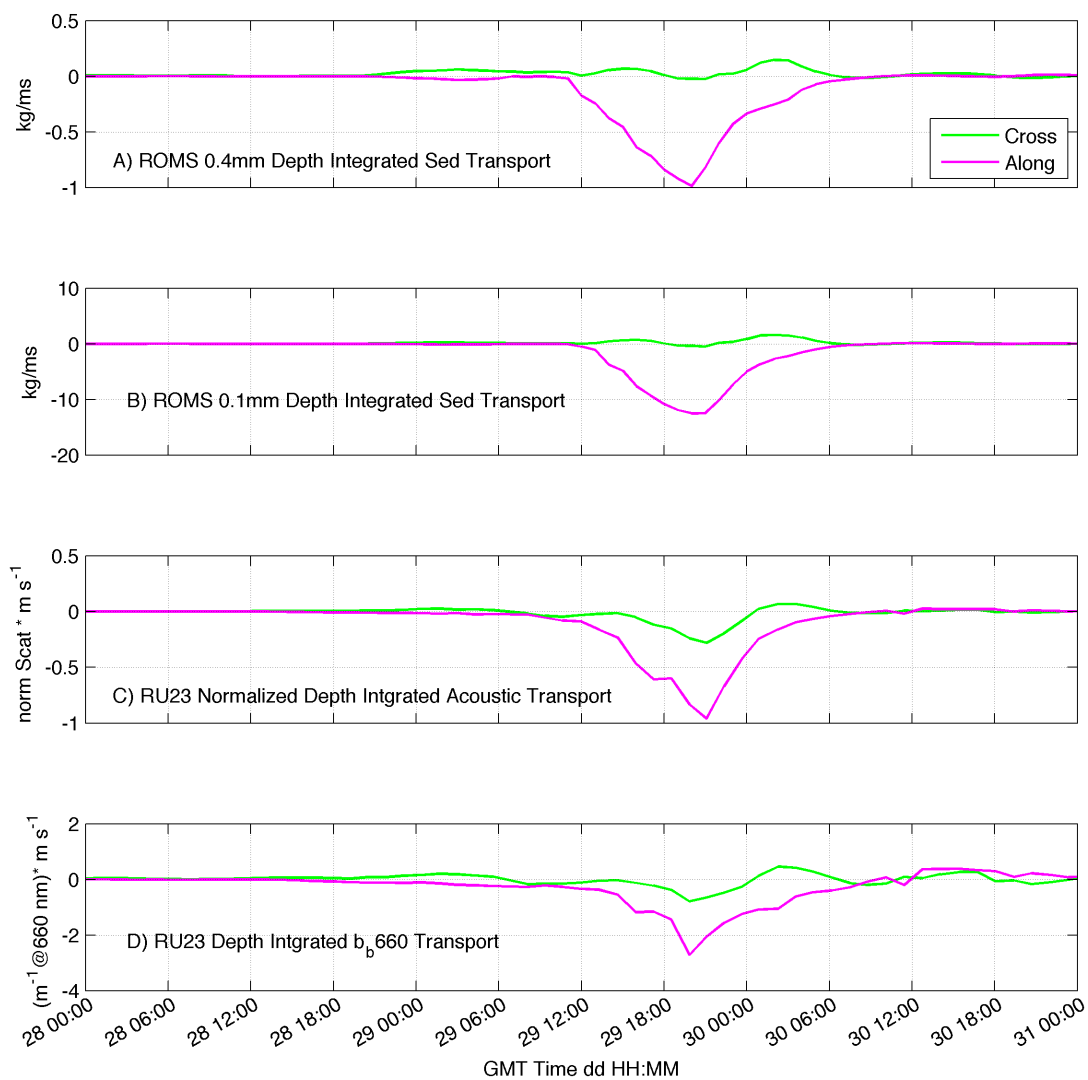
Figure 4.10 Depth averaged transports calculated along the glider track for modeled A) 0.4 mm sediment, B) 0.1mm sediment, C) Normalized depth integrated acoustic transport, and depth integrated optical backscatter transport in the (green) cross-and (pink) along- shelf directions. Positive values indicate along-shelf (cross-shelf) toward the northeast (offshore).
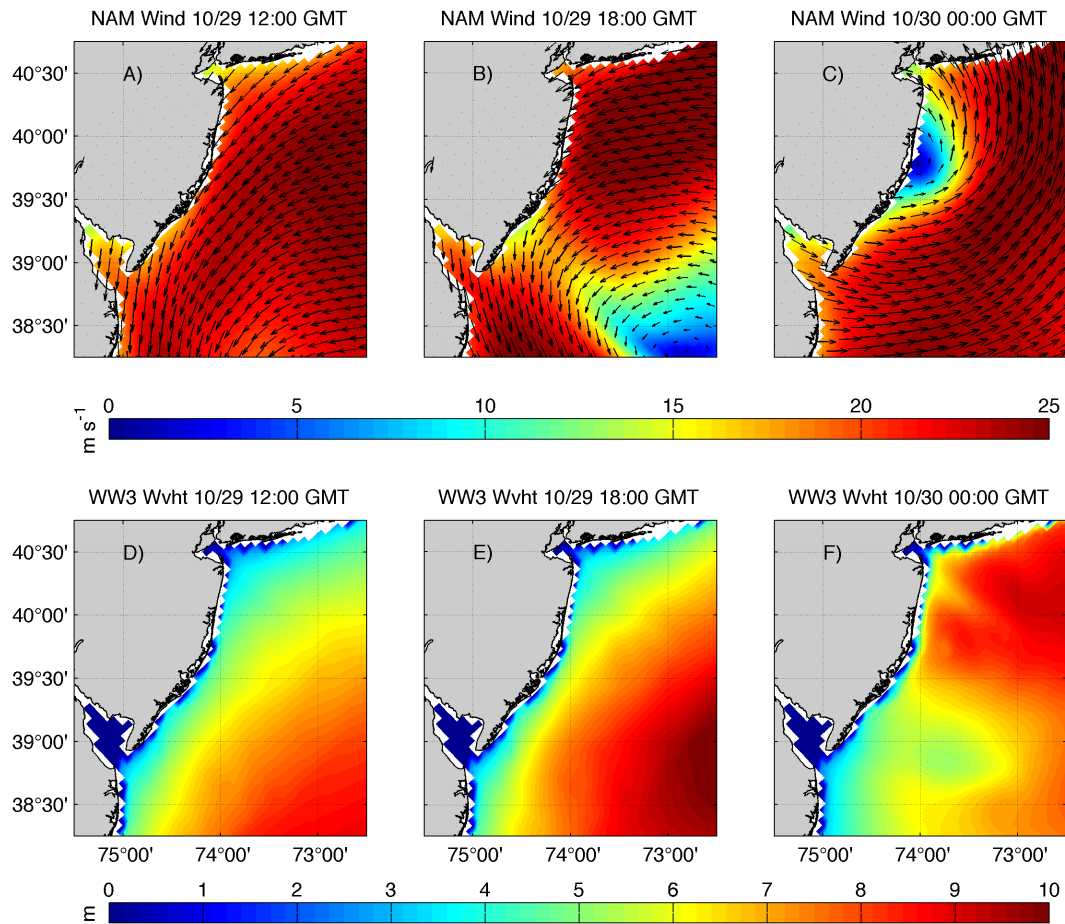
Figure 4.11 Panels of (A-C) NAM Wind on October 29th at A) 12:00 GMT, B) 18:00 GMT and C) October 30th at 00:00 GMT. Panels of (D-F) WWII wave heights on October 29th at D) 12:00 GMT, E) 18:00 GMT and F) October 30th at 00:00 GMT.
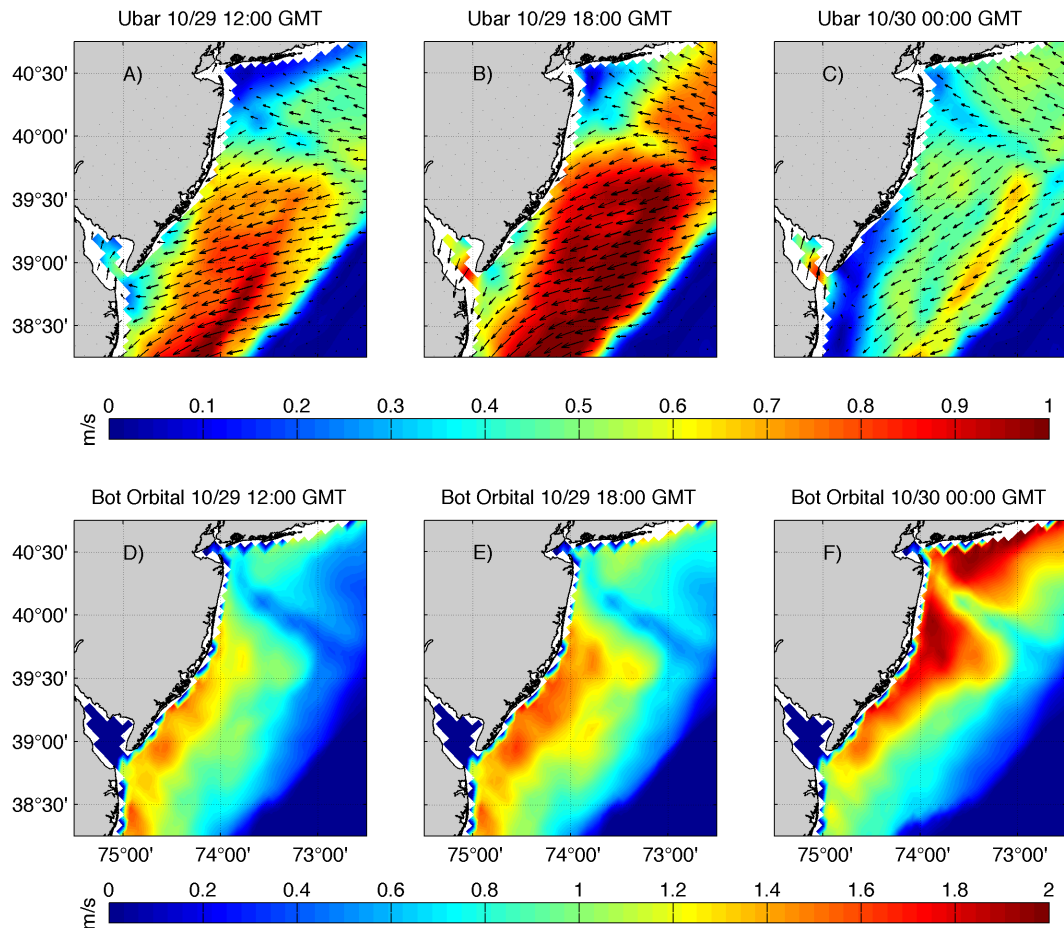
Figure 4.12 Panels of (A-C) ROMS depth averaged currents on October 29th at A) 12:00 GMT, B) 18:00 GMT and C) October 30th at 00:00 GMT. Panels of (D-F) bottom orbital velocities on October 29th at D) 12:00 GMT, E) 18:00 GMT and F) October 30th at 00:00 GMT.

Figure 4.13 Panels of (A-C) ROMS depth integrated 0.4mm sediment concentration on October 29th at A) 12:00 GMT, B) 18:00 GMT and C) October 30th at 00:00 GMT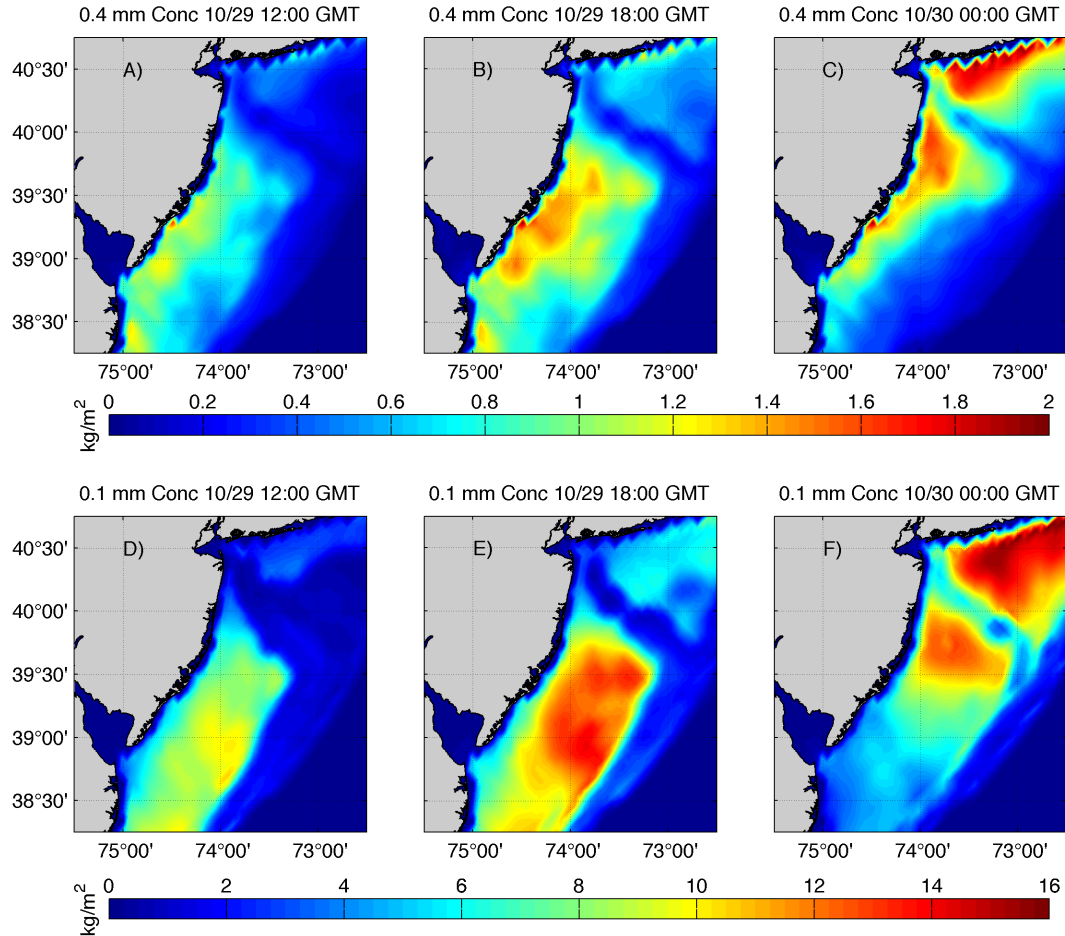. Panels of (D-F) ROMS depth integrated 0.1mm sediment concentration on October 29th at D) 12:00 GMT, E) 18:00 GMT and F) October 30th at 00:00 GMT.
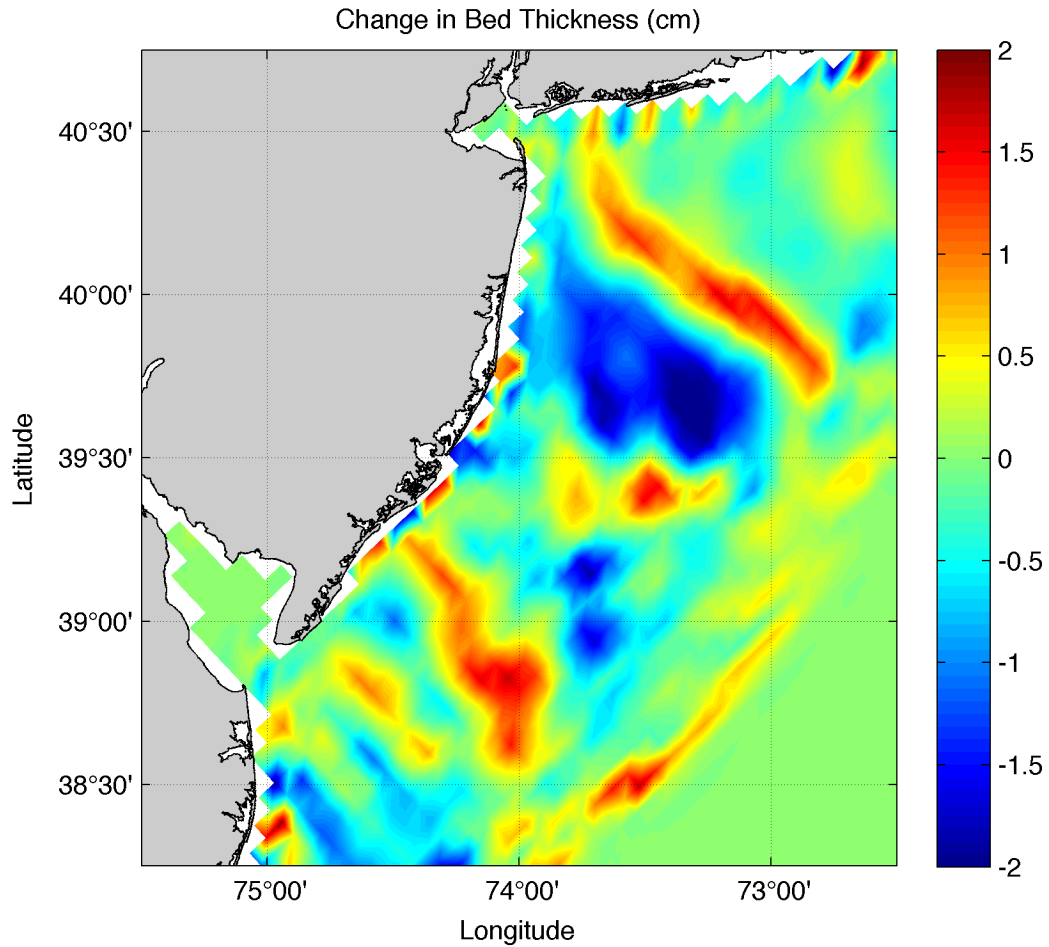
Figure 4.14 Change in bed thickness between the model initialization on October 23rd 2012 at 00:00 GMT and October 31st at 08:00 GMT, with positive values indicating net deposition and negative values net erosion.

Chapter 5

Summary and Conclusions

This dissertation presents data from multiple Teledyne-Webb Slocum gliders within a broader regional scale ocean observatory deployed in a Nor'easter, NorIda in November of 2009, and Hurricane Sandy in October of 2012. In Chapter 2 we presented data from multiple gliders in the 2009 NorIda storm to characterize small scale (O10 Km) spatial variability in sediment resuspension and transport due to varying bed types across the New Jersey shelf. One major drawback of this early study was an inability to measure realistic water-column currents. To improve upon this for future studies we included a Nortek Aquadopp current profiler mounted in an upward looking position onboard RU23 for deployment into Hurricane Sandy in October of 2012. The combination of the standard glider sampling package and the Aquadopp allowed for an unprecedented view of the evolution of the thermocline and coastal ocean during Hurricane Sandy in Chapter 3 of this study. This Aquadopp glider combination also provided invaluable acoustic and optical backscatter measurements that allowed for broad regional scale validation of sediment resuspend and transport within Hurricane Sandy.

Gliders continue to be disruptive technologies that open up new frontiers in oceanography. With this dissertation we demonstrate that these technologies can not only sample in some of the most extreme weather conditions on the planet, but that they are ideally suited to do it efficiently and with high temporal resolution. The collection of new observations in these extreme events will help drive process driven improvements to predictive atmospheric, ocean and sediment transport and

resuspension models. Future advances include sediment resuspension and transport sensitivity studies using a broader array of sediment types and realistic bed conditions, calibration of acoustic and optical sensors with *in situ* sediment to observe realistic concentrations, and integrated downward looking acoustic sensors for improved bottom stress and potentially turbulence measurements within storm conditions.

References

Agrawal, Y. C., and H. C. Pottsmith (2000), Instruments for particle size and settling velocity observations in sediment transport, *Mar. Geol.*, *168*(1‚Äì4), 89–114, doi:10.1016/s0025-3227(00)00044-x.

Agrawal, Y. Y. C. (2005), The optical volume scattering function: Temporal and vertical variability in the water column off the New Jersey coast, *Limnol. Oceanogr.*, *50*(6), 1787–1794.

Amato (1994), Sand and Gravel Maps of the Atlantic Continental Shelf, edited by M. M. Service, *OCS Monogr. MMS*, *93-0037*, 35.

Ariathurai, R., and K. Arulanandan (1978), Erosion rates of cohesive soils, *J. Hydraul. Div. Proc. ASCE*, *104*(2), 279–283.

Austin, J., and S. Lentz (2002), The inner shelf response to wind-driven upwelling and downwelling., *J. Phys. Oceanogr.*, (1905), 2171–2193.

Babin, S. M. (2004), Satellite evidence of hurricane-induced phytoplankton blooms in an oceanic desert, *J. Geophys. Res.*, *109*(C3), C03043, doi:10.1029/2003JC001938.

Barrick, D. E. (1971a), Theory of HF and VHF Propagation Across the Rough Sea, 1, The Effective Surface Impedance for a Slightly Rough Highly Conducting Medium at Grazing Incidence, *Radio Sci.*, *6*(5), 517–526, doi:10.1029/RS006i005p00517.

Barrick, D. E. (1971b), Theory of HF and VHF Propagation Across the Rough Sea, 2, Application to HF and VHF Propagation Above the Sea, *Radio Sci.*, *6*(5), 527–533, doi:10.1029/RS006i005p00527.

Beardsley, R. C., and W. C. Boicourt (1981), On estuarine and continental-shelf circulation in the Middle Atlantic Bight, in *Evolution of physical oceanography*, edited by B. A. Warren and C. Wunsch, pp. 198–233, The MIT press.

Bender, M., and I. Ginis (2000), Real-Case Simulations of Hurricane–Ocean Interaction Using A High-Resolution Coupled Model: Effects on Hurricane Intensity., *Mon. Weather Rev.*, 917–946.

Bigelow, H. (1933), Studies of the waters on the continental shelf, Cape Cod to Chesapeake Bay. I. The cycle of temperature, *Pap. Phys. Oceanogr. Meteorol.*, *2*(4).

Blaas, M., C. Dong, P. Marchesiello, J. C. McWilliams, and K. D. Stolzenbach (2007), Sediment-transport modeling on Southern Californian shelves: A ROMS case study, *Cont. Shelf Res.*, *27*(6), 832–853, doi:10.1016/j.csr.2006.12.003.

Black, P. G., E. A. D'Asaro, T. B. Sanford, W. M. Drennan, J. A. Zhang, J. R. French, P. P. Niiler, E. J. Terrill, and E. J. Walsh (2007), Air–Sea Exchange in Hurricanes: Synthesis of Observations from the Coupled Boundary Layer Air–Sea Transfer Experiment, *Bull. Am. Meteorol. Soc.*, *88*(3), 357–374, doi:10.1175/BAMS-88-3-357.

Blake, E. S., T. B. Kimberlain, R. J. Berg, P. C. John, and J. L. Beven II (2013), Tropical Cyclone Report: Hurricane Sandy, *Natl. Hurric. Cent.*, *12*.

Boss, E., and W. Pegau (2001), Relationship of light scattering at an angle in the backward direction to the backscattering coefficient, *Appl. Opt.*, *40*(30), 5503, doi:10.1364/AO.40.005503.

Boss, E., W. S. Pegau, M. Lee, M. Twardowski, E. Shybanov, G. Korotaev, and F. Baratange (2004), Particulate backscattering ratio at LEO 15 and its use to study particle composition and distribution, *J. Geophys. Res. Ocean.*, *109*(C1), C01014, doi:10.1029/2002JC001514.

Boss, E. et al. (2009), Comparison of inherent optical properties as a surrogate for particulate matter concentration in coastal waters, *Limnol. Oceanogr. Methods*, *7*, 803–810.

Bunt, J. a. C., P. Larcombe, and C. F. Jago (1999), Quantifying the response of optical backscatter devices and transmissometers to variations in suspended particulate matter, *Cont. Shelf Res.*, *19*(9), 1199–1220, doi:10.1016/S0278-4343(99)00018-7.

Cacchione, D., and W. Grant (1987), Storm-Dominated Bottom Boundary Layer Dynamics on the Northern California Continental Shelf: Measurements and Predictions, *J. Geophys. ...*, *92*(1817), 1817–1827.

Cacchione, D. a., P. D. Thorne, Y. Agrawal, and N. J. Nidzieko (2008), Time-averaged near-bed suspended sediment concentrations under waves and currents: Comparison of measured and model estimates, *Cont. Shelf Res.*, *28*(3), 470–484, doi:10.1016/j.csr.2007.10.006.

Cahill, B., O. Schofield, R. Chant, J. Wilkin, E. Hunter, S. Glenn, and P. Bissett (2008), Dynamics of turbid buoyant plumes and the feedbacks on near-shore biogeochemistry and physics, *Geophys. Res. Lett.*, *35*(10), L10605, doi:10.1029/2008GL033595.

Castelao, R., S. Glenn, and O. Schofield (2010), Temperature, salinity, and density variability in the central Middle Atlantic Bight, *J. Geophys. Res.*, *115*(C10), C10005, doi:10.1029/2009JC006082.

Chang, G. C., T. D. Dickey, and A. J. Williams (2001), Sediment resuspension over a continental shelf during Hurricanes Edouard and Hortense, *J. Geophys. Res. Ocean.*, *106*(C5), 9517–9531, doi:10.1029/2000JC900032.

Chant, R. J., W. R. Geyer, R. Houghton, E. Hunter, and J. Lerczak (2007), Estuarine Boundary Layer Mixing Processes: Insights from Dye Experiments*, *J. Phys. Oceanogr.*, *37*(7), 1859–1877, doi:10.1175/JPO3088.1.

Chapman, R., and H. Graber (1997), Validation of HF radar measurements, *Oceanogr. Soc.*, *10*(2), 76–79, doi:10.5670.

Chen, K., and R. He (2010), Numerical Investigation of the Middle Atlantic Bight Shelfbreak Frontal Circulation Using a High-Resolution Ocean Hindcast Model., *J. Phys. Oceanogr.*, *40*(5), 949–964, doi:10.1175/2009JPO4262.1.

Cione, J. J., and E. W. Uhlhorn (2003), Sea Surface Temperature Variability in Hurricanes: Implications with Respect to Intensity Change, *Mon. Weather Rev.*, *131*(8), 1783–1796, doi:10.1175//2562.1.

D'Asaro, E. a., T. B. Sanford, P. P. Niiler, and E. J. Terrill (2007), Cold wake of Hurricane Frances, *Geophys. Res. Lett.*, *34*(15), L15609, doi:10.1029/2007GL030160.

Davis, R., C. Eriksen, and C. Jones (2003), Autonomous Buoyancy-driven Underwater Gliders, in *Technology and Applications of Autonomous Underwater Vehicles*, edited by G. Griffiths, p. 37, Taylor & Francis.

Drake, D. E., and D. A. Cacchione (1992), Wave—current interaction in the bottom boundary layer during storm and non-storm conditions: observations and model predictions, *Cont. Shelf Res.*, *12*(12), 1331–1352, doi:10.1016/0278-4343(92)90058-R.

Dzwonkowski, B., J. T. Kohut, and X.-H. Yan (2009a), Seasonal differences in wind-driven across-shelf forcing and response relationships in the shelf surface layer of the central Mid-Atlantic Bight, *J. Geophys. Res. Ocean.*, *114*(C8), C08018, doi:10.1029/2008JC004888.

Dzwonkowski, B., J. T. Kohut, and X.-H. Yan (2009b), Sub-inertial characteristics of the surface flow field over the shelf of the central Mid-Atlantic Bight, *Cont. Shelf Res.*, *29*(15), 1873–1886, doi:10.1016/j.csr.2009.07.005.

Emanuel, K., C. DesAutels, C. Holloway, and R. Korty (2004), Environmental Control of Tropical Cyclone Intensity, *J. Atmos. Sci.*, *61*(7), 843–858, doi:10.1175/1520-0469.

Emanuel, K. A. (1999), Thermodynamic control of hurricane intensity, *Nature*, *401*(6754), 665–669.

Fairall, C., and E. Bradley (1996), Bulk parameterization of air-sea fluxes for Tropical Ocean- Global Atmosphere Coupled-Ocean Atmosphere Response Experiment, *J. Geophys. Res.*, *101*(C2), 3747–3764.

Fairall, C. W., E. F. Bradley, J. E. Hare, A. A. Grachev, and J. B. Edson (2003), Bulk Parameterization of Air–Sea Fluxes: Updates and Verification for the COARE Algorithm., *J. Clim.*, *16*(4), 571.

Falkowski, P. G., and J. A. Raven (2007), *Aquatic photosynthesis*, Princeton University Press, Princeton, New Jersey.

Falkowski, P. G., J. Vidal, T. S. Hopkins, G. T. Rowe, T. E. Whitledge, and W. G. Harrison (1983), Summer nutrient dynamics in the Middle Atlantic Bight: primary production and utilization of phytoplankton carbon, *J. Plankt. Res.* , *5* (4), 515–537, doi:10.1093/plankt/5.4.515.

Fandry, C. B., and R. K. Steedman (1994), Modelling the dynamics of the transient, barotropic response of continental shelf waters to tropical cyclones, *Cont. Shelf Res.*, *14*(15), 1723–1750, doi:10.1016/0278-4343(94)90045-0.

Gangopadhyay, A., A. Schmidt, L. Agel, O. Schofield, and J. Clark (2013), Multiscale forecasting in the western North Atlantic: Sensitivity of model forecast skill to glider data assimilation, *Cont. Shelf Res.*, *63*, S159–S176, doi:10.1016/j.csr.2012.09.013.

Gargett, A., J. Wells, A. E. Tejada-Martínez, and C. E. Grosch (2004), Langmuir Supercells: A Mechanism for Sediment Resuspension and Transport in Shallow Seas, *Sci.* , *306* (5703), 1925–1928, doi:10.1126/science.1100849.

Glahn, B., A. Taylor, N. Kurkowski, and W. A. Shaffer (2009), The role of the SLOSH model in National Weather Service storm surge forecasting, *Natl. Weather Dig.*, *33*(1), 3–14.

Glenn, S. (2004), Biogeochemical impact of summertime coastal upwelling on the New Jersey Shelf, *J. Geophys. Res.*, *109*, doi:10.1029/2003JC002265.

Glenn, S., and O. Schofield (2009), Growing a Distributed Ocean Observatory: Our View from the COOL Room, *Oceanography*, *22*(2), 128–145, doi:10.5670/oceanog.2009.44.

Glenn, S., C. Jones, M. Twardowski, L. Bowers, J. Kerfoot, J. Kohut, D. Webb, and O. Schofield (2008), Glider observations of sediment resuspension in a Middle Atlantic Bight fall transition storm, *Limnol. Oceanogr.*, *53*(5 part 2), 2180–2196, doi:10.4319/lo.2008.53.5_part_2.2180.

Glenn, S. M., and W. D. Grant (1987), A suspended sediment stratification correction for combined wave and current flows, *J. Geophys. Res.*, *92*(C8), 8244, doi:10.1029/JC092iC08p08244.

Goff, J. a., C. J. Jenkins, and S. Jeffress Williams (2008), Seabed mapping and characterization of sediment variability using the usSEABED data base, *Cont. Shelf Res.*, *28*(4-5), 614–633, doi:10.1016/j.csr.2007.11.011.

Gong, D., J. Kohut, and S. Glenn (2010), Seasonal climatology of wind-driven circulation on the New Jersey Shelf, *J. Geophys. Res. Ocean. (…*, *115*(C4), 953–968, doi:10.1029/2009JC005520.

Grant, W., and O. Madsen (1979), Combined Wave and Current Interaction with a Rough Bottom, *J. Geophys. Res. …*, *84*(8), 1797–1808.

Grant, W. D., and O. S. Madsen (1986), The Continental-Shelf Bottom Boundary Layer, *Annu. Rev. Fluid Mech.*, *18*(1), 265–305, doi:10.1146/annurev.fl.18.010186.001405.

Haidvogel, D. B. et al. (2008), Ocean forecasting in terrain-following coordinates: Formulation and skill assessment of the Regional Ocean Modeling System, *J. Comput. Phys.*, *227*(7), 3595–3624, doi:10.1016/j.jcp.2007.06.016.

Hall, T. M., and A. H. Sobel (2013), On the impact angle of Hurricane Sandy's New Jersey landfall, *Geophys. Res. Lett.*, *40*(10), 2312–2315, doi:10.1002/grl.50395.

Harcourt, R. R., and E. a. D'Asaro (2010), Measurement of Vertical Kinetic Energy and Vertical Velocity Skewness in Oceanic Boundary Layers by Imperfectly Lagrangian Floats., *J. Atmos. Ocean. Technol.*, *27*(11), 1918–1935, doi:10.1175/2010JTECHO731.1.

Harris, C., and P. Wiberg (2002), Across-shelf sediment transport: Interactions between suspended sediment and bed sediment, *J. Geophys. Res.*, *107*(C1), doi:10.1029/2000JC000634.

Harris, C. K., B. Butman, and P. Traykovski (2003), Winter-time circulation and sediment transport in the Hudson Shelf Valley, *Cont. Shelf Res.*, *23*(8), 801–820, doi:10.1016/S0278-4343(03)00025-6.

Hofmann, E., J.-N. Druon, K. Fennel, M. Friedrichs, D. Haidvogel, C. Lee, A. Mannino, C. McClain, R. Najjar, and J. O'Reilly (2008), Eastern US continental shelf carbon budget integrating models, data assimilation, and analysis, *Oceanography*.

Houghton, R. W., R. Schlitz, R. C. Beardsley, B. Butman, and J. L. Chamberlin (1982), The Middle Atlantic Bight Cold Pool: Evolution of the Temperature Structure During Summer 1979, *J. Phys. Oceanogr.*, *12*(10), 1019–1029, doi:10.1175/1520-0485.

Hu, K., P. Ding, Z. Wang, and S. Yang (2009), A 2D/3D hydrodynamic and sediment transport model for the Yangtze Estuary, China, *J. Mar. Syst.*, *77*(1-2), 114–136, doi:10.1016/j.jmarsys.2008.11.014.

Jarosz, E., D. a Mitchell, D. W. Wang, and W. J. Teague (2007), Bottom-up determination of air-sea momentum exchange under a major tropical cyclone., *Science*, *315*(5819), 1707–9, doi:10.1126/science.1136466.

Jelesnianski, C. P., J. Chen, and W. A. Shaffer (1992), *SLOSH: Sea, lake, and overland surges from hurricanes*, US Department of Commerce, National Oceanic and Atmospheric Administration, National Weather Service.

Keen, T., and S. Glenn (2002), Predicting bed scour on the continental shelf during Hurricane Andrew, *J. Waterw. port, coastal, Ocean ...*, *128*(6), 249–257, doi:10.1061/(ASCE)0733-950X(2002)128:6(249).

Keen, T. R., and S. M. Glenn (1995), A Coupled Hydrodynamic–Bottom Boundary Layer Model of Storm and Tidal Flow in the Middle Atlantic Bight of North America, *J. Phys. Oceanogr.*, *25*(3), 391–406, doi:10.1175/1520-0485(1995)025<0391:ACHBLM>2.0.CO;2.

Keim, B. D., R. A. Muller, and G. W. Stone (2004), Spatial and temporal variability of coastal storms in the North Atlantic Basin, *Mar. Geol.*, *210*(1-4), 7–15, doi:10.1016/j.margeo.2003.12.006.

Keim, B. D., R. a. Muller, and G. W. Stone (2007), Spatiotemporal Patterns and Return Periods of Tropical Storm and Hurricane Strikes from Texas to Maine, *J. Clim.*, *20*(14), 3498–3509, doi:10.1175/JCLI4187.1.

Kim, S.-C., L. D. Wright, and B.-O. Kim (1997), The combined effects of synoptic-scale and local-scale meteorological events on bed stress and sediment transport on the inner shelf of the Middle Atlantic Bight, *Cont. Shelf Res.*, *17*(4), 407–433, doi:10.1016/S0278-4343(96)00038-6.

Kohut, J. T., S. M. Glenn, and J. D. Paduan (2006), Inner shelf response to Tropical Storm Floyd, *J. Geophys. Res.*, *111*(C9), C09S91, doi:10.1029/2003JC002173.

Lentz, S. (2001), The Influence of Stratification on the Wind-Driven Cross-Shelf Circulation over the North Carolina Shelf*, *J. Phys. Oceanogr.*, (Lentz 1995), 2749–2760.

Lentz, S., R. T. Guza, S. Elgar, F. Feddersen, and T. H. C. Herbers (1999), Momentum balances on the North Carolina inner shelf, *J. Geophys. Res.*, *104*(C8), 18205, doi:10.1029/1999JC900101.

Lentz, S. J. (2003), A climatology of salty intrusions over the continental shelf from Georges Bank to Cape Hatteras, *J. Geophys. Res.*, *108*, doi:10.1029/2003JC001859.

Lentz, S. J. (2008), Seasonal Variations in the Circulation over the Middle Atlantic Bight Continental Shelf, *J. Phys. Oceanogr.*, *38*(7), 1486–1500, doi:10.1175/2007JPO3767.1.

Lohrmann, A. (2001), Monitoring sediment concentration with acoustic backscattering instruments, *Nortek Tech. Note*, (I), 1–5.

Lynch, J. F., T. F. Gross, C. R. Sherwood, J. D. Irish, B. H. Brumley, and J. D. and B. Lynch, J.F., Gross, T.F., Sherwood, C.R., Irish (1997), Acoustical and optical backscatter measurements of sediment transport, , *17*(4), 337–366.

Madsen, O. (1994), Spectral wave-current bottom boundary layer flows, *Coast. Eng. Proc.*, 384–398.

Madsen, O., and P. Wikramanayake (1991), Simple models for turbulent wave-current bottom boundary layer flow,

McBride, R. A., and T. F. Moslow (1991), Origin, evolution, and distribution of shoreface sand ridges, Atlantic inner shelf, U.S.A., *Mar. Geol.*, *97*(1-2), 57–85, doi:10.1016/0025-3227(91)90019-Z.

McLean, S. (1991), Depth-integrated suspended-load calculations, *J. Hydraul. Eng.*, *117*(11), 1440–1458.

Meyer-Peter, E., and R. Müller (1948), Formulas for bed-load transport, in *Proceedings of the 2nd Meeting of the International Association for Hydraulic Structures Research*, pp. 39–64.

Miles, T., S. Glenn, and O. Schofield (2013), Temporal and spatial variability in fall storm induced sediment resuspension on the Mid-Atlantic Bight, *Cont. Shelf Res.*, *63*.

Ogston, a. ., D. . Cacchione, R. . Sternberg, and G. . Kineke (2000), Observations of storm and river flood-driven sediment transport on the northern California

continental shelf, *Cont. Shelf Res.*, *20*(16), 2141–2162, doi:10.1016/S0278-4343(00)00065-0.

Ogston, A. S., and R. W. Sternberg (1999), Sediment-transport events on the northern California continental shelf, *Mar. Geol.*, *154*, 69–82, doi:10.1016/S0025-3227(98)00104-2.

Ohlmann, C., P. White, L. Washburn, E. Terrill, B. Emery, and M. Otero (2007), Interpretation of Coastal HF Radar–Derived Surface Currents with High-Resolution Drifter Data., *J. Atmos. Ocean. Technol.*, *24*(4), 666–680.

Olabarrieta, M., J. Warner, and B. Armstrong (2012), Ocean–atmosphere dynamics during Hurricane Ida and Nor'Ida: An application of the coupled ocean–atmosphere–wave–sediment transport (COAWST) modeling system, *Ocean Model.*, *43-44*, 112–137, doi:10.1016/j.ocemod.2011.12.008.

Papanicolaou, A., and M. Elhakeem (2008), Sediment Transport Modeling Review — Current and Future Developments, *J. Hydraul. ...*, (January), 1–14.

Price, J. F. (1981), Upper Ocean Response to a Hurricane, *J. Phys. Oceanogr.*, *11*(2), 153–175, doi:10.1175/1520-0485(1981)011<0153:UORTAH>2.0.CO;2.

Price, J. F. (2009), Metrics of hurricane-ocean interaction: vertically-integrated or vertically-averaged ocean temperature?, *Ocean Sci.*, *5*(3), 351–368, doi:10.5194/os-5-351-2009.

Reid, J. M., J. A. Reid, C. J. Jenkins, M. E. Hastings, S. J. Williams, and L. J. Poppe (2005), *usSEABED: Atlantic coast offshore surficial sediment data release*, US Geological Survey.

Roarty, H. et al. (2010), Operation and Application of a Regional High-Frequency Radar Network in the Mid-Atlantic Bight, *Mar. Technol. Soc. J.*, *44*(6), 133–145.

Roesler, C. S., and E. Boss (2008), In situ measurement of the inherent optical properties (IOPs) and potential for harmful algal bloom detection and coastal ecosystem observations, in *Real-Time Coastal Observing Systems for Ecosystem Dynamics and Harmful Algal Blooms*, pp. 153–206, UNESCO Publishing.

Ruiz, S., L. Renault, B. Garau, and J. Tintoré (2012), Underwater glider observations and modeling of an abrupt mixing event in the upper ocean, *Geophys. Res. Lett.*, *39*(1), n/a–n/a, doi:10.1029/2011GL050078.

Sanford, T. B., J. F. Price, J. B. Girton, and D. C. Webb (2007), Highly resolved observations and simulations of the ocean response to a hurricane, *Geophys. Res. Lett.*, *34*(13), L13604, doi:10.1029/2007GL029679.

Sanford, T. B., J. F. Price, and J. B. Girton (2011), Upper-Ocean Response to Hurricane Frances (2004) Observed by Profiling EM-APEX Floats *, *J. Phys. Oceanogr.*, *41*(6), 1041–1056, doi:10.1175/2010JPO4313.1.

Schofield, O. et al. (2007), Slocum Gliders: Robust and ready, *J. F. Robot.*, *24*(6), 473–485, doi:10.1002/rob.20200.

Schofield, O. et al. (2010a), A Regional Slocum Glider Network in the Mid-Atlantic Bight Leverages Broad Community Engagement, *Mar. Technol. Soc. J.*, *44*(6), 185–195.

Schofield, O. et al. (2010b), Automated Sensor Network to Advance Ocean Science, *Eos, Trans. Am. Geophys. Union*, *91*(39), 345–346, doi:10.1029/2010EO390001.

Shchepetkin, A., and J. McWilliams (2009), Computational kernel algorithms for fine-scale, multi-process, long-time oceanic simulations, *… Comput. Methods …*, *14*(08), 121–183, doi:10.1016/S1570-8659(08)01202-0.

Shchepetkin, A. F., and J. C. McWilliams (2005), The regional oceanic modeling system (ROMS): a split-explicit, free-surface, topography-following-coordinate oceanic model, *Ocean Model.*, *9*(4), 347–404, doi:10.1016/j.ocemod.2004.08.002.

Sherman, J., R. E. Davis, W. B. Owens, and J. Valdes (2001), The autonomous underwater glider "Spray," *IEEE J. Ocean. Eng.*, *26*(4), 437–446, doi:10.1109/48.972076.

Sherwood, C. R., B. Butman, D. A. Cacchione, D. E. Drake, T. F. Gross, R. W. Sternberg, P. L. Wiberg, and A. J. Williams (1994), Sediment-transport events on the northern California continental shelf during the 1990–1991 STRESS experiment, *Cont. Shelf Res.*, *14*(10-11), 1063–1099, doi:10.1016/0278-4343(94)90029-9.

Soulsby, R. L., and J. S. Damgaard (2005), Bedload sediment transport in coastal waters, *Coast. Eng.*, *52*(8), 673–689, doi:10.1016/j.coastaleng.2005.04.003.

Stewart, R. H., and J. W. Joy (1974), HF radio measurements of surface currents, *Deep Sea Res. Oceanogr. Abstr.*, *21*(12), 1039–1049, doi:10.1016/0011-7471(74)90066-7.

Styles, R., and S. Glenn (2000), Modeling stratified wave and current bottom boundary layers on the continental shelf, *J. Geophys. Res. Ocean. …*, *105*.

Styles, R., and S. Glenn (2002a), *An optimized combined wave and current algorithm for arbitrary bed roughness.*

Styles, R., and S. M. Glenn (2002b), Modeling bottom roughness in the presence of wave-generated ripples, *J. Geophys. Res. Ocean.*, *107*(C8), 15–24, doi:10.1029/2001JC000864.

Styles, R., and S. M. Glenn (2005), Long-term sediment mobilization at a sandy inner shelf, *J. Geophys. Res.*, *110*(C4), C04S90, doi:10.1029/2003JC002175.

Swift, D., and M. Field (1981), Evolution of a classic sand ridge field : Maryland sector , North American inner shelf, *Sedimentology*, 461–482.

Teague, C. C. (1971), *High Frequency Resonant Scattering Techniques for the Observation of Directional Ocean Wave Spectra*, Department of Electrical Engineering, Stanford University.

Teague, W. J., E. Jarosz, T. R. Keen, D. W. Wang, and M. S. Hulbert (2006), Bottom scour observed under Hurricane Ivan, *Geophys. Res. Lett.*, *33*(7), L07607, doi:10.1029/2005GL025281.

Terrill, E. J., W. K. Melville, and D. Stramski (2001), Bubble entrainment by breaking waves and their influence on optical scattering in the upper ocean, *J. Geophys. Res. Ocean.*, *106*(C8), 16815–16823, doi:10.1029/2000JC000496.

Thorne, P. D., and D. M. Hanes (2002), A review of acoustic measurement of small-scale sediment processes, *Cont. Shelf Res.*, *22*(4), 603–632, doi:10.1016/S0278-4343(01)00101-7.

Todd, R. E., D. L. Rudnick, M. R. Mazloff, R. E. Davis, and B. D. Cornuelle (2011a), Poleward flows in the southern California Current System: Glider observations and numerical simulation, *J. Geophys. Res.*, *116*(C2), C02026, doi:10.1029/2010JC006536.

Todd, R. E., D. L. Rudnick, R. E. Davis, and M. D. Ohman (2011b), Underwater gliders reveal rapid arrival of El Niño effects off California's coast, *Geophys. Res. Lett.*, *38*(3), n/a–n/a, doi:10.1029/2010GL046376.

Traykovski, P. (2007), Observations of wave orbital scale ripples and a nonequilibrium time-dependent model, *J. Geophys. Res. Ocean.*, *112*(C6), C06026, doi:10.1029/2006JC003811.

Traykovski, P., A. E. Hay, J. D. Irish, and J. F. Lynch (1999), Geometry, migration, and evolution of wave orbital ripples at LEO-15, *J. Geophys. Res. Ocean.*, *104*(C1), 1505–1524, doi:10.1029/1998JC900026.

Trembanis, A., C. DuVal, J. Beaudoin, V. Schmidt, D. Miller, and L. Mayer (2013), A detailed seabed signature from Hurricane Sandy revealed in bedforms and

scour, *Geochemistry, Geophys. Geosystems*, *14*(10), 4334–4340, doi:10.1002/ggge.20260.

Trowbridge, J. H. (1992), A simple description of the deepening and structure of a stably stratified flow driven by a surface stress, *J. Geophys. Res. Ocean.*, *97*(C10), 15529–15543, doi:10.1029/92JC01512.

Trowbridge, J. H., and A. R. M. Nowell (1994), An introduction to the Sediment TRansport Events on Shelves and Slopes (STRESS) program, *Cont. Shelf Res.*, *14*(10-11), 1057–1061, doi:10.1016/0278-4343(94)90028-0.

Twardowski, M. S., E. Boss, J. B. Macdonald, W. S. Pegau, A. H. Barnard, and J. R. V Zaneveld (2001), A model for estimating bulk refractive index from the optical backscattering ratio and the implications for understanding particle composition in case I and case II waters, *J. Geophys. Res. Ocean.*, *106*(C7), 14129–14142, doi:10.1029/2000JC000404.

Visbeck, M. (2002), Deep Velocity Profiling Useding Lowered Acoustic Doppler Current Profilers: Bottom Track and Inverse Solutions, *J. Atmos. Ocean. Technol.*

Walker, N. . (2006), Hurricane Prediction A Century of Advances, , *19*(2), 24–36.

Warner, J., B. Butman, and P. Dalyander (2008a), Storm-driven sediment transport in Massachusetts Bay, *Cont. Shelf Res.*, *28*(2), 257–282, doi:10.1016/j.csr.2007.08.008.

Warner, J. C., C. R. Sherwood, R. P. Signell, C. K. Harris, and H. G. Arango (2008b), Development of a three-dimensional, regional, coupled wave, current, and sediment-transport model, *Comput. Geosci.*, *34*(10), 1284–1306, doi:10.1016/j.cageo.2008.02.012.

Warner, J. C., B. Armstrong, R. He, and J. B. Zambon (2010), Development of a Coupled Ocean–Atmosphere–Wave–Sediment Transport (COAWST) Modeling System, *Ocean Model.*, *35*(3), 230–244, doi:10.1016/j.ocemod.2010.07.010.

Wiberg, P. (2000), A perfect storm: formation and potential for preservation of storm beds on the continental shelf, *Oceanogr. DC- …*, *13*(3), 93–99, doi:http://dx.doi.org/10.5670/oceanog.2000.18.

Wiberg, P. L., and C. K. Harris (1994), Ripple geometry in wave-dominated environments, *J. Geophys. Res.*, *99*, 775, doi:10.1029/93JC02726.

Wiberg, P. L., and C. R. Sherwood (2008), Calculating wave-generated bottom orbital velocities from surface-wave parameters, *Comput. Geosci.*, *34*(10), 1243–1262, doi:10.1016/j.cageo.2008.02.010.

Wiberg, P. L., D. E. Drake, and D. A. Cacchione (1994), Sediment resuspension and bed armoring during high bottom stress events on the northern California inner continental shelf: measurements and predictions, *Cont. Shelf Res.*, *14*(10-11), 1191–1219, doi:10.1016/0278-4343(94)90034-5.

Wiggert, J. ., B. . Jones, T. . Dickey, K. . Brink, R. . Weller, J. Marra, and L. . Codispoti (2000), The Northeast Monsoon's impact on mixing, phytoplankton biomass and nutrient cycling in the Arabian Sea, *Deep Sea Res. Part II Top. Stud. Oceanogr.*, *47*(7-8), 1353–1385, doi:10.1016/S0967-0645(99)00147-2.

Wilkin, J., and E. Hunter (2013), An assessment of the skill of real-time models of Mid-Atlantic Bight continental shelf circulation, *J. Geophys. Res. …*, *118*(6), 2919–2933, doi:10.1002/jgrc.20223.

Xu, Y., R. Chant, D. Gong, R. Castelao, S. Glenn, and O. Schofield (2011), Seasonal variability of chlorophyll a in the Mid-Atlantic Bight, *Cont. Shelf Res.*, *31*(16), 1640–1650, doi:10.1016/j.csr.2011.05.019.

Xu, Y., B. Cahill, J. Wilkin, and O. Schofield (2013), Role of wind in regulating phytoplankton blooms on the Mid-Atlantic Bight, *Cont. Shelf Res.*, *63*(Mld), S26–S35, doi:10.1016/j.csr.2012.09.011.

Yablonsky, R. M., and I. Ginis (2008), Improving the Ocean Initialization of Coupled Hurricane–Ocean Models Using Feature-Based Data Assimilation, *Mon. Weather Rev.*, *136*(7), 2592–2607, doi:10.1175/2007MWR2166.1.

Zedler, S. E., T. D. Dickey, S. C. Doney, J. F. Price, X. Yu, and G. L. Mellor (2002), Analyses and simulations of the upper ocean's response to Hurricane Felix at the Bermuda Testbed Mooring site: 13–23 August 1995, *J. Geophys. Res. Ocean.*, *107*(C12), 3232, doi:10.1029/2001JC000969.

Zhang, W. G., J. L. Wilkin, J. C. Levin, and H. G. Arango (2009a), An Adjoint Sensitivity Study of Buoyancy- and Wind-Driven Circulation on the New Jersey Inner Shelf, *J. Phys. Oceanogr.*, *39*(7), 1652–1668, doi:10.1175/2009JPO4050.1.

Zhang, W. G., J. L. Wilkin, and R. J. Chant (2009b), Modeling the Pathways and Mean Dynamics of River Plume Dispersal in the New York Bight, *J. Phys. Oceanogr.*, *39*(5), 1167–1183, doi:10.1175/2008JPO4082.1.